Mehdi Kadkhodabeigi

Modeling of Tapping Processes in Submerged Arc Furnaces

Thesis for the degree of Philosophiae Doctor

Trondheim, May 2011

Norwegian University of Science and Technology
Faculty of Natural Sciences and Technology
Department of Materials Science and Engineering

NTNU – Trondheim
Norwegian University of
Science and Technology

NTNU
Norwegian University of Science and Technology

Thesis for the degree of Philosophiae Doctor

Faculty of Natural Sciences and Technology
Department of Materials Science and Engineering

ISBN 978-82-471-2841-1 (printed ver.)
ISBN 978-82-471-2843-5 (electronic ver.)
ISSN 1503-8181

Doctoral theses at NTNU, 2011:149
IMT-Report 2011:138

Printed by NTNU-trykk

Preface

This thesis is submitted in partial fulfilment of the requirements for the degree of Philosophiae Doctor at the Norwegian University of Science and Technology (NTNU). The work has mainly been carried out at the Department of Materials Science and Engineering at NTNU in the period of May 2008 to April 2011.

This work has been a part of **ProMiljø** financed by The Norwegian Ferroalloy Producers Research Association (FFF) and Norwegian Research Council. The project was a cooperation between NTNU, The Foundation of Scientific and Industrial research (SINTEF) and supporting companies within the metallurgical industries in Norway. The goal of **ProMiljø** project is to develop more efficient processes for improved internal and external environment. The project aims to achieve environmental improvements through:

- Process optimization and process control
- Control of emissions sources (gas, particles and energy)
- Reduced loss of materials and energy
- Further development of measuring equipment in collaboration with equipment suppliers to meet future environmental requirements

Comprehensive study of different processes involved in industrial production of ferroalloys, is essential in order to make further improvements. Among the different processes in a ferroalloy production plant, furnace operation is of a great importance. Tapping process is one of the main steps during furnace operation which affects the production chain environmentally, economically and through human health. The work presented in this thesis focuses on investigation of tapping processes in submerged arc furnaces (SAF's) used in ferroalloys production.

Acknowledgements

The completion of my dissertation and subsequent Ph.D. has been a long journey. It's true that "Life is what happens" when you are completing your dissertation. Life doesn't stand still, nor wait until you are finished and have time to manage it. Much has happened and changed in the time I've been involved with this project. In spite of the life's challenges and the changes in these years, working as much as possible on my dissertation has always been the number one priority. At any rate, I have finished, but not alone, and am elated. I could not have succeeded without the invaluable support of a several. Without these supporters, especially the select few I'm about to mention, I may not have gotten to where I am today, at least not sanely.

To this select group, I'd like to give a heartfelt, special thanks beginning with Professor Halvard Tveit. He was not only my supervisor during my studies at NTNU, but my mentor and friend. His patience, flexibility, genuine caring and concern, and faith in me during the dissertation process enabled me to attend to life while also earning my Ph.D. He's been motivating, encouraging, and enlightening. He has never judged nor pushed when he knew I needed to juggle priorities. We've laughed together and he's also been kind when I needed help. When others doubted, he remained a fan. When I became too serious, his humor and friendly sarcasm allowed me to laugh and lightened my perspective. He always supported me and provided insight and direction-right up to the end. For this, I cannot thank him enough. I am forever grateful. Thank You Halvard!

I'd also like to give special thanks, to Professor Stein Tore Johansen who guided me as co-supervisor in this project. His guidance, understanding, flexibility in scheduling, gentle encouragement and relaxed demeanor made for a good working relationship and the impetus for me to finish. His mentorship was paramount in providing a well rounded experience consistent my long-term career goals. He encouraged me to grow as as an instructor and an independent thinker. I am not sure many graduate students are given the opportunity to develop their own individuality and self-sufficiency by being allowed to work with such independence. For everything you've done for me, Stein Tore, I thank you.

I am very grateful to Professor Merete Tangstad as the administrator of my dissertation committee and as the leader of SiManTiAl group which I had the opportunity to be member of. Thank you Merete for being kind, encouraging and for the

many precious memories along the way.

I also would like to thank all my lovely friends in the SiManTiAl group. Their academic support, discussions, feedbacks and personal cheering are greatly appreciated. Thank you for the wonderful time we spent together.

This work has been a part of a big project called ProMiljø. I wish to acknowledge both The Norwegian Ferroalloy Producers Research Association (FFF) and Norwegian Research Council for their financial support of the project.

I would like to express my gratitude to the staff of the Department of Materials Science and Engineering and SINTEF Materials and Chemistry (Flow Technology Group). Especially Svend Grådahl for his kindly help in providing the results of previous experimental works and performing the industrial tests for the current research, Bernd Witgens for his assistance as the project leader and Helge midtdal for his help both in performing the industrial tests and fixing the problems related to using SINTEF computer cluster.

Elkem Bjølvefossen ASA, Elkem Salten AS, Elkem Thamshavn AS, Eramet Norway AS and Finnfjord AS are highly acknowledged for their extensive help and cooperation for doing the industrial tests and providing valuable data for completion of this work. Here especially Kjell Håkon Berget and Edin Henrik Myrhaug (Elkem Materials), Sven Gunnar Ramstad (Elkem Bjølvefossen), Bente Faaness (Elkem Thamshavn), Nils-Eivind Kamfjord (Elkem Salten), Henning Andersen, Benjamin Ravary and Per-Anders Eidem (Eramet Norway), Jacob Steinmo, Jill Olsen and Kjell Christian Roshol (Finnfjord) and Birger Andresen (Fesil).

Of course no acknowledgments would be complete without giving thanks to my parents. Both have instilled many admirable qualities in me and given me a good foundation with which to meet life. They've taught me about hard work and self-respect, about persistence and about how to be independent. My mother, especially, is a symbol of devotion, politeness, strength and character. Both have always expressed how proud they are of me and how much they love me. I am proud of them too and love them very much. I am grateful for them both and for what they have done for me.

Trondheim, May 2011

Mehdi Kadkhodabeigi

Contents

List of Figures

List of Tables

List of Symbols

u, v ..... Fluid velocity $[m/s]$
ρ ..... Fluid density $[kg/m^3]$
p ..... Pressure $[Pa]$
g ..... Gravity acceleration $[m/s^2]$
μ ..... Fluid viscosity $[kg/m.s]$
μ_t ..... Turbulent viscosity $[kg/m.s]$
ε ..... Porosity of packed bed
β ..... Thermal coefficient of volumetric expansion $[1/K]$
F ..... External force $[N/m^3]$
k_{eff} ..... Effective thermal conductivity of fluid $[W/m.K]$
c_p ..... Specific heat of fluid $[J/kg.K]$
C_μ ..... Turbulence model constant
d_p ..... Particle size $[m]$
k ..... Turbulence kinetic energy $[m^2/s^2]$
ϵ ..... Turbulent dissipation rate $[m^2/s^3]$
I ..... Unit tensor
T ..... Temperature$[K]$
E ..... Energy
α ..... Permeability of packed bed
C_2 ..... Inertial resistance
Y_i ..... Mass fraction of species i
$D_{i,m}$ ..... Diffusion coefficient for species i
Sc_i ..... Schmidt number
D_t ..... Turbulent diffusivity
σ_s ..... Stefan - Boltzmann constant
H_m ..... Metal height $[m]$
H_s ..... Slag height $[m]$
D_v ..... Valve diameter $[m]$
τ ..... Stress tensor

h_j ..... Species enthalpy
C_d ..... Discharge coefficient
σ_k ..... Turbulent prandtl number for k
σ_ω ..... Turbulent prandtl number for ω
q_r ..... Radiative heat flux $[W/m^2]$
R_i ..... Production rate of species i by chemical reaction
κ ..... Phase index

Chapter 1

Introduction

GLOBAL production of ferrosilicon and ferromanganese and other types of ferroalloys has been increasing in the recent years in parallel to the increased production of steel. The demand for silicon in the global market has also increased due to its wide range of applications from alloying element in aluminum industry to the photovoltaic solar cells and medical purposes. Silicon and most of the ferroalloys are commercially produced in Submerged Arc Furnaces**(SAF's)** through carbothermic reduction of the ores. The reactions involved in the carbothermic reduction of the ores are highly endothermic and hence the production process is very energy intensive. Moreover the production process creates huge amount of gas and solid pollution which should be controlled and reduced somehow in order to improve the environmental standards.

Reducing the energy consumption and environmental pollutants as well as improving the working conditions are important goals in ferroalloys industry. Stable Submerged Arc Furnaces operation is required in order to reach these goals. There are different issues which affect the stability of the furnace operation. Among different industrial processes involved in the production of silicon and ferroalloys, tapping process plays an important role regarding the stability of furnace operation. Tapping is simply bringing the molten products of the smelting process from the furnace hearth into the ladle for casting or other post taphole operations. If tapping due to any reason fails the furnace operation must be stopped or to be continued at reduced load to complete the tapping before the process can proceed. Therefore good and secure drainage of the molten products from the furnace is essential in order to have optimum production yield and a safe operation. Accumulation of the produced melt in the furnace over time will disturb the smelting process and hence

causes decreased yield.

During furnace tapping a very high temperature flow of the melts has to be controlled. It makes considerable challenges including the safety of operation and environmental issues. Presence of the fumes released from the melt flow and from the ladle together with process gases which sometimes blow out of the furnace taphole, cause the tapping area to be recognized as one of the most important sources of internal pollution in the plants. Capturing of the tapping fumes therefore is a challenging issue in the silicon and ferroalloys industries. The combination of hot metal flow and gases blowing out of the taphole also creates a potentially hazardous working condition in the tapping area.

Tapping process is directly influenced by in-furnace governing conditions and furnace operation. How the mentioned issues can affect tapping in the submerged arc furnaces, has not been examined well. In the case of the conditions inside the furnace, the problem is that accessing to the hearth of an operating furnace in order to obtain information is very limited and in many cases it is impossible. In fact pyrometallurgical operations, such as those occurring in bath type smelting or reduction furnaces, seldom lend themselves to accurate characterization, unlike processes occurring at lower temperatures and less aggressive chemical conditions. Measurements of temperature, liquid level, pressure and flow rates, which often are trivial at lower temperatures are either not possible or can simply not be determined at higher temperatures.

The mentioned limitations in doing wide range of experimental works in one hand and the need for having a better understanding of the process on the other hand imply that development of conceptual models of the furnaces based on the fundamental principals is significantly important. Submerged arc furnaces are basically very complex systems for being accurately studied and modeled. This is mainly due to high temperature nature of the smelting process which includes chemical reactions, phase changes, gas and liquid flows and energy conversion inside the furnace. However fundamental modeling approaches in addition to acceptable accuracy for understanding purposes, provide insight into the real processes. Therefore in the present research the modeling approach is employed in order to investigate the tapping process and its related issues in the submerged arc furnaces used in silicon, ferrosilicon and ferromanganese production.

1.1 Research motivation

Since tapping process is an important step in the production chain of ferroalloys and there are many industrial challenges regarding to it, therefore an in-depth investigation of the process and its affecting phenomena seems to be necessary. The research was started aiming to increase the understanding of the effect of conditions inside the furnace on the tapping process in submerged arc furnaces. A better understanding of the governing conditions on the tapping then could help the industry to improve their productivity through having a more stable furnace operation. Since tapping process influences the environmental and safety issues in the plants, this study could also be useful in making a more environmental friendly and safer operation as well. Investigation of the tapping in different type of submerged arc furnaces has not been reported before, therefore it could also provide a reference to be used in designing new methods of tapping and/or future studies.

This research is a part of a bigger project called **ProMiljø** which focuses mainly on the energy and environmental issues in the ferroalloys industry. **ProMiljø** project is financially supported by The Norwegian Ferroalloy Producers Research Association (**FFF**). Since this project is supported by Norwegian ferroalloys producers, very good cooperation between industry and research institutes in doing industrial tests and having scientific discussions does exist. This cooperation helps a research project in many ways such as getting familiar with real industrial challenges, using the industrial experiences in the modeling procedure, doing industrial measurements in order to find enough inputs for the model and also validation of the research results through industrial tests.

1.2 Research focus area

In this research the main focus is on the tapping related issues in the submerged arc furnaces. The effect of in-furnace conditions and operational decisions on the tapping parameters is extensively investigated. The processes under investigation are divided into two main categories. The slag-free smelting processes like silicon and ferrosilicon production and the smelting processes including slag as a separate phase in the system, such as ferromanganese production. Operating conditions inside the furnace are different, depending on the type of production. Depending on the properties of the systems under study, the applied modeling approaches are different. Environmental aspects of tapping process in the silicon and ferrosilicon furnaces through designing a new hood system for capturing the tapping off-gases

is also addressed.

Transport phenomena such as flow of gas and liquid through solid particle beds and chemical reactions are typical phenomena taking place inside a SAF. CFD is a powerful modeling technique for these kind of problems. The models developed in this research have the following features:

- The models have been built based on a robust theoretical basis using Computational Fluid Dynamics (CFD) techniques
- In-furnace conditions have been defined based on the best of knowledge available about the furnace inside
- The results of industrial measurements and observations have been used either as the model's inputs or the validation tool in the modeling procedure

1.3 Thesis outline

The reminder of the thesis is divided into four parts as follows:

Part I starts with a short description of silicon, ferrosilicon and ferromanganese production process in the submerged arc furnaces. Furnace structure, different phenomena and chemical reactions occurring in the furnace are briefly reviewed. Formation of different zones in the furnace charge materials and physical properties of each zone is explained. Significant gas pressure in the furnace crater zone as a unique feature of the silicon and ferrosilicon furnaces is discussed. In addition the method used for industrial measurements of the furnace crater pressure and the obtained results are presented. This part is then followed by describing the tapping process in the silicon and ferrosilicon furnaces, importance of the tapping in the production chain, introducing the main affecting issues on the tapping and explaining how these issues influence the tapping parameters. One industrial challenge during tapping of silicon and ferrosilicon furnaces known as taphole gassing phenomenon is addressed. The taphole gassing phenomenon, the root reasons of occurring and different aspects, specially environmental aspect, of the phenomenon are described.

Part II starts with explaining the Computational Fluid Dynamics (CFD) modeling technique and some of its reported applications in studying the submerged arc furnaces and similar systems. The main steps in developing a multiphase model for an industrial size submerged arc furnace including making the furnace geometry, defining different zones in the furnace, recognizing the governing equations on the system, choosing the right boundary conditions and using the proper solver for the

developed set of equations, are described. Using the model results such as the gas and liquid flow patterns in different zones of the furnace and tapping flow rates in explaining how different issues affect the tapping parameters and which issues are of most importance, are extensively discussed. This part continues with describing the industrial measurements of the furnace tapping rates, equipments used in the tests and the obtained results for both silicon and ferrosilicon furnaces. It is then followed by comparing the results of model and the results obtained from the industrial tests in order to validate the developed model. Finally some industrial applications of the described model are presented.

Part III begins with explaining a new hood design for capturing the taphole off-gasses as well as the fumes coming out of the ladle. Development of a CFD model for the taphole gassing phenomenon in order to study the effectiveness of the designed hood in capturing the off-gases (feasibility study before constructing the hood in the industrial scale) will be presented. Finally the results of the model, successful industrial tests of the new hood system and remaining challenges before it can be widely installed in the industrial plants, are discussed.

Part IV describes the stratified tapping of slag and metal from submerged arc furnaces used in ferromanganese production. The furnace structure by focusing mainly on the furnace hearth where the metal and coke bed do exist, is explained. Models developed for tapping process in the similar systems like blast furnaces are briefly reviewed. This part continues with describing the procedure of developing a CFD model for the tapping process in a ferromanganese furnace. The model results including the slag and metal flows in the furnace hearth during tapping, melt flow rates coming out of the taphole and heat distribution in the melts as well as furnace refractory and furnace walls are presented. Finally comparison between the model results and industrial measurements in order to show the validity of the model is represented.

1.4 Publications

1. Kadkhodabeigi, M., Tveit, H., Johansen, S. T. CFD Modeling of Tapping Process in Ferromanganese Furnaces, *eighth International Conference on CFD in Oil & Gas, Metallurgical and Process Industries*, 21-23 June 2011, Trondheim, Norway.

2. Kadkhodabeigi, M., Tveit, H., Johansen, S. T. Modeling the Tapping Process in Submerged Arc Furnaces Used in High Silicon Alloys Production, *ISIJ*

International, Volume 51, Number 2 / 2011, pp. 193-202.

3. Kadkhodabeigi, M., Tveit, H., Johansen, S. T. CFD Modeling of the Effect of Furnace Crater Pressure on the Melt and Gas Flows in the Submerged Arc Furnaces Used for Silicon Production, *Journal of Progress in Computational Fluid Dynamics*, Volume 10, Number 5-6 / 2010, pp. 374-383.

4. Kadkhodabeigi, M., Tveit, H., Berget, K. H. Silicon Process-New Hood Design for Tapping Gas Collection, *INFACON XII, Sustainable Future*, ISBN: 978-952-92-7340-9, Vol. 1, pp. 109-119.

5. Kadkhodabeigi, M., Tveit, H., Johansen, S. T. Modeling the Tapping of Silicon Melt from the Submerged Arc Furnaces, *Seventh International Conference on CFD in the Minerals and Process Industries*, 9-11 December 2009, Melbourne, Australia.

Chapter 2

Submerged Arc Furnaces Used in Ferroalloys Production

2.1 Silicon and ferrosilicon production

SILICON (Si) is a light chemical element with metallic and non-metallic characteristics. In nature, silicon combines with oxygen and other elements to form silicates. Silicon in the form of silicates constitutes more than 25% of the Earths crust. Silica is a silicate consisting entirely of silicon and oxygen. Silica as quartz is used to produce silicon ferroalloys, mostly FeSi 55 and FeSi 75, and silicon metal (Schei et al. [1998]).

”Global silicon and ferrosilicon Market to Reach 4.6 Million Tons by 2015. Worldwide demand for silicon and ferrosilicon slumped in 2008 and 2009, as a result of global economic crisis. However, the market is expected to bounce back to normalcy due to revival of the demand for silicon and ferrosilicon, which was observed during the end of 2009. Historical factors such as regular semiconductor cycle length of 5-6 quarters, along with the timing of governmental fiscal and economic policy, are evincing revival of the market. Growing demand for core silicon from leading electronic markets are growing despite the downturn, are likely to aid in the survival of core silicon manufacturers. Growing demand for polysilicon from key PV markets is most likely to decrease the pressure on the silicon prices in the near future. Metallurgy constitutes the largest end-use segment for Silicon. Consumption of silicon by the end-use is projected to reach 532.9 thousand tons by 2012. Chemicals represent the other major end-use segment. However, photovoltaic represents the fastest growing end-use segment of silicon. Ferrous Foundry

represents the largest consumer of ferrosilicon. Steel Industry represents the other principal consumer of ferrosilicon. Growth in the silicon and ferrosilicon will be in line with long-term trends in the end-use industries. Currently, auto makers face a tough environment from more stringent environmental standards. Consequently, several new trends and innovations are emerging in the form of lighter, more fuel-efficient automobiles, cost-effective fuel cells, and hybrid electric vehicles. Another key trend is in the changing material mix of the automobile industry with a growing application of lightweight, high-performance aluminum in production. This trend bodes well for aluminum and has direct and positive implications for the ferroalloy industry, particularly for silicon metal as an alloying material" (GIA2010).

2.2 Process description

Silicon and ferrosilicon are industrially produced as the result of carbothermic reduction of raw materials in submerged arc furnaces. The raw materials introduced into the furnace are composed of mineral ores and carbon containing materials such as coke, coal, charcoal and wood chips which act as reductant in the process. Electrical energy supplies the necessary energy for the endothermic reactions. The ores used in the charge depending on the production type are quartz in silicon production and a mixture of quartz and iron ore in ferrosilicon production. The raw materials, according to the specification of final product, are subsequently weighed, mixed and moved to the furnace bins and finally added to the furnace top through several charging tubes. Silicon and ferrosilicon plants in principle contain several furnaces. The raw materials are heated in the furnace by large amount of electric energy and molten product is produced. Depending on the furnace size the energy consumption and production rates are different.

Smelting process in the submerged arc furnaces is highly energy intensive and hence a large portion of the total production costs is related to the energy consumption. According to Schei et al. [1998], about 32% of the energy consumed in the process remains as chemical energy in the product. Some of the remaining 68% is captured by the water cooling system of the furnace, but the largest fraction of the energy is in the SiO and CO off-gas escaping over the furnace top. Energy recovery in the silicon and ferrosilicon producing furnaces has been an important issue. There are different industrial challenges related to design and operation of energy recovery systems for submerged arc furnaces. However in some of the modern plants there is energy recovery system which utilizes the heat in the off gas in order to produce electric energy in steam turbines or to produce warm water or steam for

other applications. The energy which can be recovered from the off gas is about one third of the energy content of the waste gas. A large portion of the dust released from the furnace top is silica fume ”microsilica”. Proper filtration of the off gas results in producing large amounts of microsilica which has its own market. The molten product is tapped from the furnace at scheduled time intervals and it is further processed by casting, crushing and screening or granulating to meet customer's specifications (Schei et al. [1998]). Schematic of the silicon production process has been shown in Figure 2.1.

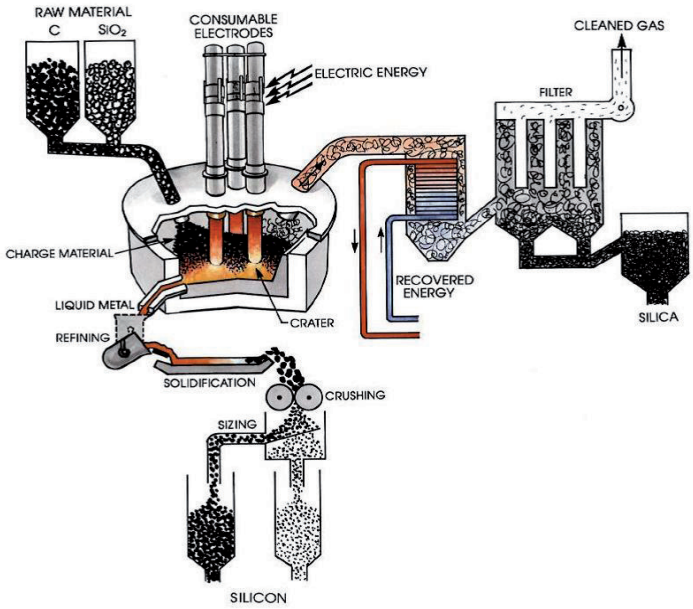

Figure 2.1: A schematic of the silicon production process (Schei et al. [1998]).

2.3 Furnace structure

Submerged arc furnaces are the hearts of ferroalloys production plants. Furnaces are like the cylindrical vessels and the furnace casing is made of sheet steel, the lower part lined with hard and strongly calcined carbon blocks which are suitable for high temperature working conditions and the upper part is lined with firebrick. The furnace shell and lining are designed in a way to ensure a long operation life. The

furnace contains three electrodes which are symmetrically situated at the corners of a regular triangle and they are submerged into the charge materials. Conversion of the electrical energy into heat in the bulk of the charge materials results in carbothermic reduction of the ore. As the smelting process proceeds the molten ferrosilicon together with process gases mainly composed of SiO and CO are produced. The off-gas flows towards the charge materials and it is released from the furnace top. The furnace off-gas burns as it comes into contact with the air flow on the furnace top. In order to have control on the combustion and collection of the furnace off-gas, today modern submerged arc furnaces are mainly semi-closed. Since stoking of the raw materials should be done through the charge surface during the smelting process, on the furnace top there are special gates which are closed most of the time and they are opened for stoking operation. A schematic cross section of a silicon/ferrosilicon furnace is shown in Figure 2.2.

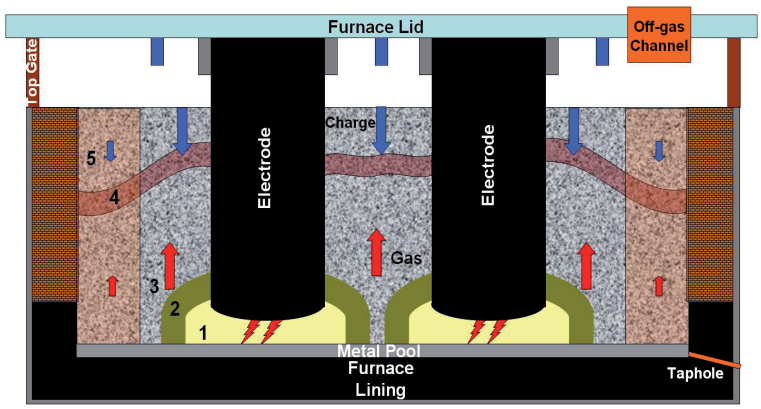

Figure 2.2: A cut through, graphical depiction of the submerged arc furnace used in high silicon alloys production. Different zones have been formed in the charge such as crater zone (1), crater wall (2), softening and melting zone (3), crust formation zone (4) and stagnant charge zone (5).

Conversion of electric energy into heat creates enough potential for the chemical reactions to happen. A large portion of the electric energy is converted to heat in the regions close to electrode tips through electric arcs. Therefore the temperature in the zones close to electrode tips is very high comparing to the other zones in the furnace. These zones marked with number 1 in Figure 2.2 are known as furnace crater.

The furnace electric power supply for silicon furnace typically lies between 10

and 40*MW* and relates to the physical dimensions of a furnace. The height of a furnace is in the range 2.2 - 3.5*m*, the internal diameter at the top is 5 - 12*m*, and the internal diameter at the bottom is 5-9*m*. According to Schei et al. [1998], a typical medium-sized silicon furnace would be 20*MW* with a pot diameter of 7*m*, a pot depth of 2.7*m*, electrode diameter of 1.25*m*, and a distance between the electrode centers of 2.6*m*.

2.4 Chemical reactions occurring inside the furnace charge

Carbothermic reduction of the ores as the result of different chemical reactions leads to production of metal in the submerged arc furnaces. The general chemical reactions happening in a silicon producing furnace are as follows (Schei et al. [1998]):

$$SiO_2(s,l) + 2C(s) = Si(l) + 2CO(g), \Delta H = 870.241kJ/mol \tag{2.1}$$

$$SiO_2(s,l) + C(s) = SiO(g) + CO(g), \Delta H = 792.510kJ/mol \tag{2.2}$$

In the case of ferrosilicon, reduction of the iron ore as it is presented in the following reaction should be considered as well.

$$Fe_2O_3(s,l) + 3C(s) = 2Fe(l) + 3CO(g), \Delta H = 455.002kJ/mol \tag{2.3}$$

The above mentioned chemical reactions are composed of different other reactions which happen in the charge. Endothermic nature of the main reactions shows that the heat distribution in the charge material plays an important role in determining the rate of reaction in different zones in the furnace. The results of different researches prove that the common chemical reactions in both silicon and ferrosilicon production occur in specific zones. Inside the furnace is generally divided into two parts known as inner (zones 1, 2, 3 and lower part of zone 5) and outer (zone 4 and upper part of zone 5) parts. In the inner part of the furnace the main chemical reactions are (Schei et al. [1998]):

$$SiO_2(s,l) + Si(l) = 2SiO(g), \Delta H = 605.441kJ/mol \tag{2.4}$$

$$SiO(g) + SiC(s) = 2Si(l) + CO(g), \Delta H = 166.714kJ/mol \tag{2.5}$$

$$2SiO_2(s,l) + SiC(s) = 3SiO(g) + CO(g), \Delta H = 1377.597kJ/mol \tag{2.6}$$

Solid carbon has a very high melting point and it is only in solid phase while attending in reactions with liquid and gas phases available in the furnace. Quartz in

the other hand has a lower melting point and its softening begins in the middle part of zone 3 in the Figure 2.2 and the melting starts near the boundaries of zones 2 and 3 in the same figure. The silica melt then flows towards the furnace crater and causes reaction 2.4 to happen. Reaction 2.4 is the main SiO forming reaction in the system and needs high amount of energy to proceed. This reaction happens in the very high temperature zone of the furnace just under the electrode tips which is marked as zone 1 in Figure 2.2. Reaction 2.5 is the most important metal forming reaction in the furnace. This reaction also needs high amount of energy together with an environment with high partial pressure of SiO gas to occur. Zone 2 in Figure 2.2 is the most probable zone where this reaction happens.

The process gases produced in the furnace inner zone contain SiO and CO gas flows towards the furnace top through charge materials. In ferrosilicon production CO gas attends in a set of reduction reactions for iron ore. This reaction happens in the upper part of charge known as the furnace outer zone. One of the most important reactions in the outer zone is the formation SiC as an intermediate product of the process based on reaction 2.7 (Schei et al. [1998]):

$$SiO(g) + 2C(s) = SiC(s) + CO(g), \Delta H = -77.592kJ/mol \tag{2.7}$$

This reaction which mostly occurs in zone 3 shown in Figure 2.2, plays an important role in recovery of silicon in the furnace and hence results in higher production yield. Since the proper flow of reactive gas in the bed of solid particles is very important in determining the rate of gas-solid reactions, physicochemical properties of carbonaceous materials used in the charge such as particle size and reactivity are very important.

Condensation of SiO gas in zone 4 shown in Figure 2.2, is another phenomenon which happens in the upper part of the furnace charge. The reaction happens when the charge temperature is less than the condensation temperature. Condensation based on reaction 2.8 causes reduced escape of SiO gas from the furnace and hence increased silicon recovery in the furnace.

$$2SiO(g) = Si(l) + SiO_2(s, l), \Delta H = -306.92kJ/mol \tag{2.8}$$

The product of reaction 2.8 is found in relatively thick layer of a brown substance in the upper part of the charge (Schei et al. [1998]).

2.5 Formation of different zones in the furnace

During the smelting process, submerged arc furnaces are periodically fed by mixture of charge materials. Quartz particles are mostly lumpy while a there is a limitation on size of iron ore and carbon containing particles in the charge mixture. However the furnace is always filled with the bulk of charge particles. Since the particles are not so compact and the void fraction between them is filled with process gases, the furnace charge behaves as a porous environment. Excavations of the submerged arc furnaces show that several zones with different physical properties are formed in the charge materials (Zherdev et al. [1960]), (Otani et al. [1968]), (Schei [1967]), (Myrhaug [2003]) and (Tranell et al. [2010]). Figure 2.3 represents the results found from excavation of an industrial ferrosilicon furnace.

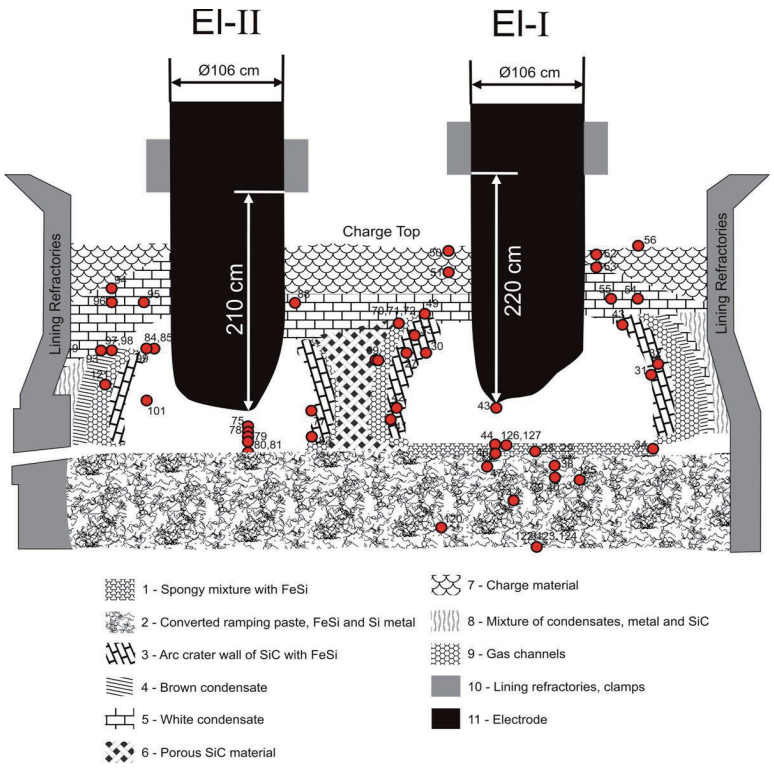

Figure 2.3: Formation of different zones in the charge materials of a ferrosilicon producing furnace, the result is from excavation of an industrial furnace (Tranell et al. [2010]).

This figure clearly shows that the furnace charge is divided into different regions and each zone has a specific materials and hence physical property. In fact formation of different zones in the charge is due to different phenomena and chemical reactions happening inside the furnace. Different regions formed in the silicon and ferrosilicon furnaces and the most probable reason of their formation are discussed here.

2.5.1 Active and inactive charge

Melting of charge particles and chemical reactions between different phases in the charge materials are the parameters which influence formation of different zones in the furnace. In this perspective the heat distribution in the charge plays the most important role. During furnace operation the consumption of charge materials in a column which surrounds the electrodes is higher comparing to the part of charge which is close to the furnace sidewall. Part of the charge which is closer to the furnace wall, shown with light brown color in Figure 2.2, is quite stagnant during furnace operation. The charge material in this zone is called inactive charge since it remains mostly unreacted inside the furnace. The main reason is that the chemical reactions rate and hence the raw materials consumption in the active zone is higher because of higher temperatures in this zone. Active and inactive part of the furnace charge are schematically shown in Figure 2.4.

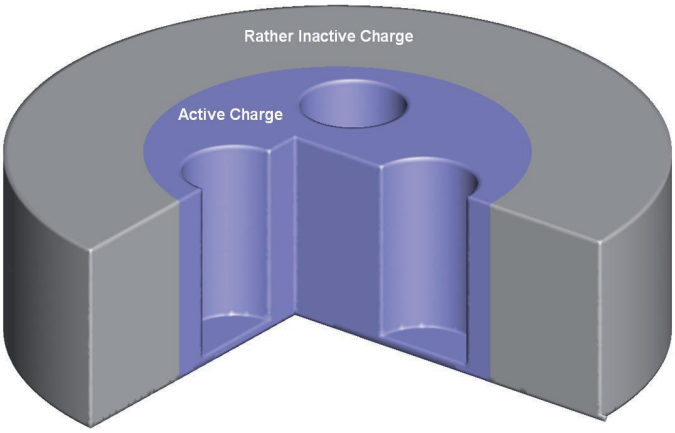

Figure 2.4: A schematic view of active and inactive part of charge materials inside a submerged arc furnace used in high silicon alloys production.

Since the inactive part of the charge has lower temperature comparing to the active charge and also the charge particles in this zone can barely move, there is a high potential for condensation of process gases in this zone.

2.5.2 Crust formation in the charge

In the zones where the condensation of SiO gas takes place, the charge particles are mostly glued together. As the result of this phenomenon, permeability of the charge decreases and the pressure of process gases in the furnace increases. This phenomenon is known as crust formation in the furnace charge and it mainly happens through making a brownish layer of particles in the upper part of the charge (zone 4 in Figure 2.2). If the thickness of the glued charge increases the process gases will mostly escape from the furnace through the gas channels formed around the electrodes. Therefore the flow of gas among the charge particles does not effectively happen and hence the rate of vital gas-solid reactions in the charge as well as SiO recovery decreases.

Crust formation in silicon and ferrosilicon furnaces is very common and one main reason of the stoking process is in fact breaking the crusts formed in the charge. The crust in the inactive part of the charge can be very thick, hardly broken and impermeable. Therefore it is known as an industrial challenge during furnace operation.

2.5.3 Formation of cavities

Formation of cavities around the electrode tips in silicon and ferrosilicon furnaces has been seen frequently in the furnace excavations. The presence of such cavities in the furnace charge was established by Zherdev et al. [1968] using probes inserted into the charge. Otani et al. [1968] used visual peep pipes which were inserted towards the cavities in the charge of laboratory furnaces and small industrial furnaces. They established the occurrence of cavity around the electrode tip by observation and film recordings and saw electric arcs burning between the electrode tip and metal pool under the cavity. At the metal bath surface lumped materials were floated which continuously appeared in spite of rapid consumption due to the arc heating. The cavities have the following typical features (Valderhaug [1992]):

1. The arcs burn between the electrode and the liquid metal bath.
2. After tapping of the furnace the cavity bottom consisting of solid materials, is observed, which disappears as the liquid metal is produced.

3. Just after stoking and charging of raw materials, tough materials, probably silica, sag down from the cavity roof and partly cover the liquid metal bath. This sagging soon decreases.

4. Next, a somewhat different sagging of tough materials with solid particles, occurs. These materials float at the liquid metal surface and are consumed continuously by the reactions.

5. As time goes by, the cavity size increases, mainly upwards, provided the furnace is operated at a correct stoichiometric balance. This is due to the continuous sagging of materials from the cavity roof.

Quartz lumps start melting in the regions above the crater zone based on the temperature distribution in the furnace. Liquid silica has very high viscosity especially when its temperature is close to the melting point. As the melt flows in the charge bed, it acts like a glue for the solid particles involved in the melt. Based on the temperature distribution in the charge, considering the arc region as the zone with highest temperature, a dome shape layer composed of silica melt and the captured particles by the melt is formed around the electrode tips (zone 2 in Figure 2.2). This zone is called crater wall because it surrounds the crater zone like a wall. As smelting process proceeds silica melt and solid particles in the crater wall are consumed by chemical reactions which occur. Therefore a large amount of process gases are produced and because of low permeability of the crater wall the gas pressure in the crater zone increases. Increasing the gas pressure which pushes the crater walls in one hand and decreasing the crater wall thickness through consumption by the reactions, lead to increased cavity size. Process gases will however pass through the crater wall when the gas pressure increases up to a limit. Therefore increase in the cavity size stops in some level. Moreover stoking process mostly causes collapsing the crater wall into the crater zone and hence changes the cavity size.

2.5.4 Formation of porous bottom bed

The results of furnace excavation show that over the furnace bottom there is a layer of solid SiC particles. This layer is porous which means the void fraction between the particles during the furnace operation is filled with liquid silicon or ferrosilicon. The thickness and other physical properties of this porous layer depend on its position in the furnace.

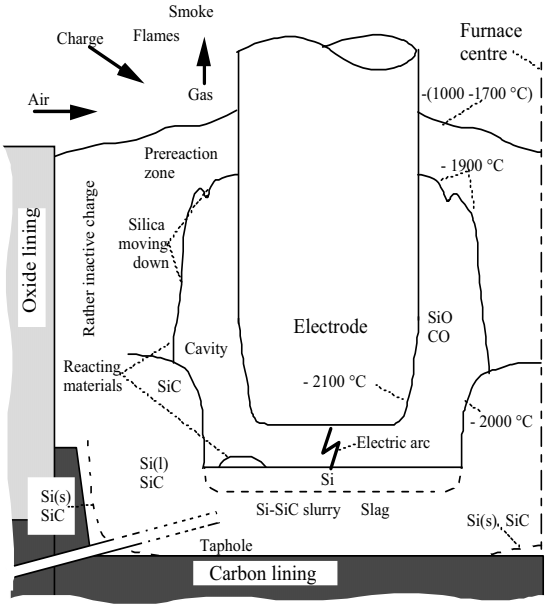

Figure 2.5: The inner structure of a submerged arc furnace used in silicon or ferrosilicon production (Westly [1979]). Formation of cavity and porous bed of SiC particles on the furnace bottom are graphically shown.

Accumulation of SiC in the furnace can happen if the balance in the reactions or in the charge is not fulfilled. In fact in operation with excess C in the charge the surplus will be deposited as SiC at the bottom. When the charge is corrected, the SiC can be consumed close to the electrode. But a distance away from the electrode the SiC will be left as a wall and leave a depression around the electrode. If the furnace is rotated, the depression of the three electrodes will go together and give a circular trench with walls of SiC (Schei et al. [1998]). Formation of cavity and porous bottom bed on the furnace bottom are graphically shown in Figure 2.5.

2.6 Furnace crater pressure

Quartz and the carbonaceous materials are added into the furnace in solid state, and the products in addition to silicon/ferrosilicon melts and some slag are mainly in a gaseous phase as CO and SiO. Also according to the gas law, the high temperature in

the reaction zone will increase the volume of the gas. In a silicon furnace of 24 MW for example, the amount of added solid material is on average in the order of 0.001 m^3/s . The volume of the CO gas and the SiO gas produced in the crater, due to the high temperature, will be in the order of 10 m^3/s (Tveit et al. [2002]). The cavities formed in the the furnace charge are filled with a mixture of CO and SiO gases during furnace operation. If the rate of production and removal of process gases in the cavities is equal then the gas pressure in the crater zone remains constant but accumulation of the gas in these zones due to any reason leads to increased furnace crater pressure. Process gases in the crater zone have high temperature and reactive nature and because the crater pressure could influence fluid flows in different zones of the furnace, investigation of furnace crater pressure and the affecting parameters in details was necessary.

2.6.1 Industrial measurements of furnace crater pressure

Measuring the crater pressure in an industrial furnace was done through inserting a steel pipe with internal diameter of 12*mm* into the electrode paste along the electrode axis down to the crater zone. The pipe inlet is then in the crater zone and the pipe outlet is connected to a differential pressure cell (Johansen et al. [1998]). Figure 2.6 shows how the experimental set up looks like.

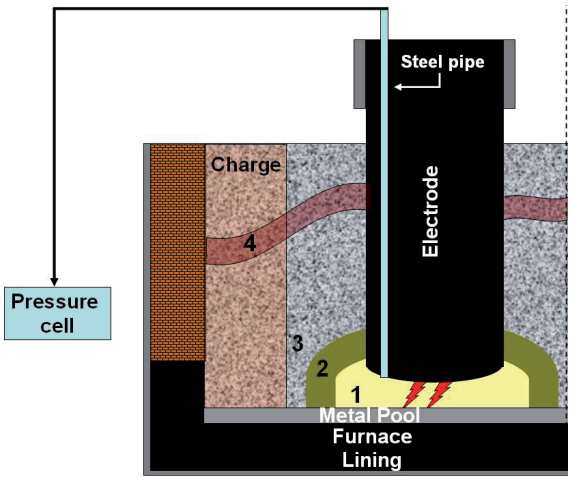

Figure 2.6: Experimental set up for measuring the crater pressure in an industrial furnace.

Industrial tests are done using separate steel pipes, pressure cells and concocting

tubes for each three electrodes. Therefore it is possible to get information from the cavities formed under each electrode in the furnace.

In order to clean the steel pipe before starting the pressure measurements the nitrogen gas is blown into the pipe. The differential pressure cells used in the experiments were from Fuji Electric Co. Ltd type FHCW34V2-AKCYY-AE with a pressure range of 0-200 *mbar*. Differential pressure cells installed on an industrial ferrosilicon furnace are presented in Figure 2.7.

Figure 2.7: Installed differential pressure cells for measuring the furnace crater pressure in a ferrosilicon furnace and the operators while setting up the connections.

Results on industrial measurements show that the furnace crater pressure has a dynamic behavior (Ingason [1994] and Johansen et al. [1998]). The pressure under different electrodes in a furnace also can be to some extent different (Johansen et al. [1998]). An example of measured crater pressure under two electrodes of a silicon producing furnace is shown in Figure 2.8. The dynamic behavior of the furnace crater pressure is clearly seen in this figure. The results of measurements show that

there are three main parameters which affect the furnace crater pressure. These parameters are furnace electric load, charge permeability and stoking process.

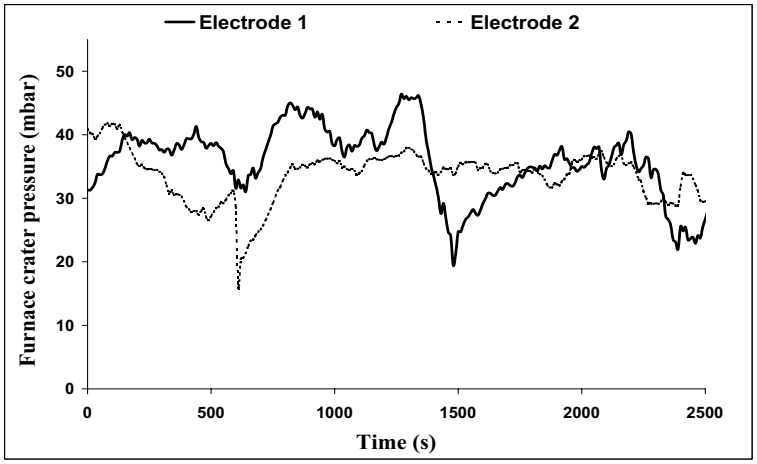

Figure 2.8: Industrial measurement of crater pressure under different electrodes in a submerged arc furnace used in silicon production (Johansen et al. [1998]).

2.6.2 The effect of charge permeability on the crater pressure

Easier penetration of the process gases through the crater wall leads to better gas distribution in the charge and lower crater pressure. Lower gas pressure in the upper part of the charge means higher pressure difference between the crater zone and the furnace outer zone. Higher pressure difference between these zones acts as a driving force for the gas flows through charge particles and towards the furnace top. Pressure build-up in the furnace crater zone can be caused because of reduced permeability of the charge materials in the furnace outer zone. It can happen because of the type of carbonaceous materials used in the charge mixture. For example using more wood chips than coke in the charge mixture increases the charge permeability. Reduced charge permeability can also happen due to condensation of SiO gas in the upper part of charge. Reduced permeability of the charge due to any of the mentioned reasons causes higher gas pressure in the charge and hence lower driving force for the gas flow from the crater zone. This phenomenon finally leads to formation of a high pressure crater zone in the furnace.

2.6.3 The effect of furnace electric load on the crater pressure

Industrial measurements of the furnace crater pressure show that there is a direct relation between the pressure in the crater zone and the furnace electric load (Tveit et al. [2002]). It is mainly due to the fact that the rate of chemical reactions happening in the crater zone is proportional to the heat generated in this zone and the furnace electric power is the main source of heat generation in the furnace. The relation between the furnace crater pressure and the furnace electric load for different furnaces are presented in Figure 2.9.

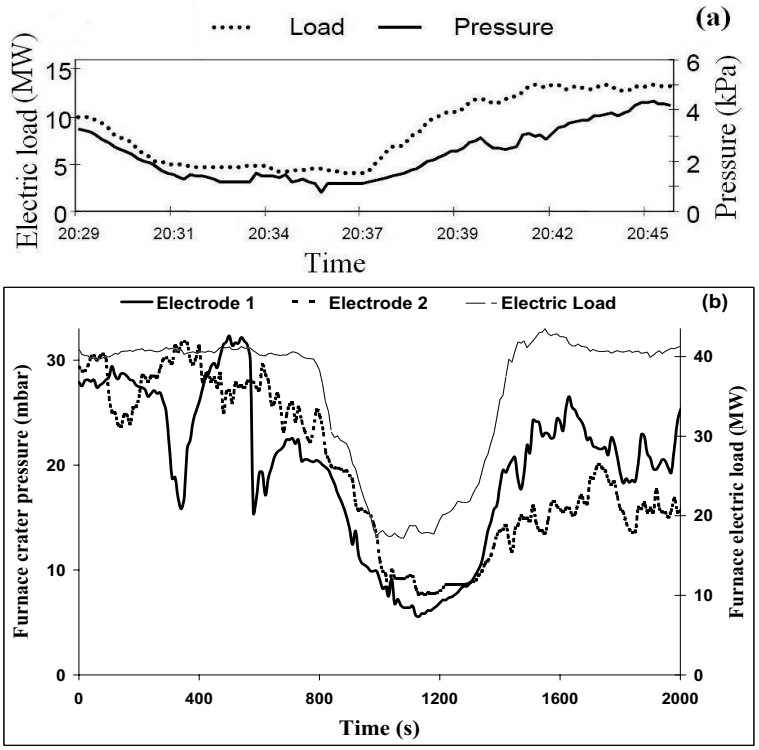

Figure 2.9: Direct relation between crater pressure and furnace electric load as the result of industrial measurements in different submerged arc furnaces used in silicon production (Tveit et al. [2002] (a) and Johansen et al. [1998]) (b).

2.6.4 The effect of stoking process on the crater pressure

The charge mixture is periodically introduced to a furnace top. Since the consumption of the charge materials in the regions close to the electrodes is higher than the other zones, stoking of the charge into these zones is necessary in order to have a productive operation. During the stoking process the charge materials from the charge surface are pushed towards the electrode surroundings using the stoking car. Falling and avalanche of charge particles on top of the crater zone causes collapse of crater wall and therefore a lot of charge falls into the furnace crater zone which is filled by process gases. This phenomenon then leads to release of process gases from crater zone. Therefore crater pressure decreases and the amount of SiO gas escaping from the furnace top as dust increases. Figure 2.10 shows this effect while doing experimental tests in an industrial ferrosilicon furnace (Johansen et al. [1998]).

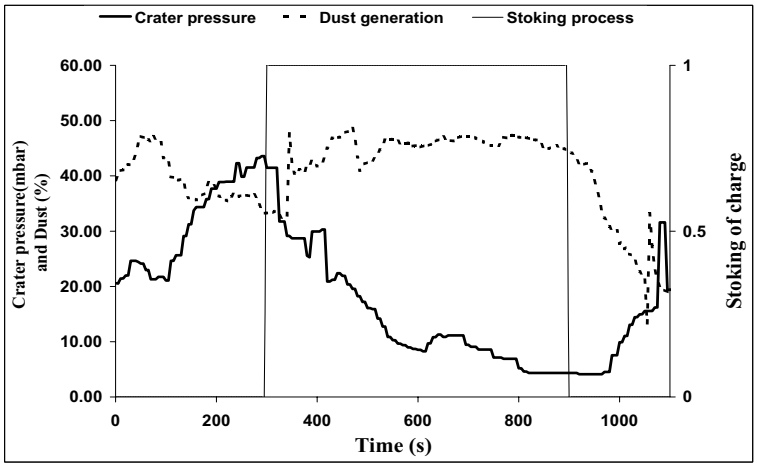

Figure 2.10: The effect of stoking process on the crater pressure and dust generation in an industrial submerged arc furnace used in ferrosilicon production (Johansen et al. [1998]).

As it can be seen from Figure 2.10 stoking of charge materials causes rapid and temporary variation in the crater pressure and the amount of dust entering into the off-gas system.

2.7 Ferromanganese Production Process

Manganese is little known to the public but very important to the modern society. Manganese is the fourth most used metal in terms of tonnage, being ranked behind iron, aluminum and copper, with in the order of 34 million tons of ore being mined annually (2006). Manganese has numerous applications which impact on our daily lives as consumers, whether it is of objects made of steel, of portable batteries, or of aluminum beverage cans. Manganese has played a key role in the development of various steelmaking processes and its continuing importance is indicated by the fact that about 90% of all manganese consumed annually goes into steel to neutralize the harmful effect of sulphur and as an alloying element. No satisfactory substitute for manganese in steel has been identified which combines its relatively low price with outstanding technical benefits (Olsen et al. [2007]). Manganese is mainly added to the liquid steel in the form of manganese alloys which are described below.

High carbon ferromanganese is commercially produced by carbothermic reduction of manganese ores, primarily in electric submerged arc furnaces. Recently built furnaces for the production of ferromanganese have capacities of 75-90 MVA. The produced metal typically contains around 78% Mn and 7% C, and the slag around 40% MnO (high-MnO slag practice). An increasing part of the metal is refined to medium or low carbon ferromanganese (Olsen et al. [2007]).

Electric furnaces used in the production of manganese alloys are generally circular and have three electrodes, each connected to a separate electrical phase. The electrodes are submerged in the burden and the electric current run through the area bellow the electrode tips where electrical energy is converted to heat. Produced slag and metal may be tapped simultaneously from the same taphole, or separately in different slag and metal tapholes arranged at a vertical distance of 0.5-1.0 m. A ferromanganese producing furnace is schematically shown in Figure 2.11.

In modern plants the different raw material components are weighed out based on chemical analysis of ores, fluxes and carbonaceous agents, and on the desired composition of alloy and slag. The raw material mix is transported to hoppers above the furnace where it is fed by gravity through chutes passing through the furnace cover (Olsen et al. [2007]).

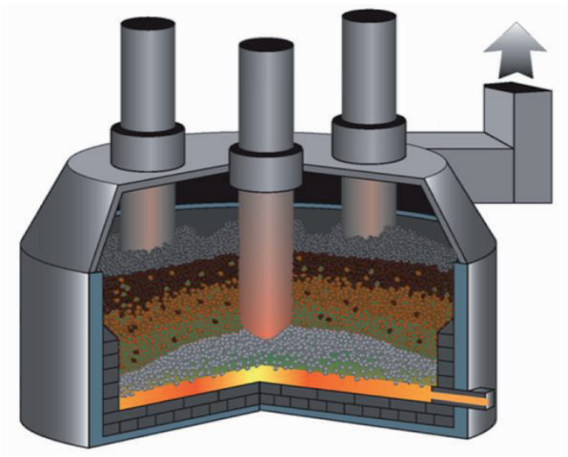

Figure 2.11: Schematic view of a ferromanganese production furnace showing furnace body, electrodes, off-gas system and charge materials (Tangstad [2011]).

Coke is the common source of carbon for the ore reduction, and the commonly used fluxes are limestone and dolomite. These basic fluxes are added to give the slag suitable chemical properties, smelting temperature and viscosity in order to secure good furnace operation and a high manganese yield. The manganese ores vary widely in their content of manganese, iron, silica, alumina, lime, magnesia and phosphorous. One important parameter is the manganese to iron ratio. Blending of ores from different sources is common practice, for instance to obtain a specific Mn to Fe ratio in the metal, e.g. 7:1 for high carbon ferromanganese with 78% Mn. Approximately 500-1000 *kg* of slag is normally produced per tone of metal (Olsen et al. [2007]).

2.8 Physical zones in the ferromanganese furnace

The interior of a furnace producing high carbon ferromanganese consists of two main zones with different characteristics: low temperature pre-reduction zone, and the high temperature coke bed zone. In addition, a metal layer will be present.

Smelting process consists of a combination of several chemical reaction happening inside the furnace. The required energy for chemical reactions mainly comes from electrical energy introduced by electrodes into the charge materials. The main part of electrical energy is dissipated in the part of charge materials close to the

electrodes tips. Therefore the rate of endothermic chemical reactions is higher in these zones. This means that the rate of raw materials flow and metal production is at its maximum close to the electrodes. Accordingly, the gas flow rate will be high along the electrodes (Olsen et al. [2007]). The mass flow in the ferromanganese furnaces has been graphically shown in Figure 2.12.

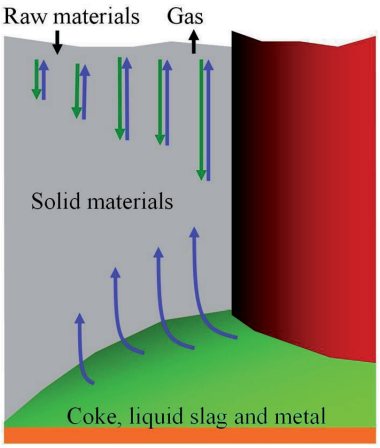

Figure 2.12: Flow of charge materials and reduction gas along one of the electrodes in a ferromanganese production furnace (Olsen et al. [2007]).

Due to temperature gradient, and thus the reactions distribution, the furnace shaft is divided into specific zones as shown in Figure 2.13. Properties of these zones and the most important chemical reactions in these zones can be summarized as follows (Safarian-Dastjerdi [2007]):

- **Pre reduction zone (1)**: Drying, calcination and heating zone, including low temperature reduction of MnO_2 to Mn_2O_3 and some hydrogen-gas formation by the water-gas reaction.
- **Pre reduction zone (2)**: Gas reduction zone, including reduction of Mn_2O_3 and Fe_2O_3, dolomite decomposition and reversed alkali reduction.
- **Pre reduction zone (3)**: Direct reduction zone where Mn_3O_4 and Fe_3O_4 are reduced and the Boudouard reaction runs simultaneously.
- **Coke bed zone**: Smelting reduction zone where MnO and SiO_2 dissolved in the slag are partly reduced to liquid metal, some carbon is dissolved in the metal and K_2CO_3 is reduced to K(g) (alkali circulation).

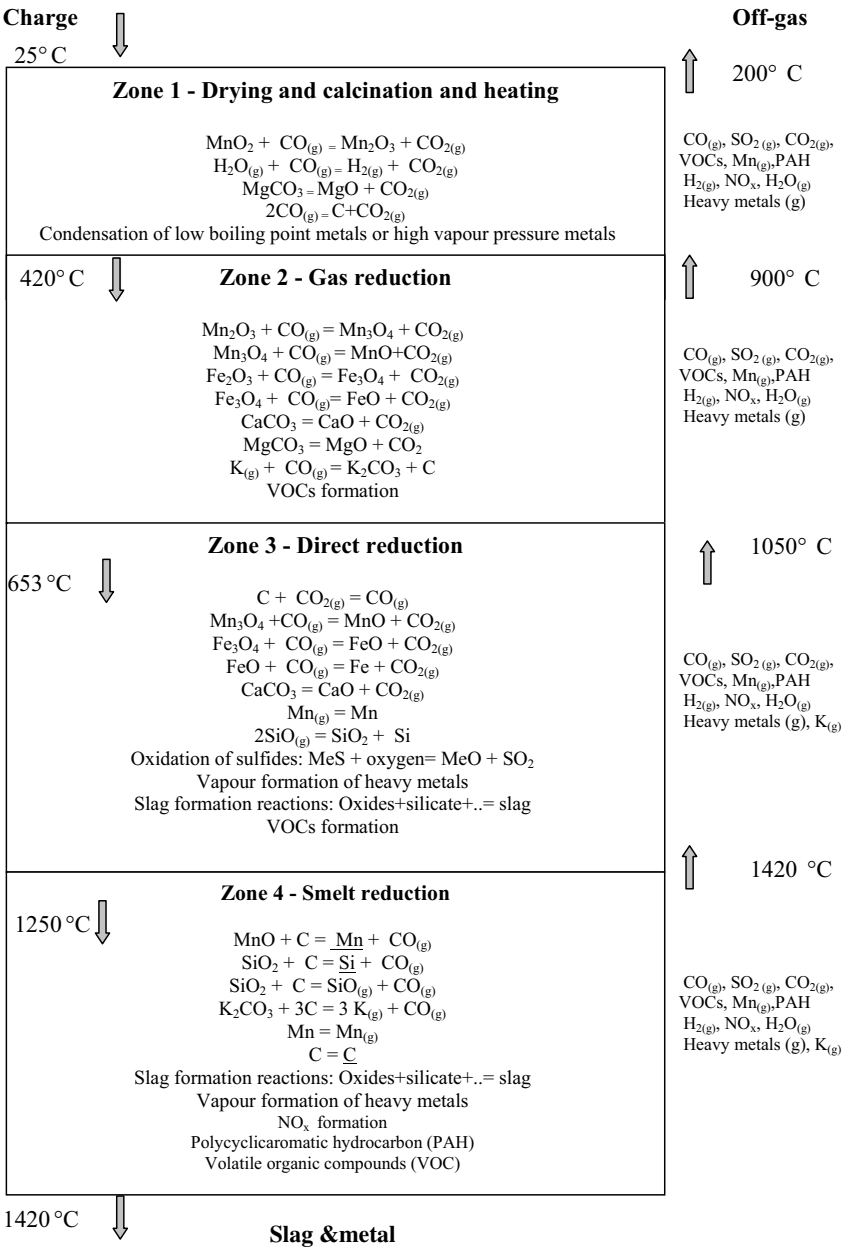

Figure 2.13: The chemical reactions, temperature gradients and gas components in high carbon ferromanganese production process in a submerged arc furnace (Safarian-Dastjerdi [2007]).

2.8.1 Coke bed zone

The coke bed starts approximately at the tip of the submerged electrodes down in the furnace. The manganese ores and fluxes melt together forming an oxide melt- the slag. In this area there will be a bed of coke, slag and metal. These phases may be present in various configurations depending on the history of the operation. Due to the different densities of coke, slag and metal the various layers are often described in the literature as consisting of separate layers, as illustrated in Figure 2.14(A) (Olsen et al. [2007]). However from excavation of a single-phase pilot scale furnace (Tangstad [b] [1996] and Tangstad et al. [2001]) and industrial furnaces (Barcza et al. [1979], Tangstad [a] [1999], Ringdalen and Eilertsen [2001], Olsen and Tangstad [2004]) it has been proven that coke is present all the way down to the metal layer. Often ”dry” bed of coke is present at the top of the coke bed area. The slag to coke ratio increases with decreasing distance to the metal layer, as illustrated in Figure 2.14(B) (Olsen et al. [2007]). The coke bed is ”forced” into the slag layer by the weight of the overburden. Also vertical column of almost pure slag have been formed in the center of the coke bed (Olsen and Tangstad [2004]). The shape and size of coke bed may vary from horizontal layers (Olsen and Tangstad [2004]) to bell shaped (Barcza et al. [1979]) and conical shapes (Ringdalen and Eilertsen [2001]), depending on raw materials, slag chemistry and most of all on the preceding furnace operation, i.e. whether the coke volume in the furnace is increasing, decreasing or is in a stable state.

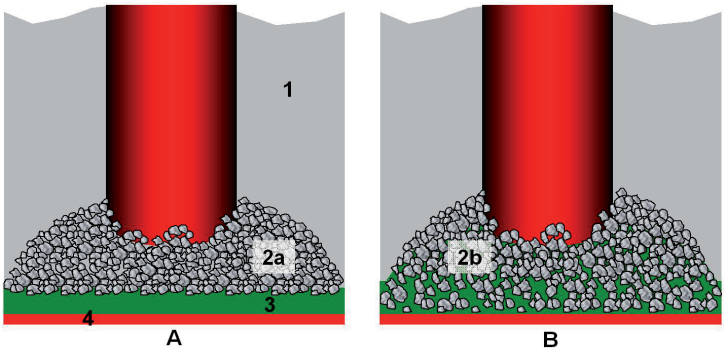

Figure 2.14: Possible coke bed configurations. A) Separate coke bed, slag layer and metal layer. B) Coke bed mixed with slag and separate metal layer. 1-pre-reduction zone, 2a-coke bed with small amount of slag, 2b-coke bed with increasing amount of slag towards the metal layer, 3-slag layer, 4-metal layer (Olsen et al. [2007]).

Slag and metal production in the coke bed zone

The ore and fluxes melt together into a liquid slag on top of the coke bed. The slag will run down through the coke bed. The coke particles are slowly consumed as they move down in the coke bed. The main metal formation also takes place in the coke bed zone. After completed pre-reduction of typical ores, the sum of MnO, SiO_2, CaO, MgO and Al_2O_3 will amount to about 90%. The content of MnO will usually be around 80%. The oxide materials melt down to form a slag phase as the raw materials enter the coke bed zone where the final metal formation reduction takes place (Olsen et al. [2007]):

$$MnO(l) + C = Mn(l) + CO \tag{2.9}$$

The reduction of MnO will start when the slag, with its content of solid MnO-spheres, is sufficiently liquid. The temperature range in this situation is called the incipient reduction temperature as most of the MnO reduction will take place above this temperature. Therefore the slag and metal producing reactions happen mainly in the coke bed zone of the furnace (Olsen et al. [2007]).

Physical properties of the coke bed zone

The coke bed zone consists of porous media made of solid coke particles where the void fraction between the particles has been filled by molten slag. The coke particles forming the coke bed have irregular shape and uneven size distribution (see Figure 2.15).

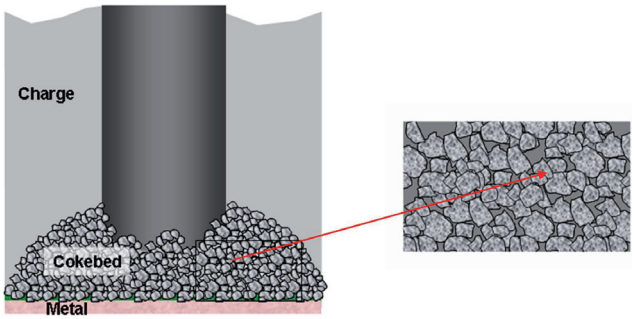

Figure 2.15: Coke bed structure with irregularly shaped and unevenly sized coke particles in a random pattern (Olsen et al. [2007]).

Volume fraction of liquid slag and the coke particles size are depended on spatial position in the coke bed zone. Results of sampling from ferromanganese furnaces show that in the part of coke bed located under the electrodes, the coke particles size is smaller and the slag volume fraction is higher than the rest of coke bed zone (Eramet [2010]).

Chapter 3

Tapping Process in Silicon and Ferrosilicon Production Furnaces

3.1 Tapping process in brief

As a result of the smelting process in a furnace, molten silicon/ferrosilicon is produced. Since silicon and ferrosilicon have higher density compared to charge materials, it is accumulated at the furnace bottom. The melt then must be removed from the furnace for being more processed through ladle refining, casting, granulation, etc. Tapping is the process of removing liquid metal from the furnace. It takes place either intermittently or continuously through a channel connected to the interior of a furnace and the taphole (see Figure 3.1). The tapping channel is opened by some tool such as a steel rod, oxygen lance, electrical graphite electrode or other mechanized or manual equipment (Schei et al. [1998]).

In an industrial silicon/ferrosilicon furnace there are several tapholes located around the furnace body but only one of them is open during tapping. The reason for having several tapholes is that most of the furnaces in use today are rotating furnaces and therefore the taphole which is opened for tapping of melt should be changed in a period of two to five days. Depending on the production type, tapping is done in continuous or discontinuous ways. In the continuous tapping the taphole is open all the time and the metal flows from the furnace inside into the ladle continuously during furnace operation. In the discontinuous tapping the taphole is normally closed and it is opened in special time intervals, i.e 2 *hr*, and produced melt is removed from furnace into the ladle in a period of time, i.e 30 *min*, and then it is closed again. Therefore in this case the furnace taphole is opened and closed

periodically. Closing of an open taphole can be done using automatic system, called mud gun, which injects special clay into the taphole or it can be done manually by inserting a solid paste into the taphole. Figure 3.2 shows tapping process in a silicon producing furnace.

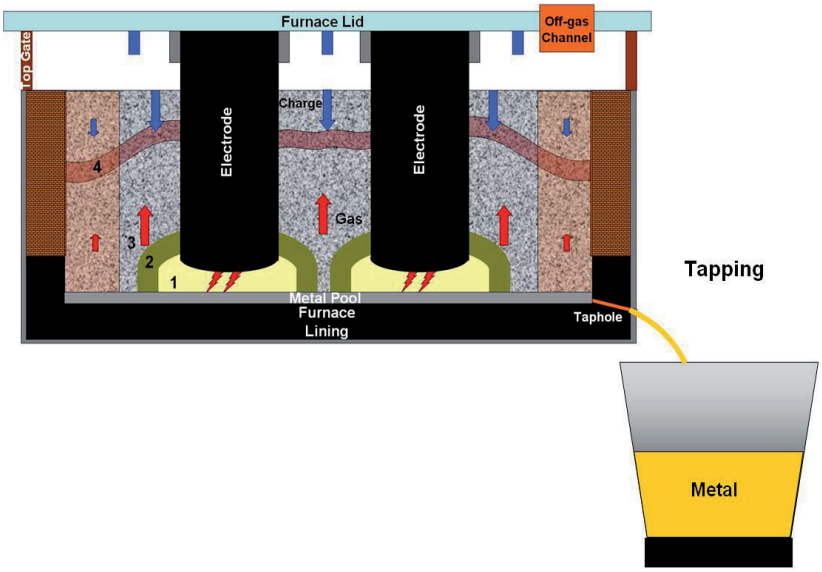

Figure 3.1: Schematic of tapping process in submerged arc furnaces.

Continuous tapping is mostly applied in silicon production furnaces due to two main reasons. The first reason is that opening and closing the taphole using steel rods or oxygen lance is costly and of course leads to inserting metallic impurities into the melt while it is not desired to have high impurity level in silicon melt. The other reason is that due to lower tapping rates of the melt into ladle during continuous tapping, there is enough time for refining of the silicon melt through gas purging into the ladle. Discontinuous tapping is mostly done in ferrosilicon production furnaces. In this study the focus is on discontinuous tapping of melt from submerged arc furnaces.

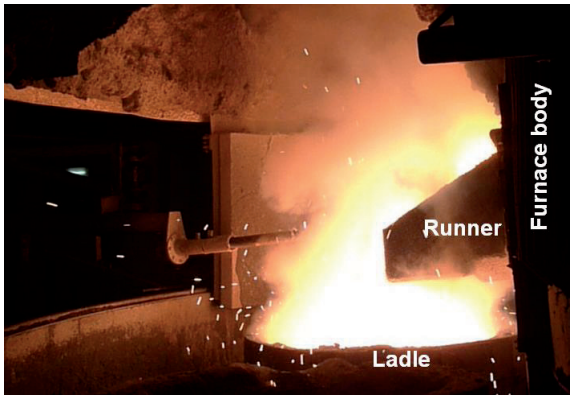

Figure 3.2: A side view of tapping of silicon melt from a submerged arc furnace, very high temperature melt flows into the ladle from the furnace hearth.

3.2 Importance of tapping process

The tapping of the melt from furnace plays an important role in silicon/ferrosilicon production chain. Having a secure and good draining of the produced metal from the furnace is essential to obtain an optimum production yield. Therefore successful tapping guaranties stability of furnace operation which is necessary to have high productivity. In the tapping process a flow of liquid metal with a temperature above 1500°C has to be controlled. This is a considerable challenge and the importance of tapping can be summarized as follows (Tveit et al. [2002]):

- The standard of the tapping process has an impact on the total process performance. If a problem happens during tapping, it influences the whole production chain.
- The tapping process and the use of tapping tools and equipment may influence the melts quality.
- The tapping process includes direct costs and hence influences the overall economy of the plant.
- The tapping area includes some potential hazardous working conditions. The combination of hot metal flow, gas from the taphole and complicated transport operations often makes the tapping area one of the worst places for accidents.

Types of accidents are skin burns and squeeze damage. Also more serious and even fatal accidents may occur in the tapping area.

- Due to the pressure of the process gas inside the furnace, SiO_2-rich gas may blow out through the taphole (Schei et al., 1998). The tapping area is therefore often one of the most important sources for internal pollution in a plant. This may introduce special problems when there is a rotating furnace body, which makes the problem of collection the off-gas from the taphole more difficult.

Considering the above mentioned topics about the importance of tapping process in silicon/ferrosilicon furnaces, a detailed investigation of different aspects of the process is necessary. In order to make a comprehensive study about the furnace tapping, the first step is recognition of different parameters and phenomena which influence the process.

3.3 Issues affecting the tapping process

Any process has a series of characteristics known as the process parameters. Different issues affect a process through influencing one or some of these parameters. The main parameters of discontinuous tapping are the flow rate of the melt from furnace into the ladle, tapping flow rate, and the time needed for completing the process, tapping time. Tapping time and tapping flow rate are linked together and create another parameter which is tapping speed.

After determining the tapping parameters it is important to recognize different issues which affect these parameters. To find those issues start with very simple physical processes which are somehow similar to the target process. In fact tapping of liquid metal from a submerged arc furnace in many ways is similar to draining of water from a cylindrical tank. Using the information coming from such basic case study is helpful in extending the ideas for complicated systems. Consider a tank which has a valve on the sidewall and filled with some water (see Figure 3.3). Velocity of water at the valve outlet and flow rate is the parameters which should be calculated.

For low-viscosity incompressible fluids such as water, the incompressible Bernoulli equation describes the flow. Applying this equation to a ”streamline” that starts at the top free surface and exits out the spout yields:

$$\rho g z_{surface} + p_{surface} = \frac{1}{2}\rho V_{jet}^2 + \rho g z_{spout} + p_{atm} \tag{3.1}$$

Note that the exiting fluid jet experiences the atmospheric pressure while pressure at the free surface of water is not equal to atmospheric pressure.

$$V_{jet} = \sqrt{2(\frac{p_{surface} - p_{atm}}{\rho}) + 2g(z_{surface} - z_{spout})} \tag{3.2}$$

The non-zero viscosity of fluids will reduce mechanical energy of the fluid flow (converting it into heat within boundary layers around the spout walls), hence the fluid jet inside the tapping channel will have a slightly smaller diameter than that of the spout. This factor can be accounted for by a discharge coefficient C_d, whose value is typically between 0.90 and 0.98. The volumetric flow rate Q results from multiplying the jet velocity times the cross-sectional area:

$$Q = A_{jet}V_{jet} = C_d A_{spout}V_{jet} = C_d \pi \frac{D_v^2}{4}\sqrt{2(\frac{p_{surface} - p_{atm}}{\rho}) + 2g(z_{surface} - z_{spout})} \tag{3.3}$$

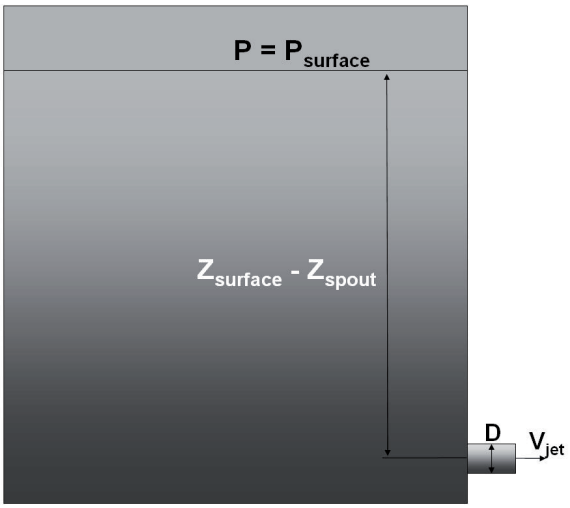

Figure 3.3: A tank filled with water, the pressure at the water surface is higher than the atmospheric pressure.

The result of this simple case study shows that the flow rate of water at the valve outlet is determined by the level of water in the tank, diameter of the valve and pressure difference between the water surface and the valve outlet. The valve diameter D_v is a geometrical issue which is constant for a given system. Therefore

any change in the height of water in the tank and the pressure on the water surface influences the draining rate of water.

Tapping of melt from a furnace is more complicated than calculating the water flow rate from a tank. However, using the results obtained from this simple system implies that the tapping speed is affected by the conditions inside the furnace. For a given furnace geometry the main issues which can affect the tapping speed are described as follows.

3.3.1 Metal height

According to Equation 3.3 the liquid height affects the liquid flow rate. This effect has been simply shown in Figure 3.4 where water flows out of a bottle through several holes which exist on the bottle surface. It can be seen that the water flow rate is depended on the vertical position of the holes because of hydrostatic pressure made by the column of water.

Figure 3.4: The effect of liquid height on the exiting flow rate from the holes made on the surface of a bottle of water.

Molten metal is the main product of smelting process in a submerged arc furnace. As long as the furnace taphole is not opened the produced melt is accumulated on the furnace bottom and hence the metal height increases. The hydrostatic pressure made by the metal height in the furnace acts as a driving force to increase the tapping flow rate. The positive effect of metal height on the tapping speed imply that having delay in opening the furnace taphole, which causes higher metal height

in the furnace, leads to more efficient tapping. But it has been industrially experienced that when the metal height in silicon and ferrosilicon furnaces increases more than a limit the rate of backward reaction 3.4 increases (Tveit et al. [2002]).

$$SiO_2(s,l) + Si(l) = 2SiO(g) \tag{3.4}$$

Increased rate of this reaction is accompanied with generation of huge amount of SiO gas which will normally increase production of silica-dust to the filter and hence lower the silicon yield. This phenomenon will have an impact on the carbon balance. An increase in the SiO-loss from the furnace will reduce the amount of carbon needed by the process. In addition since reaction 3.4 is extremely endothermic, the huge amount of energy needed for this reaction may reduce the process temperature in the hot zone which is very unfavorable for the total process performance (Tveit et al. [2002]). Therefore it is unfavorable to have very high metal height in the furnace before starting tapping and hence the time intervals between the taps in discontinuous tapping are influenced by the metal height inside the furnace.

3.3.2 Permeability of the packed beds

It was discussed before that in the submerged arc furnaces different porous zones of charge particles are formed. Physical properties of each zone depend on its position in the furnace. A porous medium consists of a matrix with a large amount of pores and throats in fact it consists of many twisted and interconnected pores of varying diameter and cross sectional shape (see Figure3.5). Likewise, the flow paths in a bed of unconsolidated granular particles can be thought of as a collection of such pores. The relationship between flow rate through the porous medium and the driving pressure will depend on the structure of these pores. Therefore description of flow in porous media is extremely difficult. Even though flow in a single pore is given by simple equations assuming simplified tube structure, the network of the pores is practically impossible to model in detail. The pathlines of liquid flow in a very simplified 2D model of a porous bed of solid particles is shown in Figure 3.6. It can be seen from this figure the liquid flow direction in the bed changes while passing through the pores. It simply expresses the resistance against fluid flow which causes pressure drop in porous medium.

In porous medium there is a resistance against fluid flows. The resistance is created due to existence of solid particles in the porous beds. Physical properties of porous beds such as the void fraction between the solid particles which can be filled with fluid, porosity, and the particles size are important parameters in determining

permeability of the beds. In fact permeability of porous beds is the factor which is used to define the resistance against the fluid flow in a bed as well as a scale to compare different beds. The role of permeability is more important if the fluid which passes through the porous bed has high viscosity.

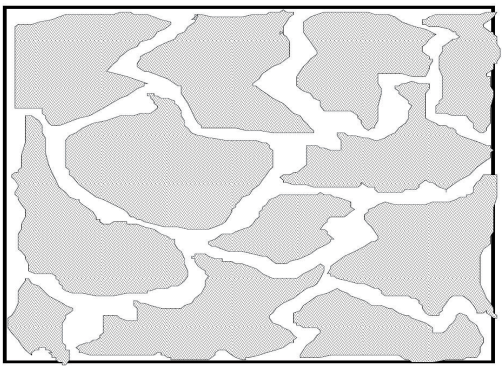

Figure 3.5: Schematic view of a solid porous bed, gray color shows the solid particles and white color represents the void fraction between the solid particles.

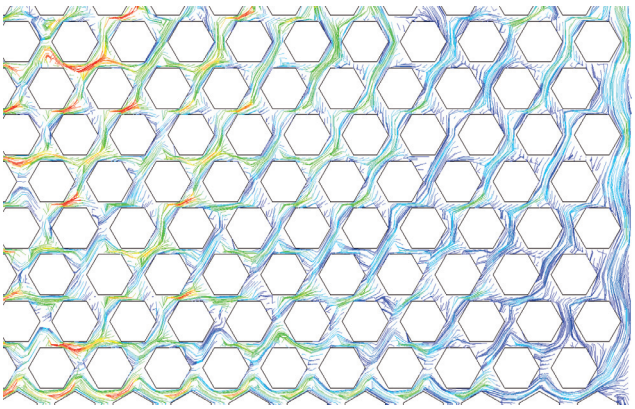

Figure 3.6: Enlarged pathlines of fluid flow in a porous medium, the black lines show the boundaries of solid particles and the space between them is the void fraction where the fluid flows through it. The fluid source is on the top and the sink in the lower left side of the bed. Fluid velocity in the bed is higher (red color) close to the sink and it is low (blue color) in the opposite side of the bed.

Permeability of the packed beds of charge materials in the furnace affects the

tapping speed both directly and indirectly. The direct effect is the resistance against the melt flows from the furnace crater zone towards the taphole made by the porous bed of SiC particles which exists on the furnace bottom. Any change in the permeability of the furnace bottom bed leads to increased or decreased tapping flow rate. Permeability of the porous beds formed in the upper part of charge materials affects the tapping speed indirectly through influencing the crater pressure.

3.3.3 Furnace crater pressure

Equation 3.3 shows that the exiting flow rate from a tank of water is depended to the pressure on the water surface. In the case of tapping from a submerged arc furnace the crater pressure is directly inserted on the melt surface which is accumulated on the furnace bottom. This external pressure can act as another driving force to increase the melt flow rate during furnace tapping.

3.4 Tapping gas problem

The above mentioned issues in addition to affecting the tapping speed can cause problems for tapping process as well. One of the main problems which sometimes happens during tapping of silicon and ferrosilicon furnaces is ”taphole gassing” phenomenon. Taphole gassing is known as the situation during tapping when in addition to the melt a significant volume of process gases are released from the furnace taphole. Therefore the phenomenon includes blowing-out of high velocity and high temperature jet of a gas from the taphole. The gas is composed of SiO and CO which due to its high temperature reacts with oxygen in the air and produces fine SiO_2 particles and a gas rich of CO_2 (Tveit et al. [2002]). Taphole gassing phenomenon is schematically shown in Figure 3.7.

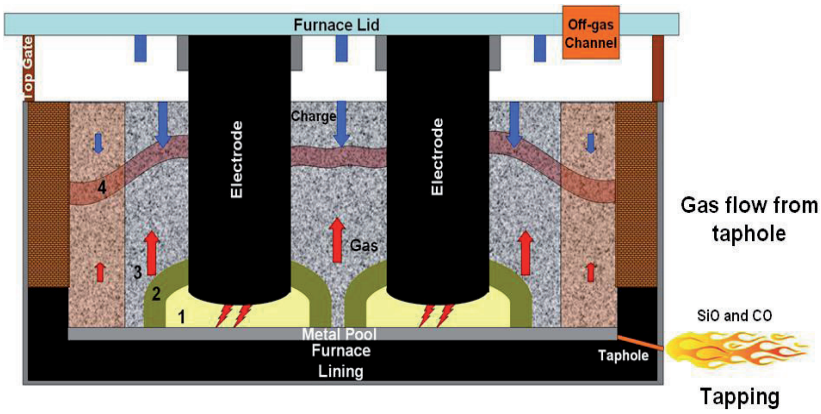

Figure 3.7: Taphole gassing phenomenon in silicon and ferrosilicon producing furnaces is known as one of the problems related to the tapping.

3.4.1 Root reasons for taphole gassing phenomenon

It was discussed earlier that the furnace crater pressure is quite high during smelting process. Normally process gases pass through charge materials and move towards the off-gas system at the furnace top. When the furnace taphole is opened for tapping of melt a pressure drop will happen in the region close to the taphole comparing the other internal zones of the furnace. Existence of high pressure gas in the crater zone and the mentioned pressure drop near the taphole creates the potential for the process gases to escape through the taphole.

Crater walls act as a resistance against the gas flows from crater zone but process gases usually form several channels in the crater wall (Tranell et al. [2010]) and the charge materials covering the crater zone, to flow out of crater zone. Another reason for formation of these ”trumpet”-shaped channels (Tveit et al. [2002]) can be increases taphole length due to operators activity during tapping. However high gas pressure in the crater zone accompanied with described phenomenon is the root reason for occurring the taphole gassing phenomenon.

3.4.2 Different aspects of taphole gassing phenomenon

Taphole gassing phenomenon affects the production process in aspects of safety, environment and economy in different ways. When taphole gassing happens a rapid combustion of SiO and CO gas occurs according to the following reactions:

$$SiO(g) + 1/2O_2(g) = SiO_2(s) \tag{3.5}$$

$$CO(g) + 1/2O_2(g) = CO_2(g) \tag{3.6}$$

Produced SiO_2 is in the form of very fine particles and CO_2 is a high temperature gas. Therefore the taphole gassing phenomena is known as an important internal source of pollution in the silicon production plant.

Sometimes taphole gassing is started suddenly after the taphole is opened and sometimes in the middle of tapping process while there is no special sign for the phenomenon and in severe cases the length of the blowing jet of hot gas can reach up to several meters. Therefore it can create a dangerous condition for the operators who are working in the tapping area. Previous studies have reported several accident and human injuries due to taphole gassing (Tveit et al. [2002]).

Process gases composed of SiO and CO gas are intermediate product of the furnace operation. SiO gas is recovered through reaction with carbonaceous materials in the charge and CO gas reacts with iron ore, in ferrosilicon production, before escaping from the furnace top. During the gassing phenomena process gases will find their way out of furnace through the taphole. Therefore energy and materials are wasted and the taphole gassing affects the economy of the silicon production as well.

3.5 Insight into investigation of tapping process

Regarding the described phenomena and different issues in this chapter, it is clear that any attempt for investigation of tapping process in silicon and ferrosilicon furnaces should include the role of in-furnace conditions. There are empirical and fundamental approaches which can be used for investigation of a system. Empirical approach applies experimental studies for understanding and describing different phenomena. However there are many limitations in doing different experiments in high temperature and large scale systems such as submerged arc furnaces. Fundamental approach basically applies theoretical models based on mathematical formulation of a physical phenomenon in order to explain it. In this approach normally several assumptions and simplifications for the system under consideration is made. The degree of accuracy of in this approach depends on the developed models and applied assumptions. However validity of fundamental approach is determined through comparing the results of this approach with the real phenomenon.

The approach which is used in this study is a combination of fundamental and empirical approaches. Therefore theoretical models of different physical phenomena inside the furnace are developed. The models are built based on the basic physical rules applicable for the furnace. In the modeling process the best of available knowledge about the conditions of inside the furnace coming from academic literature, industrial experiments and scientific observations are employed. The modeling approach is based on Computational Fluid Dynamics (CFD) technique as a powerful tool for investigation of the systems involving fluid flows, chemical reactions and transfer phenomena. The results of other industrial tests and observations are then used as criteria in order to show validity of developed models in this study.

Chapter 4

Computational Fluid Dynamics (CFD): Principles and Applications

4.1 Introduction

THE Physical aspects of any fluid flow are governed by three fundamental principles: Mass conservation, Energy conservation and Newton's second law. These fundamental principles can be expressed in terms of mathematical equations, which in their most general form are usually partial differential equations. Computational Fluid Dynamics (CFD) is the science of determining a numerical solution of the governing equations of fluid flow whilst advancing the solution through space or time to obtain a description of the complete flow field of interest.

The governing equations for Newtonian fluid dynamics, the unsteady Navier-Stokes equations, have been known for over a century. However, the analytical investigation of reduced forms of these equations is still an active area of research as is the problem of turbulent closure for the Reynolds averaged form of the equations. For non-Newtonian fluid dynamics, chemically reactive flows and multiphase flows theoretical developments are at a less advanced stage.

Experimental fluid dynamics has played an important role in validating the limits of the various approximations to the governing equations. The wind tunnel, for example, as a piece of experimental equipment, provides an effective means of simulating real flows. Traditionally this has provided a cost effective alternative to full scale measurement. However, in the design of equipment that depends critically on the flow behavior, for example the aerodynamic design of an aircraft, full scale measurement as part of the design process is economically impractical. This situa-

tion has led to an increasing interest in the development of a numerical wind tunnel (Date [2005]).

The steady improvement in the speed of computers and the available memory size since the 1950s has led to the emergence of computational fluid dynamics. This branch of fluid dynamics complements experimental and theoretical fluid dynamics by providing an alternative cost effective means of simulating real flows. As such it offers the means of testing theoretical advances for conditions unavailable on an experimental basis (Date [2005]).

The role of CFD in engineering predictions has become so strong that today it may be viewed as a new third dimension of fluid dynamics, the other two dimensions being the above stated classical cases of pure experiment and pure theory. The development of more powerful computers has furthered the advances being made in the field of computational fluid dynamics. Consequently CFD is now the preferred means of testing alternative designs in many engineering companies before final, if any, experimental testing takes place.

4.2 Fundamentals of CFD

Fluid flows in different systems are determined through solving a set of partial differential equations (PDEs) which govern physical state of the system. In order to simulate the behavior of the fluid flows in the system, the set of governing equations must be solved simultaneously. In real systems there is normally no analytical solution for the governing partial differential equations (PDEs) and therefore numerical solutions must be applied. Computational Fluid Dynamics (CFD) is the art of replacing such systems of PDEs by a set of algebraic equations which can be solved using computers. The system domain is then decomposed into a large number of cells/elements and the algebraic equations are solved within these cells by applying proper boundary conditions. The quality of simulation results depends on the mathematical model, underlying assumptions, approximation type, stability of the numerical scheme and cell size. There are two types of CFD codes which can be used for solving engineering problems; self-made code or general purpose commercial code. Self-made code requires a great amount of time and knowledge, but can be very efficient in solving a specific problem. General purpose commercial CFD codes have the advantage of being well developed and flexible. There are several commercial general purpose CFD packages available on the market.

The general partial differential equations governing fluid flows in a system are briefly presented in this section. Depending on the properties of the systems under

consideration in this research, different CFD models are employed. The equations used in each model are described with more details in the related chapters.

For flows involving species mixing or reactions, a species conservation equation is solved for, if the non-premixed combustion model is used, conservation equations for the mixture fraction and its variance are solved. Additional transport equations are also solved when the flow is turbulent.

4.2.1 Mass conservation equation

The equation for conservation of mass, or continuity equation, can be written as follows:

$$\frac{\partial \rho}{\partial t} + \nabla \cdot (\rho \vec{v}) = S_m \tag{4.1}$$

Equation 4.1 is the general form of the mass conservation equation and is valid for incompressible as well as compressible flows. The first term on the left hand side represent the rate of increase of mass in a fluid element, the second represents rate of flow of mass into a fluid element. For incompressible fluids the density is constant and the first term is zero. The source S_m is the mass added to the continuous phase from the dispersed second phase (e.g., due to vaporization of liquid droplets) and any other sources.

Species equation

The species equation describes that the rate of change of the mass of the chemical species per unit volume is equal to the rate of generation of the chemical species minus the convection and diffusion fluxes per unit volume.

$$\frac{\partial}{\partial t}(\rho Y_i) + \nabla \cdot (\rho \vec{v} Y_i) = -\nabla \cdot J_i + R_i + S_i \tag{4.2}$$

The first left hand term in Equation 4.2 represents the rate of increase of species i into the fluid element; the second term the net rate of flow of species i out of the fluid element due to convection. On the right hand side the first term describes the rate of increase of species i due to diffusion. R_i is the net rate of production of species i by chemical reaction and S_i is the rate of creation by addition from the dispersed phase plus any user defined sources. The diffusion flux of species i, J_i, can be written as:

$$\vec{J_i} = -\rho D_{i,m} \nabla Y_i \tag{4.3}$$

for laminar flows where Y_i is mass fraction of species i, $D_{i,m}$ is diffusion coefficient for species i.

4.2.2 Momentum conservation equation

Conservation of momentum in an inertial (non-accelerating) reference frame is described by Equation 4.4. The momentum equation (Navier-Stokes equation) satisfies Newtons second law; the rate of change of momentum equals the sum of forces acting on an element.

$$\frac{\partial}{\partial t}(\rho\vec{v}) + \nabla \cdot (\rho\vec{v}\vec{v}) = -\nabla p + \nabla \cdot (\bar{\tau}) + \rho\vec{g} + \vec{F} \tag{4.4}$$

Where p is the static pressure, $\bar{\tau}$ is the stress tensor (described below), and $\rho\vec{g}$ and $\vec{F}$ are the gravitational body force and external body forces (e.g., that arise from interaction with the dispersed phase), respectively. $\vec{F}$ also contains other model-dependent source terms such as porous-media flow resistance and electromagnetic sources.

The stress tensor $\bar{\tau}$ is given by:

$$\bar{\tau} = \mu\left[(\nabla\vec{v} + \nabla\vec{v}^T) - \frac{2}{3}\nabla \cdot I\right] \tag{4.5}$$

where μ is the molecular viscosity, I is the unit tensor, and the second term on the right hand side is the effect of volume dilation.

4.2.3 Energy conservation equation

The energy conservation equation satisfies the first law of thermodynamics; the rate of change of energy equals the sum of the rate of heat addition to and the rate of work done on a fluid element. It is given by:

$$\frac{\partial}{\partial t}(\rho E) + \nabla \cdot (\vec{v}(\rho E + p)) = -\nabla \cdot \left(k_{eff}\nabla T - \sum_j h_j\vec{J}_j + (\bar{\tau}_{eff} \cdot \vec{v})\right) + S_h \tag{4.6}$$

The first term in the left hand of Equation 4.6 is the rate of increase of enthalpy in fluid element; the second term is the convective heat into the fluid element. The first term in the right hand represents the energy transfer due to conduction, species diffusion and viscous dissipation. The second term in right hand is the volumetric heat source. In which total energy E is defined as:

$$E = h - \frac{p}{\rho} + \frac{v^2}{2} \tag{4.7}$$

where k_{eff} is effective conductivity, $\vec{J_j}$ is diffusion flux of species j, S_h is heat source and h_j is species enthalpy.

$$h_j = \int_{T_{ref}}^{T} C_{p,j} dT \tag{4.8}$$

Where sensible enthalpy $h = \sum_j Y_j h_j$ for ideal gasses and $h = \sum_j Y_j h_j + \frac{p}{\rho}$ for incompressible fluids.

4.3 Applications of CFD in metallurgy

CFD has for several years been used in process industries for simulation and optimization of different categories of processes. In some field such as ladle metallurgy or continuous casting of steel, it has been used for many years. For other processes, such as submerged arc furnaces, research was done much later but due to its high complexity has not been extensively studied. Modeling of single and multi-phase flows in furnaces, heat and mass transfer and chemical reactions in the furnace is done using CFD. Some examples of its applications in metallurgical industries are iron and steel making (Blast furnace, HIsmelt, Basic Oxygen Furnace, Electric Arc Furnace), continuous casting of steel (tundish, casting mould), ladle metallurgy (gas and electromagnetic stirring), non-ferrous smelting processes (Flash smelting, Hall-Heroult cell, Peirce-Smith converter), off-gas cooling, dust precipitation (waste-heat boilers, cyclones, electrostatic precipitator), hydrometallurgy (stirring tanks, thickeners, tank-house) etc (Scheepers [2008]). A series of applications of CFD in modeling of submerged arc furnaces and tapping process in different systems are briefly reviewed in this section.

4.3.1 Using CFD in modeling of submerged arc furnaces

Scheepers [2008] developed a single phase CFD model for describing the reaction zone and transfer phenomena in a submerged arc furnace used in phosphorous production. In this model a uniform packed bed with a fixed porosity was considered as the charge materials in the furnace. Through defining heat sources under the electrodes, energy sinks and sources due to different chemical reactions and also proper thermal conductivity for charge materials, temperature distribution in the

charge was determined. Based on findings from the heat distribution in the bed of charge materials a narrow gas-solid reduction zone in the furnace, where very fast ore reduction reaction takes place over a small temperature gradient, was proposed. Reduction of phosphorous ore while moving downward in the furnace and the reduction zone are shown in Figure 4.1.

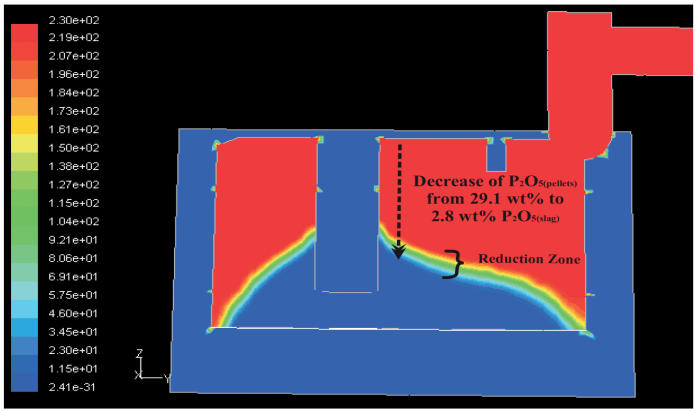

Figure 4.1: A cross-section of the ore concentration as it is consumed by the reaction. The units on the left are kg of P_2O_5 in the ore per cubic meter (Scheepers [2008]).

Andresen [1995] developed a dynamical two-dimensional cylinder symmetric model for high temperature zone of submerged arc furnaces used in silicon production. He simulated the temperature distribution and the rate of chemical reactions very similar to what is believed to exist around one of the electrodes in an industrial furnace. The area comprised a gas filled cavity surrounding the lower tip of the electrode, the metal pool underneath and the lower part of the materials above the crater zone. A sketch of the 2D crater zone and the symmetrical geometry used for modeling is shown in Figure 4.2.

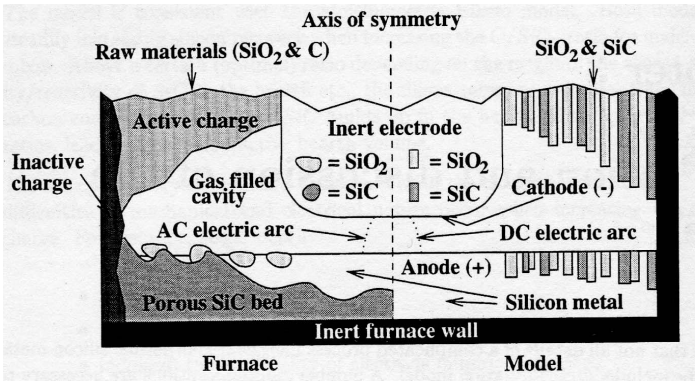

Figure 4.2: Graphical view of the crater zone of a silicon producing furnace and the 2D geometry developed for CFD modeling (Andresen [1995]).

He studied the heterogeneous chemical reactions taking place in the high temperature zone, evaporation and condensation of silicon, transport of materials by dripping, turbulent and laminar fluid flows, DC electric arcs and heat transfer by convection, conduction and radiation in this zone. An example of the results obtained from their study is presented in Figure 4.3.

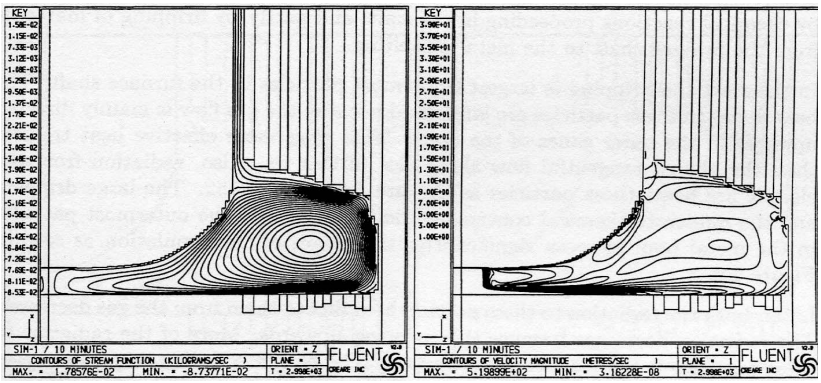

Figure 4.3: Stream functions of flow field (left) and gas velocity magnitude (right) in the furnace crater zone (Andresen [1995]).

Yang et al. [2004] developed an overall process model to simulate inter-linked transport processes of fluid flow, heat transfer and reduction kinetics within the submerged arc furnace used in ferrochromium production. The application of reac-

tion kinetic data to simulate the chromite pellet/lumpy ore reduction with CO gas was presented. It was then further adjusted to provide a sub model for a flow and heat transfer simulation for the packed bed by using computational fluid dynamics (CFD) technique.

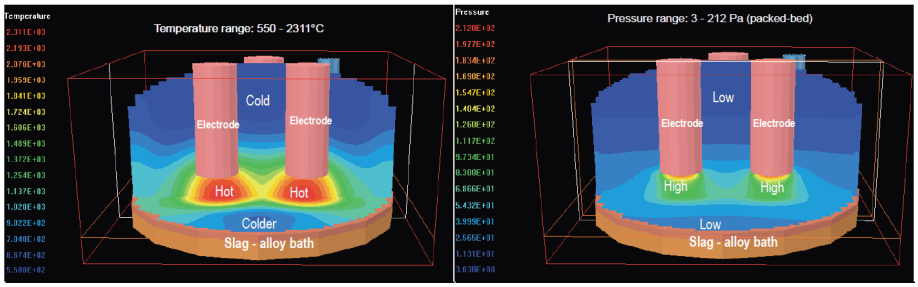

Figure 4.4: Predicted temperature and pressure distributions across electrodes and above slag layer in a ferrochromium production furnace (Yang et al. [2004]).

Their comprehensive process model was aimed to simulate materials and gas flow, temperature and energy distribution throughout the furnace system. They could develop a preliminary model for gas flow and temperature distribution for the upper part of a 20 MW furnace (the packed bed) for high carbon ferrochromium production under simplified conditions. Figure 4.4 shows the model prediction of the temperature and pressure distribution in the furnace.

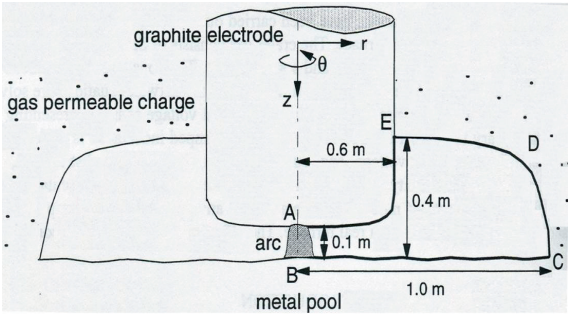

Figure 4.5: Sketch of the silicon furnace crater zone and the domain (A-B-C-D-E) which has been used for modeling (Larsen [1996]).

Larsen [1996] developed a 2D CFD model for an alternating current (AC) free-burning arc in a silicon metal furnace. The crater gas consisted of Si-O-C com-

pounds and the arc were burning between the graphite electrode and the silicon melt (see Figure 4.5).

The conservation equations for mass, momentum and energy together with the time-dependent Maxwell equations were solved in their model. The total arc voltage and current, the current density distribution, temperature, pressure and velocity fields were calculated as a function of time. They concluded that the pressure in the arc was considerably higher than 1 bar and also they mentioned that transport phenomena are crucial for the chemical process in the furnace crater zone. Contours of constant temperature in the arc zone at different times as a result of their research is shown in Figure 4.6.

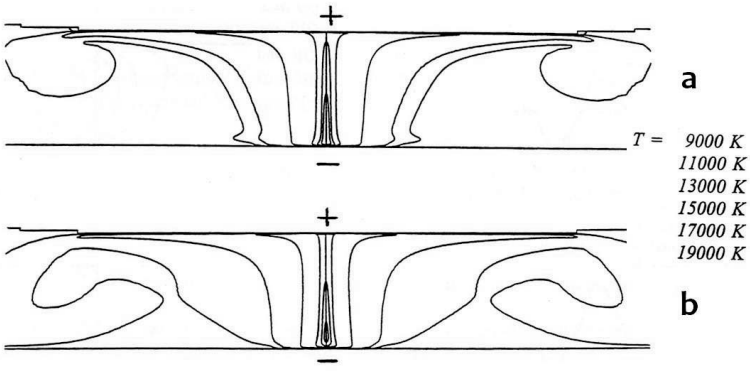

Figure 4.6: Contours of constant temperature at different times and different arc currents, a) t=51 ms, i=-79kA and b) t=56 ms, i=-42kA (Larsen [1996]).

4.3.2 Using CFD in modeling of tapping process

Application of CFD in modeling of the tapping process has been reported in some studies. Most of the studies about the tapping have focused on blast furnaces. Zhou et al. [2010] developed a single phase 3D comprehensive computational fluid dynamics model for simulating the blast furnace hearth. It included both the hot metal flow and heat transfer through the refractories. They divided the furnace hearth into different porous zones with different physical properties. 2D and 3D views of the furnace geometry, different zones and physical properties of each zone are displayed in Figure 4.7.

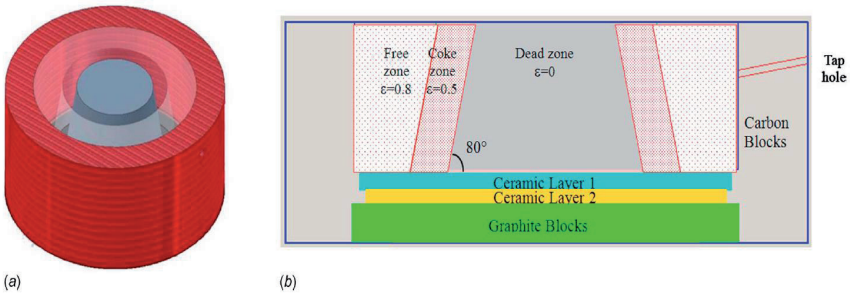

Figure 4.7: Graphical view of a blast furnace hearth composed of different porous zones of coke particles (Zhou et al. [2010]).

As a result of the research they could predict the melt temperature and velocity field in the furnace hearth as well as the temperature distribution in the wall refractories. Figure 4.8 shows the velocity and temperature field extracted from their model.

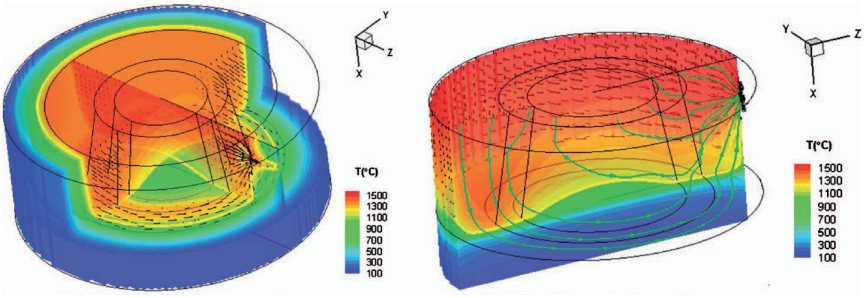

Figure 4.8: Temperature and velocity fields in the blast furnace hearth resulted from a 3D single phase CFD model (Zhou et al. [2010]).

Nishioka et al. [2005] developed a model for the tapping process in blast furnaces based on the basic characteristic features of drainage in the furnace hearth. They used both two-dimensional and three-dimensional CFD models to simulate molten iron and slag flow in the hearth of a blast furnace. Since the furnace taphole has not been considered in the model geometry, the model could not predict the pressure drop across the taphole channel. Therefore they developed a separate model to evaluate the mentioned pressure drop. Their results indicated that the drainage behavior and residual iron and slag volume were affected by the conditions

in the hearth. Also it was found that decrease of the coke particles diameter causes increase of the residual slag volume and a decrease of the residual iron volume. Velocity vectors, metal-slag and gas-slag interfaces as the result of their research are shown in Figure 4.9.

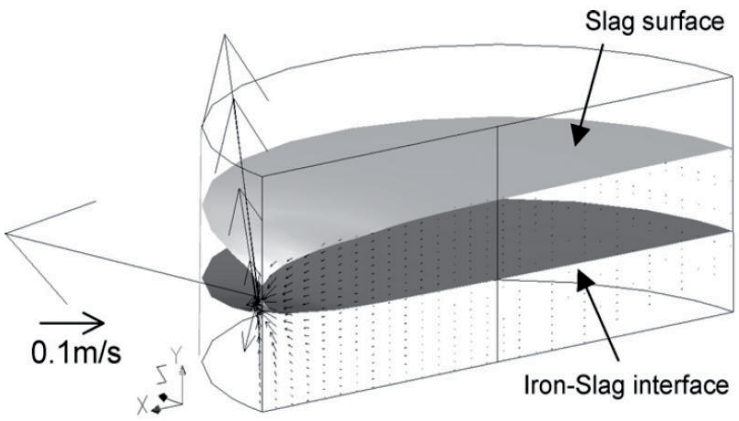

Figure 4.9: Interfaces between gas-slag and slag-metal and the velocity vectors due to melt flows in a blast furnace hearth (Nishioka et al. [2005]).

Searching in the literature shows that different aspects of submerged arc furnaces have been extensively studied in the past but there is no existing comprehensive study about the tapping process including the main affecting parameters. Therefore there is a need for a model which can describe the tapping in submerged arc furnaces and its related physical phenomena in a scientific way.

Chapter 5

Modeling and Industrial Measurements of Tapping Speed in Silicon and Ferrosilicon Producing Furnaces

5.1 Introduction

SIMILARITIES between furnaces used in silicon and ferrosilicon production leads to having the same model developing procedure for these furnaces. In the present study full 3D multiphase flow models of silicon and ferrosilicon furnaces are developed. The models are based on computational fluid dynamics (CFD) and fluid flows and interactions between the phases are therefore investigated. The modeling process consists of making the furnace geometry, selection of the physical models regarding the assumptions and simplifications of the real system, developing user-defined sub models, considering proper boundary conditions and explaining the model results. Geometry of the furnace has been constructed using Gambit 2.4.6 which is a pre-processor for simulating software. Fluid flows in the furnace have been numerically simulated by using Fluent 6.3.26 which is a commercial CFD software. Fluent has standard physical models and the solver to solve most of the required governing equations. In the case where some modifications to the existing models have been required, sub models in the form of user defined functions (UDFs) have been developed and applied.

In addition to theoretical modeling, the results of industrial tests from differ-

ent furnaces are used. The industrial measurements have been set based on the need to have a better understanding of phenomena in order to develop the model. In addition the measurements should serve to both make the CFD model (furnace crater pressure measurements) and validate the model (continuous tapping weight measurements).

5.2 Basis of the model

The model has been constructed based on the available knowledge about the furnaces, process calculations and some hypotheses. The fundamental considerations have been mostly described earlier in Chapter 2. The detailed basis applied in the modeling procedure is explained in the following.

5.2.1 Furnace geometry

Details about the furnace geometry, such as furnace diameter, size of electrodes and taphole diameter, i.e. outer furnace information, are available from the structural design of the furnace. In the current research the geometries are taken from typical industrial size silicon and ferrosilicon production furnaces. Sketch of the furnace geometry used in the modeling process is shown in Figure 5.1 and details about the geometry of the furnaces used in this study are given in Table 5.1.

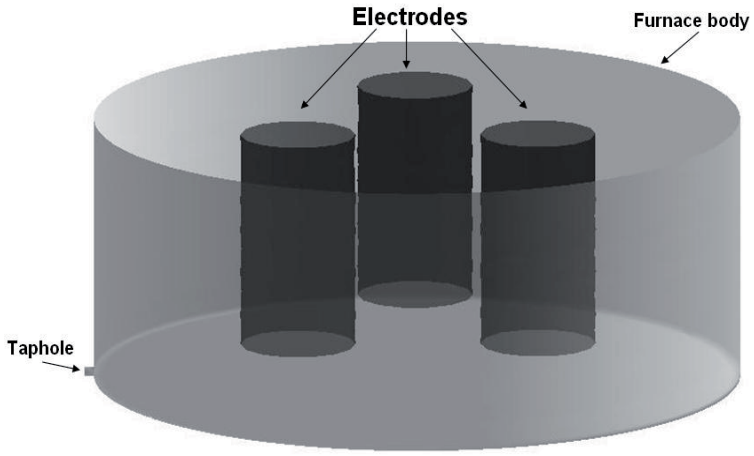

Figure 5.1: 3D geometry of a silicon or ferrosilicon production furnace used in the model.

Table 5.1: Detailed geometry of silicon and ferrosilicon furnaces used in CFD modeling

Furnace type	Furnace diameter (m)	Furnace height (m)	Electrode diameter (m)	Taphole diameter (m)	Taphole length (m)
Silicon	10.5	3.2	1.8	0.11	0.30
Ferrosilicon	8.0	3.0	1.3	0.10	0.25

5.2.2 Conditions inside the furnace

The conditions of inside the furnace represents the situation of the charge materials in different zones of the furnace regarding the temperature distribution and described chemical reactions. Physical properties of charge materials and chemical reactions rates play important roles in determining the gas and liquid flows in different zones of the furnace and hence the pressure build up in the crater zone. Therefore choosing the proper parameters is an essential step in the modeling process.

Size of raw materials

The main raw materials used in silicon and ferrosilicon production are quartz and carbonaceous materials as reductant. The process requirements for the quartz and quartzite are related to size and strength (Schei et al. [1998]). The thermal strength is of special importance as it can affect the gas flow in the charge if too much quartzite fines are present. If the quartzite melts too high up in the furnace, this is not favorable for the process operation. Undersized material is normally unwanted and may be sieved and removed before being fed into the furnace. The normal size of quartzite varies from 10 to 150 *mm*.

The quality of reduction materials is commonly considered to be important to achieve a high silicon yield in the furnace (Schei et al. [1998]). Both the size and reactivity of the carbon used will affect the process performance. The size of carbon will vary from 1 *mm* up to 30 *mm*. The specific surface is increased by decreasing the size of the material. Due to high gas velocity in the furnace, fluidized small particles may be carried into the gas outlet. This may lead to losing control with the amount of carbon supplied to the process. According to Johansen et al. [1991], the critical minimum size for charcoal particles can be 1.5 *mm* to avoid this problem.

Process information

There is available information from the process about the production rates of silicon, ferrosilicon and process gases. Calculations regarding the metal and gas production for different working conditions in silicon and ferrosilicon furnaces have been widely discussed in the literature (Schei et al. [1998]). The production rate of process gases influences the gas flows and hence the reactions rate in different zones of the furnace as well as pressure build up in the crater zone. There is available theoretical predictions and operational data from industry for the production rate of process gases in the furnace. The average melt production in the furnace has been extracted from industrial data and has been used in the model development.

Physical properties of charge materials in different zones of the furnace

It was described in Chapter 2 that the physical properties of the charge materials are depended on the spatial position of the charge in the furnace. This is due to several phenomena such as softening and melting of ore, condensation of process gases and different chemical reactions in different zones of the furnace. There is limited information about the particles size and charge porosity in different zones of the furnace, and information are mostly from the results of furnace excavations (Zherdev et al. [1960]), (Otani et al. [1968]), (Schei [1967]) and (Tranell et al. [2010]). The most important result of furnace excavations is the component distribution in different zones of the furnace charge.

Although the furnace excavation provides valuable information about the furnace, but these results show the conditions of inside the furnace few days after the furnace has shut down. Within this period the charge has cooled down to lower temperatures and then the furnace digging out has been started. Particles size and porosity of the charge materials in the upper part of the charge can be extracted from the furnace excavation results. However decreased porosity of the charge and gluing of the particles near the furnace crater zone due to cooling makes the furnace excavations different from the conditions inside the furnace during real operation.

In the current model we have tried, using the limited available information, to simulate the conditions inside the furnace as close as possible to a real operating furnace. The physical properties of each zone have been defined based on the furnace excavation results, wherever it is possible. Therefore some assumptions and simplifications have been made in order to build model of such a complex system.

In the model the furnace charge has been divided into two main parts. The active part is the column of charge materials located in the central zone of the furnace (see

Figure 5.2).

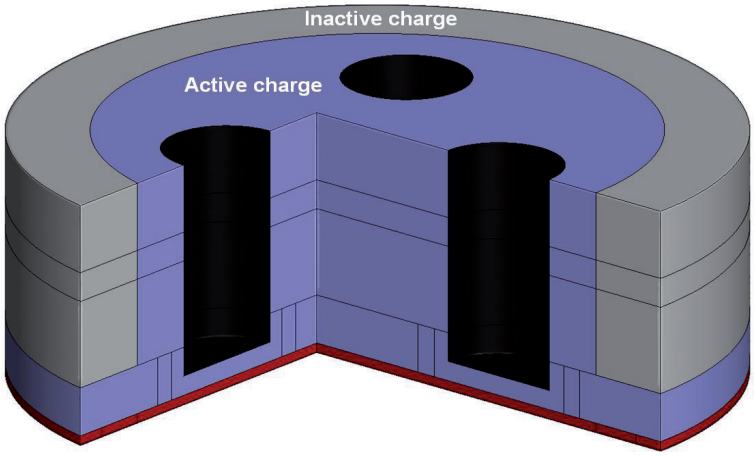

Figure 5.2: Position of different zones in a slice cut out of the developed model for a submerged arc furnace used in high silicon alloys production.

In this zone, due to high consumption rate of raw materials, there is more flow of charge particles from the charge surface into the crater zone and therefore this part of the charge has higher permeability for the flow of process gases. The rather inactive part of the charge represents a portion of the charge close to the furnace side wall which is stagnant during furnace operation. The flow of charge particles from this zone towards the furnace crater is much less than the active part. Due to the stationary situation of the charge particles in this zone, condensation of the process gases occurs mostly in the upper part of charge in this region. The furnace excavation results show that due to condensation of process gases in the charge particles located in the inactive zone, these particles stick together and make a thick layer of condensed particles. During furnace operation this layer sticks to the internal lining of the furnace on the side wall and acts like a part of lining against the probable corrosion in the furnace wall. The inactive part of charge materials has therefore low permeability for the flow of process gases towards the furnace top.

Inside the active and inactive part of the charge different zones, in the vertical direction, have been defined. Physical properties of these zones have been defined based on the described phenomena happening in these zones. Positions of these zones are shown in Figure 5.2. The porosity in different zones of the charge materials ranges between 10% up to 60% depending on the position of the packed beds.

The unknown charge porosity in some of the furnace zones have been proposed through tuning the operational parameters such as the furnace crater pressure.

Over the furnace bottom, where the melt is accumulated, three different zones have been defined. Difference in physical properties of these zones is directly related to the uneven temperature distribution in the bottom packed bed. The flow resistance is designed to increase as we move out from the furnace center and approach the taphole. High flow resistance is created partially by a high solids fraction. Hence, the volume fraction of the melt is highest in the furnace center and decreases by increasing the distance from the furnace center. The 2D view of different zones around one of the electrodes is presented in Figure 5.3.

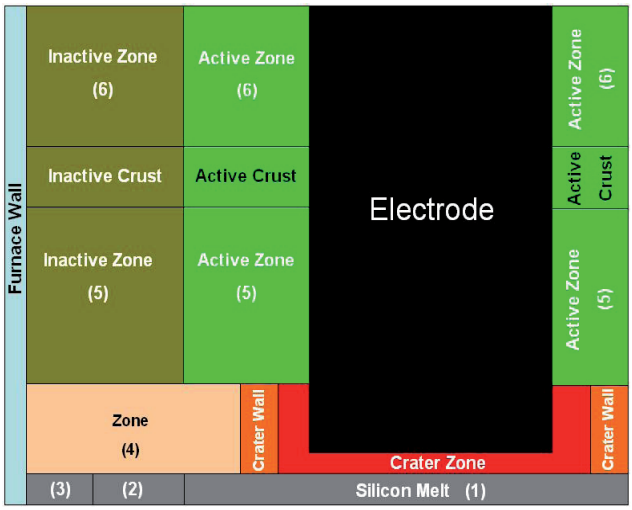

Figure 5.3: 2D view of defined zones around on of electrodes inside the furnace. It should be noted that all these zones have cylindrical form in 3D model of the furnace.

Properties of liquid and gas phases

The liquid phase in the model depending on the case study is molten silicon or ferrosilicon alloy. The gas phase is a mixture composed of SiO and CO gas with density of 0.23 kg/m^3 in the furnace operating temperature. Physical properties of silicon (Rhim and Ohsaka [2000]) and ferrosilicon (Klevan [1997]) are given in Table 5.3.

Table 5.2: Structure of the comprehensive model of tapping process in the submerged arc furnaces used for high silicon alloys production.

Insight into the Structure of the CFD Model				
Parameters	Parameter Type	Detailed Parameter	Accuracy	References / Comments
Input	Geometry	Furnace diameter	High	Industrial data
		Furnace height	High	Industrial data
		Electrodes diameter	High	Industrial data
		Taphole diameter	High	Industrial data
Input	Process information	Metal production	High	Industrial data / (Schei et al. [1998])
		Gas production	High	Industrial data / (Schei et al. [1998])
		Crater pressure	Medium	Industrial tests (Ingason [1994] and Johansen et al. [1998])
		Formation of charge zones	Low	Furnace excavations (Zherdev et al. [1960]), (Otani et al. [1968]), (Schei [1967]),(Myrhaug [2003]) and (Tranell et al. [2010])
		Melts density and viscosity	High	(Rhim and Ohsaka [2000]) and (Klevan [1997])
Tuning Parameters	Physical properties	Particles size (Outer zone)	Medium	(Schei et al. [1998]) and Johansen et al. [1991]
		Particles size (Inner zone)	Tuned	Furnace excavations (Zherdev et al. [1960]), (Otani et al. [1968]), (Schei [1967]),(Myrhaug [2003]) and (Tranell et al. [2010])
		Packed bed porosity	Tuned	Furnace excavations (Zherdev et al. [1960]), (Otani et al. [1968]), (Schei [1967]),(Myrhaug [2003]) and (Tranell et al. [2010])
Output	Results of model	Tapping speed	High	Industrial tests
		Average metal height	Predicted	
		Metal pattern	Predicted	Industrial accident for leakage of melt from the furnace which confirms high metal heights close to the furnace wall
		Gas flow in the charge	Predicted	Industrial observations and (Tranell et al. [2010])

Table 5.3: Physical properties of silicon and ferrosilicon used for modeling in the present study.

	Silicon
Density	$\rho = 2580 - 0.35(T - 1687)kg/m^3$
Viscosity	$\mu = 0.75 \times 10^{-3} - 1.22 \times 10^{-6}(T - 1687)kg/m.s$
	Ferrosilicon
Density	$\rho[1723^\circ K] = 7106 \times exp(-0.0107 \times mass\%Si)kg/m^3$
Viscosity	$\mu = 0.11 \times 10^{-4} - 5 \times 10^{-9}(T - 1687)kg/m.s$

5.3 Description of CFD model

In order to model the flow of gas and liquids out from the hearth of the furnace we need a multidimensional multiphase model that can handle the flow of gas and liquid though porous materials. In addition we need to keep track of the sharp interface between gas and liquid inside the furnace. The modeling choice was therefore to apply volume averaged Navier-Stokes equations in which the flow resistance due to the more or less transformed charge materials can be expressed by general friction laws. When it comes to the gas liquid interface it must be tracked as sharply as possible. As the needed models concepts already were available in the commercial Fluent code we used Fluent's Volume Of Fluid (VOF) model to keep track of the gas-liquid interface. In order to simplify the model we have limited the analysis to isothermal but high temperature conditions.

5.3.1 Model governing equations

As the gas-liquid interface is tracked by the VOF model we assume that gas and liquid have locally identical velocities. Hence, mass and momentum conservation is expressed using a common fluid velocity and using mixture properties. Accordingly, the conservation equations for mass and momentum in an isotropic porous medium is written in coordinate free tensor notation as:

$$\frac{\partial \varepsilon\rho}{\partial t} + \nabla \cdot (\varepsilon\rho\mathbf{u}) = 0 \tag{5.1}$$

$$\frac{\partial \varepsilon\mathbf{u}}{\partial t}+\nabla\cdot(\varepsilon\rho\mathbf{uu})-\nabla\cdot\left[\mu_{eff}\varepsilon(\nabla\mathbf{u}+(\nabla\mathbf{u})^T)\right] = -\varepsilon\nabla(p+\frac{2}{3}\rho k)+\varepsilon\rho g\beta(T-T_{ref})-\varepsilon\mathbf{R} \tag{5.2}$$

$$\rho = \sum_{\kappa} \varepsilon_{\kappa}\rho_{\kappa} / \sum_{\kappa} \varepsilon_{\kappa} \tag{5.3}$$

$$\mu = \sum_{\kappa} \varepsilon_{\kappa}\mu_{\kappa} / \sum_{\kappa} \varepsilon_{\kappa} \tag{5.4}$$

where ε is the fluid fraction and ρ is the fluid bulk density, with k representing gas and liquid respectively. The scalar equation for the propagation of the liquid fraction has similar form as Equation (5.1).

The effective and turbulent viscosities are defined as follows:

$$\mu_{eff} = \mu + \mu_t \tag{5.5}$$

$$\mu_t = \rho C_{\mu} \frac{k^2}{\epsilon} \tag{5.6}$$

The model is a generalization of Darcy's Law, commonly used for flows in porous media, and of the Reynolds-averaged Navier Stokes equations, with an eddy viscosity accounting for the turbulent effects. The last term in Equation (5.2) represents the resistance to flow in porous media. Based on the well-known Ergun's equation (Ergun [1952]), the resistance force for flow through a bed of particles is given by:

$$\mathbf{R} = \frac{150\mu}{d_p^2}\frac{(1-\varepsilon)^2}{\varepsilon^3}\mathbf{u} + \frac{1.75\rho}{d_p}\frac{(1-\varepsilon)}{\varepsilon^3}|\mathbf{u}|\mathbf{u} \tag{5.7}$$

where d_p is the equivalent spherical diameter of the packing, ρ is the density of fluid, μ is the dynamic viscosity of the fluid and ε is the void fraction of the bed (Bed porosity at any time). The defined resistance in the Ergun's equation for each component can be written as:

$$\mathbf{R}_i = -(\frac{\mu}{\alpha} \cdot \mathbf{u}_i + C_2 \frac{1}{2}\rho|\mathbf{u}|\mathbf{u}_i) \tag{5.8}$$

$$\alpha = \frac{d_p^2}{150}\frac{\varepsilon^3}{(1-\varepsilon)^2}(Permeability) \tag{5.9}$$

$$C_2 = \frac{3.5}{d_p}\frac{(1-\varepsilon)}{\varepsilon^3}(InertialResistance) \tag{5.10}$$

Turbulence model

In order to model the turbulent flow of the gas and liquid phases available in the furnace, a modified version of the $k-\epsilon$ model for fluid flow in porous beds (Nakayama and Kuwahara [1999]) is applied. In this turbulence model an extra source term

due to turbulence production due to large solid particles is added to both the kinetic energy and the dissipation rate model equations. The turbulent viscosity is then determined from these modified turbulent kinetic energy and dissipation rates. Accordingly, the model allows unified treatments for the flow of process gas and silicon melt over the entire furnace volume.

Numerical method and boundary conditions

Development of industrial size CFD models is very helpful in order to validate the results of the model and also using the model as a powerful tool for improving the process or making modification in the furnace design. But regarding the huge size of the furnace model and specially because tapping process needs a transient modeling approach, it is necessary to have enough computational resources. Therefore obtaining the results from the developed model in this work is very expensive from a computational point of view.

The furnace operates at atmospheric pressure condition. Therefore the boundary conditions at the furnace top and at the taphole outlet were defined as constant pressure boundaries at atmospheric pressure. The fluid properties are based on the furnace operating temperature, which is around 1800°C, while local temperatures in the crater zone may reach levels above 2000°C. Over the internal surface of the furnace walls we apply a no-slip condition for the velocity of both liquid and gas.

In order to simulate the generation of process gases due to chemical reactions in the crater zone, a mass source term for gas production was defined inside the crater zone. The production rate of the melt which is around 70 *ton/day* (FeSi 55) and 55 *ton/day* (FeSi 75) for the considered ferrosilicon furnace and around 90 ton/day for silicon furnace is introduced via defining a mass source in the metal zone of the model and it is fixed in all case studies. The numerical value for the mass source terms of process gas and melt was based on information from industrial operation. The three-dimensional numerical grid which has been used in this study is shown in Figure 5.4.

Figure 5.4: A slice of the computational grid used in the modeling of silicon and ferrosilicon production furnaces.

The grid is arranged in such a way that the resolution is high in regions close to the furnace taphole and the metal-gas interface where this research mainly focuses on. The total number of grid points is about 500000.

5.4 Results and Discussions

Simulations have been performed for a large number of operational conditions for different production types including silicon and ferrosilicon (both FeSi 55 and FeSi 75). This allows the investigation of how furnace crater pressure, metal height and the permeability impact the tapping flow rate, the total tapping weight and the tapping time. The results from the model are presented in different sections, according to the phenomena under examination. In addition to the model results, for sake of comparison and validation, the results of industrial measurements are also presented. Table 5.4 represents different case studies for ferrosilicon (FeSi 55) furnace.

Table 5.4: List of case studies for ferrosilicon (FeSi 55) furnace operation in different conditions including a wide range of furnace crater pressures (CP) and different metal heights (MH). For each case a separate CFD model has been developed within this research work.

MH \ **CP**	**45*mbar***	**63*mbar***	**80*mbar***	**90*mbar***	**100*mbar***	**135*mbar***	**180*mbar***
4.5 *cm*	Case 1	Case 2	Case 3	Case 4	Case5	Case 6	Case 7
6 *cm*	Case 8	Case 9	Case 10	Case 11	Case 12	Case 13	Case 14
8 *cm*	Case 15	Case 16	Case 17	Case 18	Case 19	Case 20	Case 21
9 *cm*	Case 22	Case 23	Case 24	Case 25	Case 26	Case 27	Case 28
10 *cm*	Case 29	Case 30	Case 31	Case 32	Case 33	Case 34	Case 35
12 *cm*	Case 36	Case 37	Case 38	Case 39	Case 40	Case 41	Case 42

5.4.1 Investigation of the effect of crater pressure

In the furnaces under consideration in this study the reported crater pressure ranges from 30 *mbar* up to 200 *mbar*. The measured furnace crater pressure also shows a dynamic behavior due to described interacting mechanisms. However, still it is possible to define representative average values. Furnace crater pressure in the model is set to desired value by changing the permeability of defined zones around furnace crater. Permeability change can be done both through changing porosity or particles size in each of the zones.

The result of the model for the tapping flow rate from the ferrosilicon (FeSi 55) furnace in the case where the initial metal height inside the furnace is 10 *cm* is presented in Figure 5.5. Results show that the tapping flow rate is initially quite high, depending on the crater pressure. After a while the tapping rate decreases significantly and reaches to a level which is almost the same in all cases. The results in Figure 5.5 also show that the increased crater pressure leads to increased initial tapping flow rate and decreased waiting time for the drop in tapping flow.

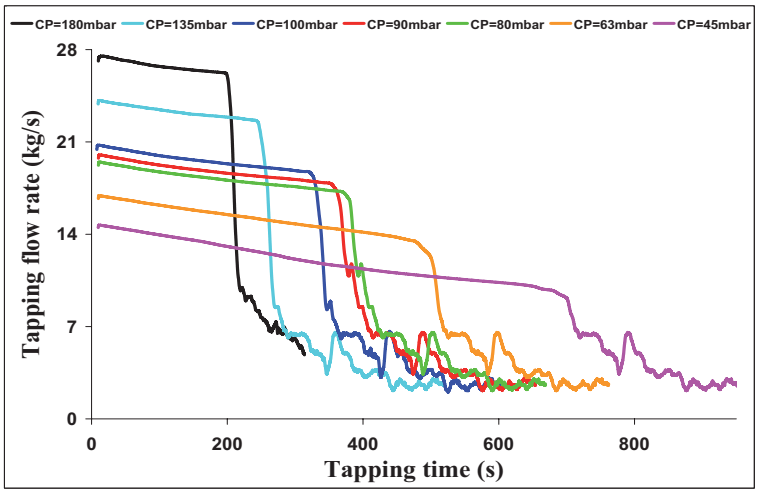

Figure 5.5: The tapping flow rate from the ferrosilicon (FeSi 55) furnace at different crater pressures inside the furnace, initial metal height is 10 *cm*.

The flow rate drop during tapping is an interesting phenomenon which is due to melt flow pattern inside the furnace, caused by the crater pressure. When the tapping flow rate drops gas starts to emerge from the taphole. After this initiation of two phase flow from the tap hole, the gas flow rate increases as the tapping process proceeds. Still the gas mass flow is very small compared to the melt flow. Figure 5.6 shows the model results for the total tapping weight with initial metal height of 10 *cm* from the ferrosilicon (FeSi 55) furnace.

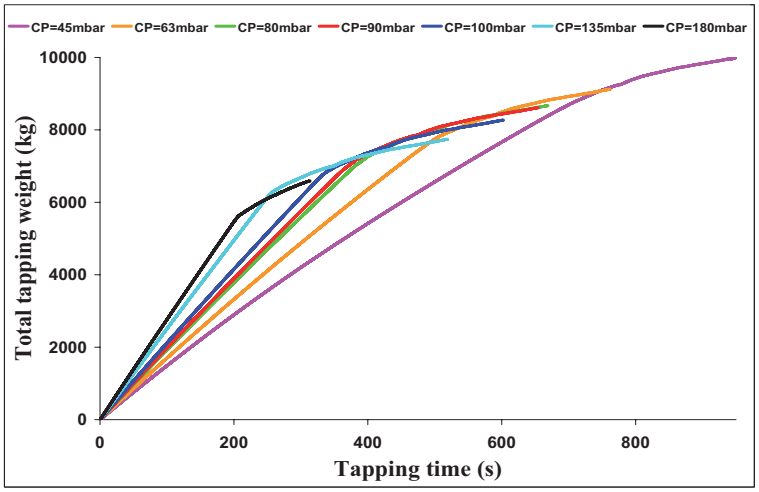

Figure 5.6: The total tapping weight from the ferrosilicon (FeSi 55) furnace at different crater pressures inside the furnace, initial metal height is 10 *cm*.

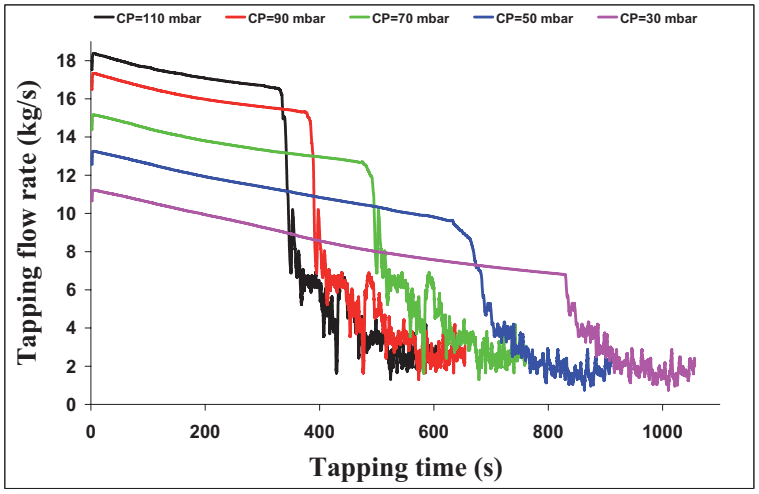

Figure 5.7: The tapping flow rate from the ferrosilicon (FeSi 75) furnace at different crater pressures inside the furnace, initial metal height is 12 *cm*.

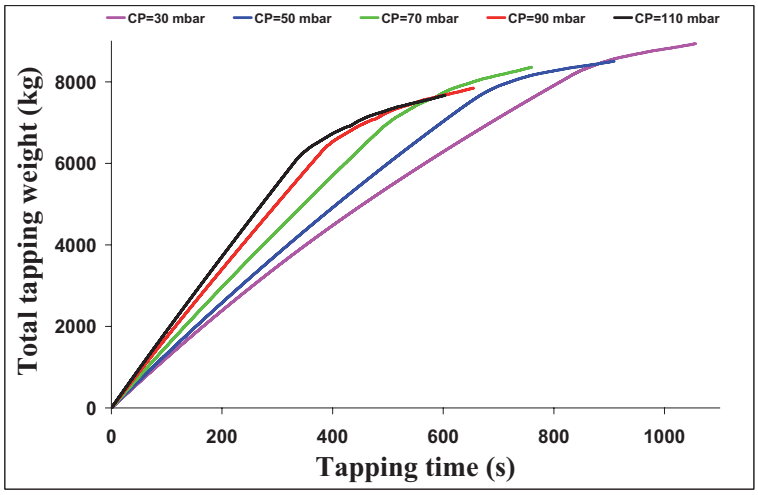

Figure 5.8: The total tapping weight from the ferrosilicon (FeSi 75) furnace at different crater pressures inside the furnace, initial metal height is 12 *cm*.

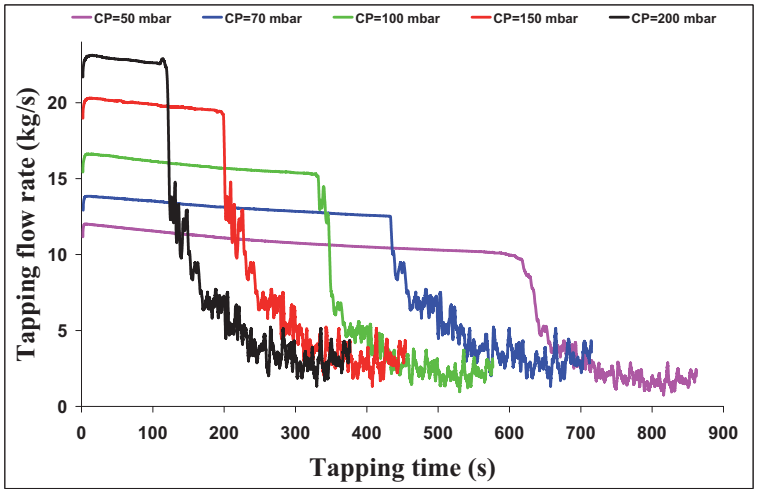

Figure 5.9: The tapping flow rate from the silicon furnace at different crater pressures inside the furnace, initial metal height is 12 *cm*.

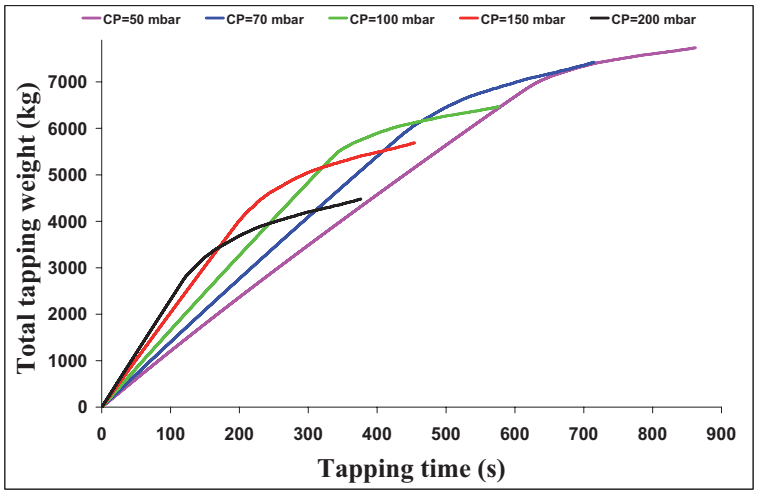

Figure 5.10: The total tapping weight from the silicon furnace at different crater pressures inside the furnace, initial metal height is 12 *cm*.

As it can be seen from Figure 5.6 high crater pressure results in less metal tapped, even if the metal flow rate is higher and tapping time shorter. The consequence of this is that for an operation of the furnace at higher crater pressures the time intervals between taps will have to be reduced in order to keep a constant maximum metal height. Figures 5.7 and 5.8 show similar results obtained from simulations of the same furnace used in production of FeSi 75.

Figures 5.9 and 5.10 show the effect of furnace crater pressure on the tapping flow rate and total tapping weight from the silicon furnace. As it is seen both in silicon and ferrosilicon furnaces the flow rate drop during tapping is a common phenomenon.

Investigation of the effect of melt hydrostatic pressure

In order to show that the increased flow rate at the start of tapping and significant flow rate drop are due to existence of the high pressure crater zone a simple study was done. In this case the initial metal height inside the ferrosilicon (FeSi 55) furnace was considered to be 12 *cm* but there was no additional pressure due to process gases released from the crater zone. In fact, the only parameter, driving the flow, was the metal height. The result of this simulation is shown in Figure 5.11.

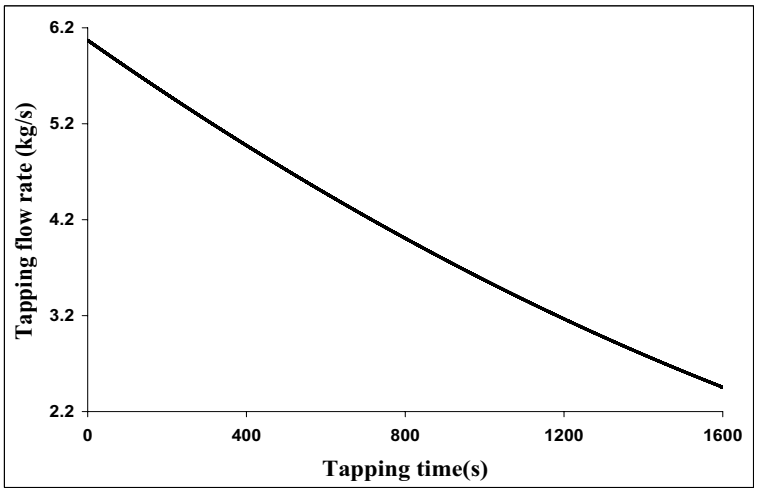

Figure 5.11: Tapping flow rate from the ferrosilicon (FeSi 55) furnace only due to hydrostatic pressure created by the metal height, initial metal height is 12 *cm*.

This result contains two important points. The first point is that the tapping flow rate is very low, even with higher initial metal height than the cases shown in Figure 5.5. In fact, to have such high tapping flow rates without the crater pressure the initial metal height must be up to 60 *cm*. Such high metal height is neither acceptable nor possible from the industrial point of view. The second point is that when only the hydrostatic pressure due to the metal height drives the flow, the flow rate drop observed in the industrial measurements can not be explained. These two points substantiate that the crater pressure due to limited flow permeability is the cause of a significant change in tapping rate, appearing after a certain mass of metal is tapped.

5.4.2 Explanation of tapping flow rate drop

The effect of furnace crater pressure on deformation of gas-metal interface

Existence of the high pressure crater zone inside the furnace plays an important role in explaining the significant decrease in the melt flow rate during tapping. Figure 5.12 shows the 2D contours of pressure in a vertical plane of the furnace including two electrodes. The region where the pressure is high represents the furnace crater zone which is filled with the process gases. As it can be seen from Figure 5.12 the

pressure is very high in the central part of the furnace where the crater zones are and by increasing the distance from the furnace center towards the wall the pressure decreases significantly.

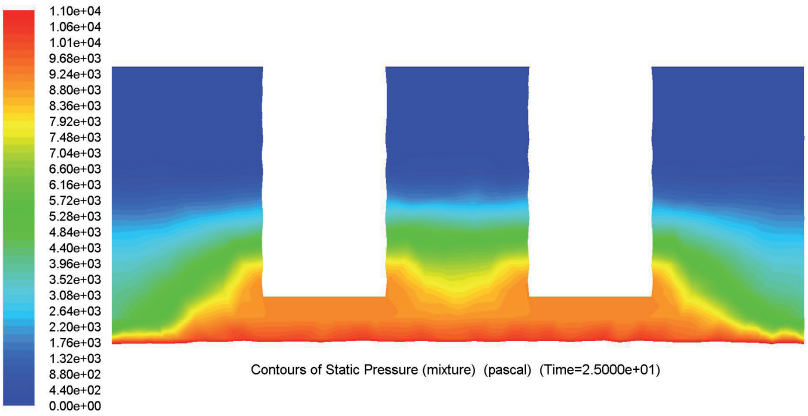

Figure 5.12: 2D contours of pressure in a vertical plane including two electrodes inside the silicon producing furnace.

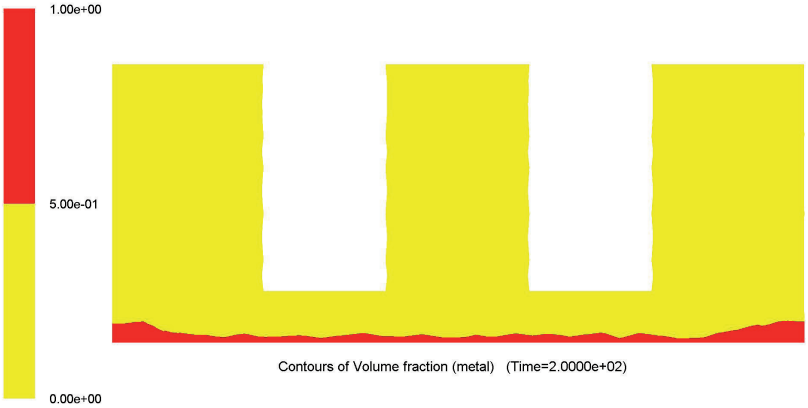

Figure 5.13: 2D contours of metal volume fraction in a vertical plane including two electrodes inside the silicon producing furnace.

Existence of such pressure pattern inside the furnace affects the melt flow pattern over the furnace bottom. Figure 5.13 shows how the melt flow pattern is influenced

by the crater pressure. As it can be seen the high pressure gas pushes the melt towards the furnace walls and creates a big hole in the melt pool. As the result of such phenomenon the metal height in the regions around the furnace and near the furnace wall, which of course contains the taphole zone, is locally increased.

2D studies

In order to see whether deformation of the liquid-gas interface is observed in the other systems containing two fluids with existence of a high pressure zone, some 2D case studies for different systems were investigated. A 2D slice of a rectangular vessel containing gas and liquid phases was considered for modeling. Inside the vessel different porous zones are defined. The detailed geometry of the vessel is shown in Figure 5.14.

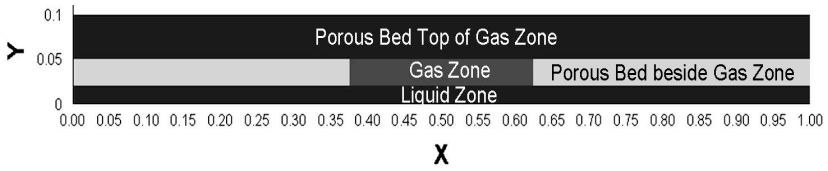

Figure 5.14: Geometry of the vessel together with different zones in the system which is used in the 2D studies.

Different gases and liquid phases were studied. The initial level of the liquid phase in the all cases was fixed at 2 *cm*. In all the case studies there is a mass source term for the gas phase, placed inside the low permeability region over the liquid phase. In each case the set up was arranged in the way to create the high and low pressure situations in the system. The details about the geometry of the vessel and different fluids used in each case are given in Table 5.5.

Table 5.5: Detailed geometry and physical properties of different zones in the 2D model of vessel.

Properties	Gas zone	Liquid zone	Top of gas zone	Beside gas zone
Porosity	1.0	0.5	0.1	0.1
Particles size (*m*)		0.04	0.01	0.01
Width (*m*)	0.25	1	1	0.375
Height (*m*)	0.03	0.02	0.05	0.03

For the case presented in this paper, the melt and the gas densities were considered 4300 kg/m^3 and 0.23 kg/m^3 respectively. The pressure patterns and the resulted fluid flow patterns inside the 2D vessel are presented in Figures 5.15and 5.16.

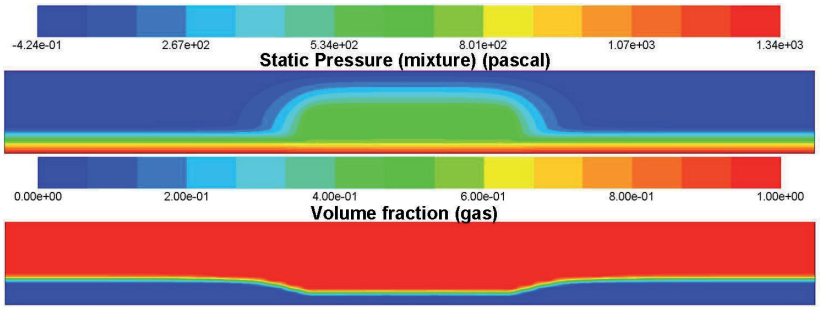

Figure 5.15: Pressure patterns and the resulted deformation of gas - melt interface in the vessel for the case of low gas pressure.

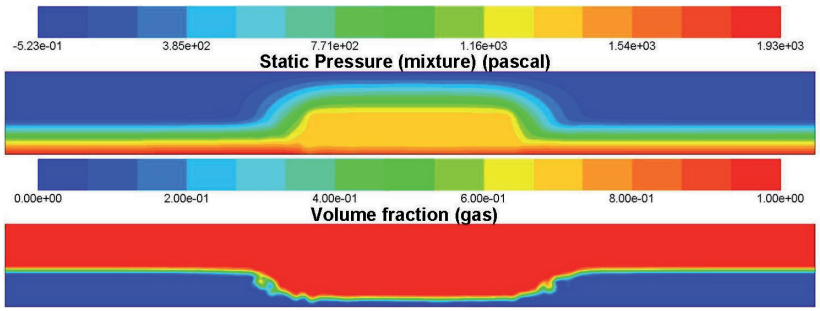

Figure 5.16: Pressure patterns and the resulted deformation of gas - melt interface in the vessel for the case of high gas pressure.

It is observed that existence of the high pressure zone in the vessel causes the deformed gas-liquid interphase, the higher the gas pressure the more the deformed interphase. The results from these 2D studies prove that the pressure driven deformation of process gases-silicon melt interface inside the furnace is highly possible.

Explaining the interface deformation and its effect on tapping flow rate

Based on the simple principles of physics it is very easy to explain why the metal flow pattern appears like what is observed in the furnace. According to the physics

rules the hydrostatic pressure inside the liquid comes from the environment pressure and the liquid's height as follows:

$$P_{total} = P_0 + \rho g h \tag{5.11}$$

Where P_0 is the environmental pressure. Inside the furnace this pressure is equal to furnace crater pressure, $P_0 = CP$, with the pattern presented in Figure 5.12. Now consider two points both at the furnace bottom but one under the electrodes where the high crater pressure exists and the other one away from the furnace center and close to the wall where the gas pressure is low. According to the rules of physics the points which have the same depth in the liquid, experience the same total pressure. Therefore both the considered points have the same total pressure but for the first point because of higher environmental pressure (P_0) the metal height (h) is less compared to the second points where the environmental pressure is lower. This phenomenon is graphically shown in Figure 5.17 which is an enlarged part of the metal volume fraction over the furnace bottom.

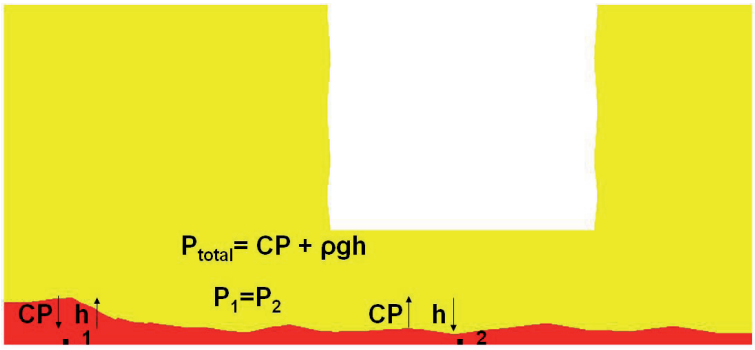

Figure 5.17: Graphical explanation for the existing volume fraction of metal over the furnace bottom in silicon and ferrosilicon furnaces.

The local metal height increase together with the pressure behind the melt which presses the melt towards the furnace taphole leads to increased tapping flow rate at the start of tapping. As the tapping process proceeds more melt from the furnace center is pushed towards the furnace sidewall and hence in the central part of the furnace the metal height decreases to very low levels. At the same time the metal height in the zones close to the furnace sidewall also decreases. Decreasing rate of metal height near the taphole is higher than the other zones around the furnace and when the metal height in this zone decreases lower than the taphole level, suddenly

the high pressure gases in the crater zone also flow out of the furnace through the taphole. Therefore the tapping flow rate decreases significantly. In this situation still there is some melt inside the furnace but the melt should move in a circular path around the furnace to reach the taphole.

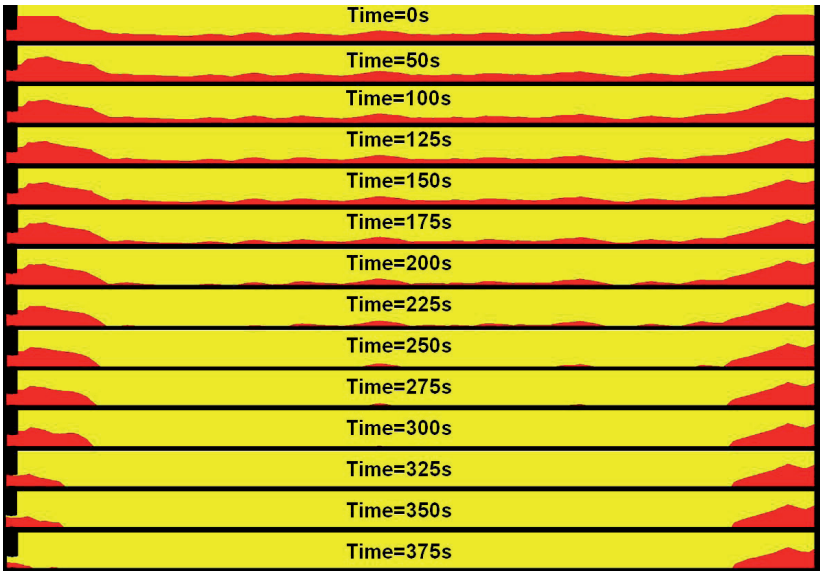

Figure 5.18: Evolution of the metal pattern in the lower part of the central plane of the ferrosilicon furnace which explains the reason for the sudden flow rate drop during furnace tapping.

Evolution of the metal flow pattern in the central plane of the furnace is shown in Figure 5.18. The metal height in the region close to the taphole decreases very fast comparing to the other regions. This figure shows clearly why the tapping flow rate drops suddenly during tapping.

Figure 5.19 shows the predicted melt flow pattern at the furnace bottom by the CFD model when the tapping flow rate drops and process gases are released from the taphole. As it is seen still there is untapped metal in the furnace but due to release of gas from the furnace taphole the metal is drained with decreased flow rate.

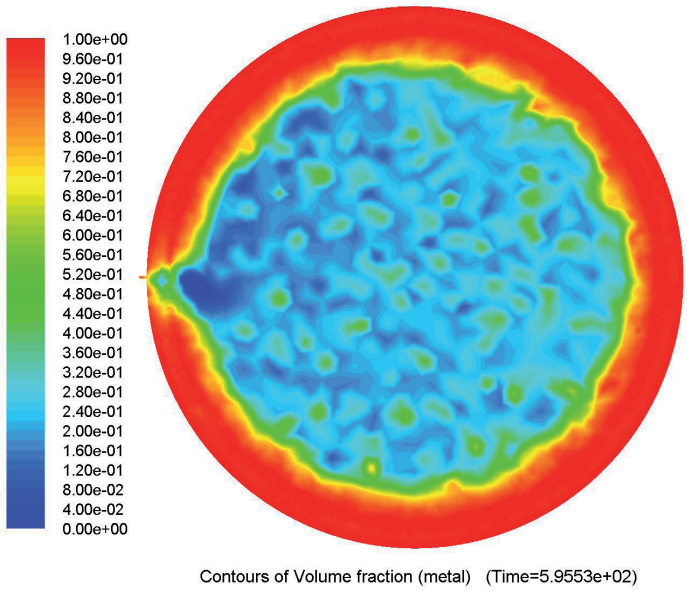

Figure 5.19: Melt flow pattern over the furnace bottom at the time when the tapping flow rate drops, the melt should now move in a circular path around the furnace to reach the taphole.

5.4.3 Industrial tests

In order to check the validity of the results provided by the CFD model different industrial tests have been done. The industrial tests were performed both on silicon and ferrosilicon, different alloys, production furnaces in different plants. The main goal of these tests was to measure tapping flow rate continuously with time. What can be measured from such tests is the total tapping weight which increases continuously. Then based on the obtained data from the test it is possible to calculate tapping flow rate.

Measuring equipments

Tapping weight can be continuously measured using weighing cells. Ladle is usually put over a rectangular panel made of steel where the weighing cells have been installed on. In industrial applications normally three or four weighing cells are installed on the panel. Different configurations of installation of the weighing cells

on a panel are shown in Figure 5.20.

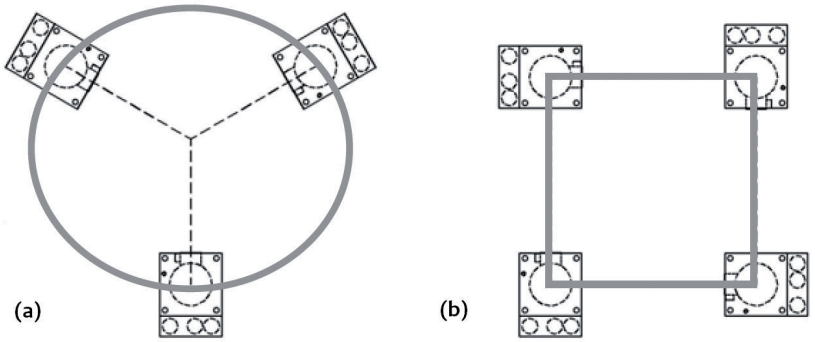

Figure 5.20: Different configuration for installing weighing cells on the panel. Circular system with 3 supporting points (a) and square system with 4 supporting points (b).

The measurements were done on a ferrosilicon producing furnace at Elkem Bjølvefossen plant located in Ålvik region in Norway. The type of weighing cells installed in this plant is UPC2S. This weighing unit, completely executed in stainless steel (AISI 304), has been designed to ease the installation of weighing and dosing systems, in tanks, bins and in static or vibrating hoppers. A CBS or C2S load cell can be paired to UPC2 to obtain an accuracy class of 1000, 2000 or 3000 divisions and an IP68 protection class. The weighing unit is equipped with load self alignment and transverse shift compensation to ensure high metrological performances even in case of adjustments, thermal expansion, positioning errors, transverse thrusts and deformation of structures. The structure of UPC2S weighing cell is presented in Figure 5.21.

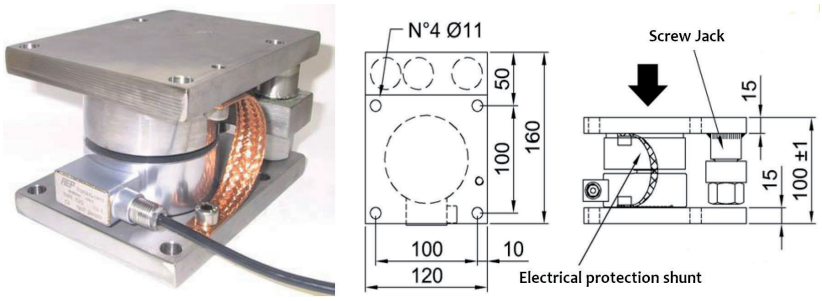

Figure 5.21: Structure and detailed dimensions (mm) of the UPC2S weighing cell used in industrial measurements.

The ladle panel in the plant is equipped with four weighing cells of the described type. The cells are installed on the panel in the way to form corners of a trapezoidal. Schematic of the weighing panel installed at Elkem Bjølvefossen plant is given in Figure 5.22. The panel is located under the ladle during tapping measurements.

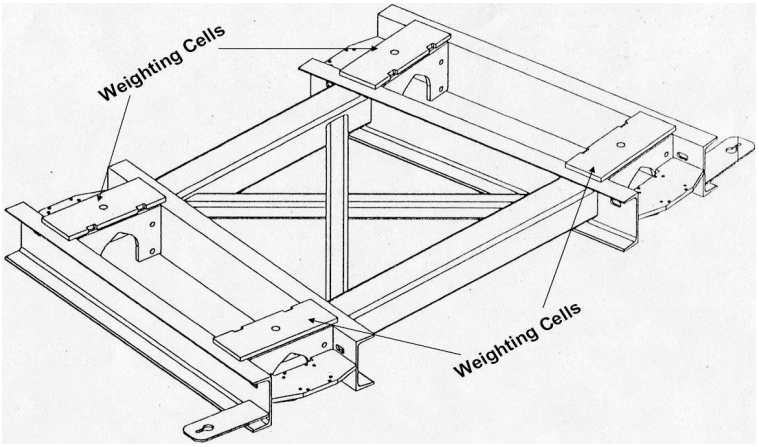

Figure 5.22: Schematic of weighing panel which includes four cells used in tapping measurements.

Continuous tapping measurements in the ferrosilicon furnace

Several industrial tests were done at the plant on the ferrosilicon (FeSi 55) furnace. As an example of the industrial measurements the tapping flow rate from the ferrosilicon (FeSi 55) furnace has been presented in Figure 5.23.

The industrial tests at Elkem Bjølvefossen plant were performed at different dates. Figure 5.24 shows the results of continuous measurement of total tapping weight from the ferrosilicon (FeSi 55) furnace in June 2009.

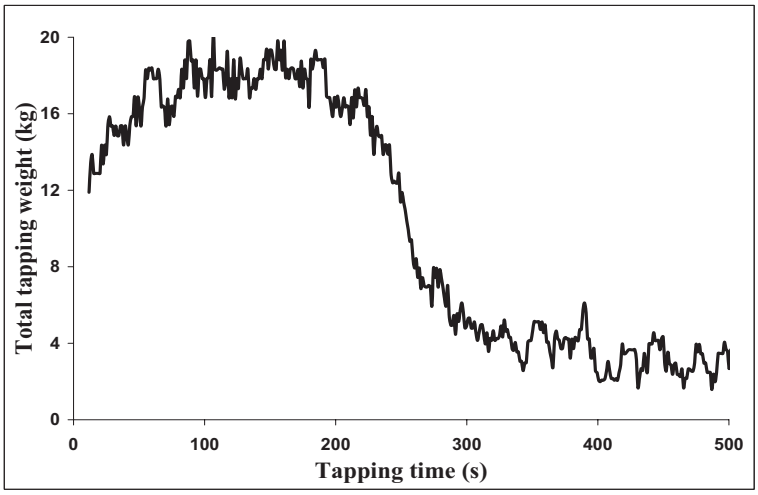

Figure 5.23: Results of the industrial measurements for the tapping flow rate from the ferrosilicon (FeSi 55) producing furnace at Elkem Bjølvefossen plant.

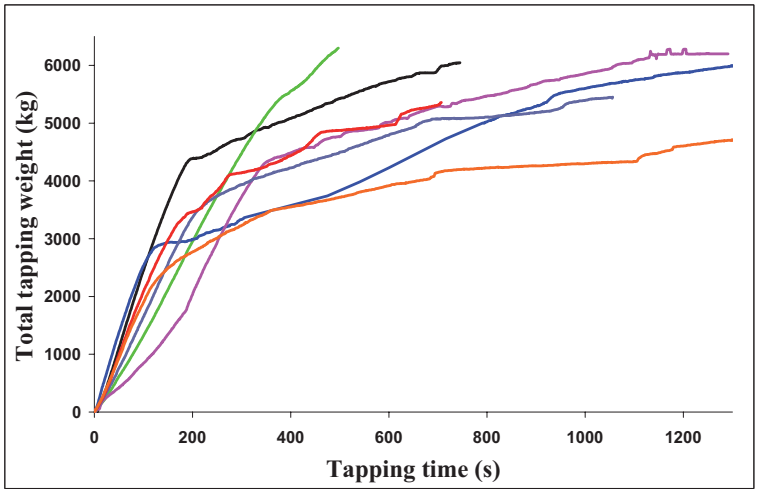

Figure 5.24: Results of continuous measurement of the total tapping weight from the ferrosilicon (FeSi 55) producing furnace at Elkem Bjølvefossen plant, date: 5-6 June 2009.

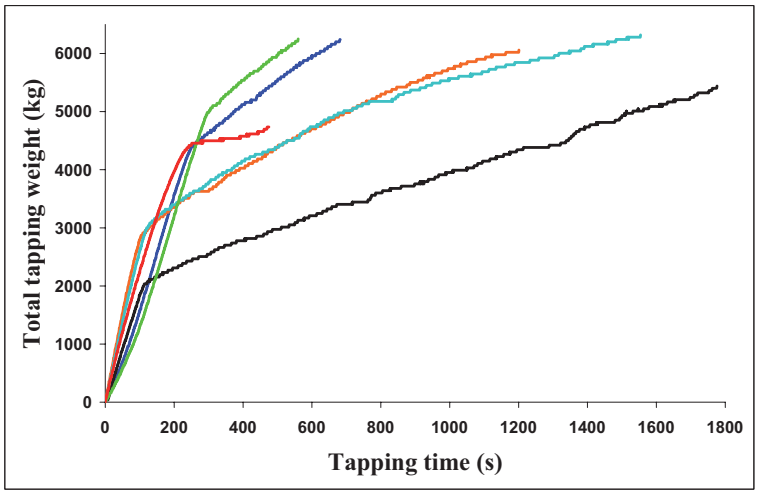

Figure 5.25: Results of continuous measurement of the total tapping weight from the ferrosilicon (FeSi 55) producing furnace at Elkem Bjølvefossen plant, date: 11 May 2010.

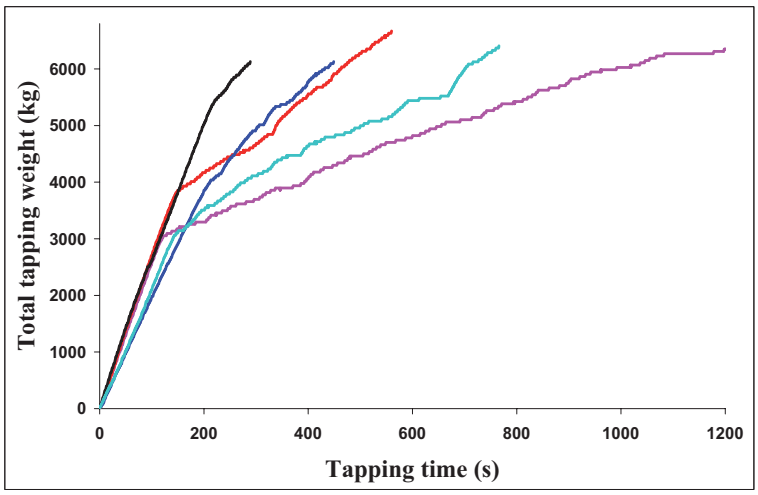

Figure 5.26: Results of continuous measurement of the total tapping weight from the ferrosilicon (FeSi 55) producing furnace at Elkem Bjølvefossen plant, date: 20 May 2010.

The results from the industrial tests on the same ferrosilicon furnace in May 2010 have been presented in Figures 5.25 and 5.26.

Continuous tapping measurements in the silicon furnace

Continuous tapping weight measurement was repeated in a silicon producing furnace as well. The tests were performed in one of the silicon furnaces at Elkem Salten plant. The weighing cells applied for the recent test were C2 Load Cell from HBM Company. These cells are made of stainless steel and have a weighing capacity of up to 50 *ton* (see Figure 5.27).

In this measurement weighing panel was equipped with two cells of the mentioned type. One of the cells installed on the weighing panel is shown in Figure 5.28. The results extracted from the weighing cells were compared with the final weight of tapped melt measured at the plant and a very good agreement was observed. In fact each weighing cell in this test reported half of the total weight. The result for total weight of silicon melt tapped from the furnace is shown in Figure 5.29.

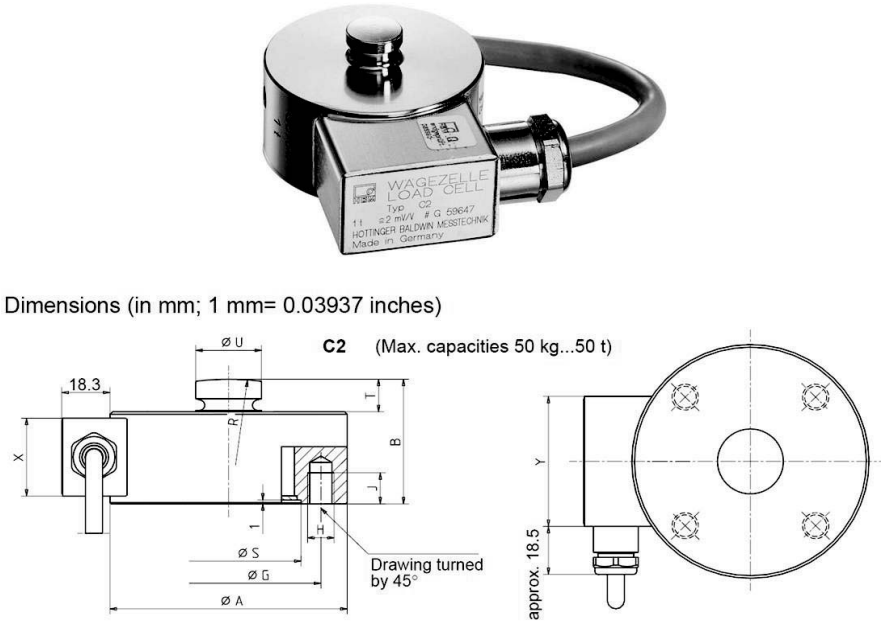

Figure 5.27: Structure and detailed dimensions (mm) of the C2 (HBM) weighing cell used in industrial measurements.

Figure 5.28: One of the load cells installed on the weighing panel before the tests at Elkem Salten plant, April 2010.

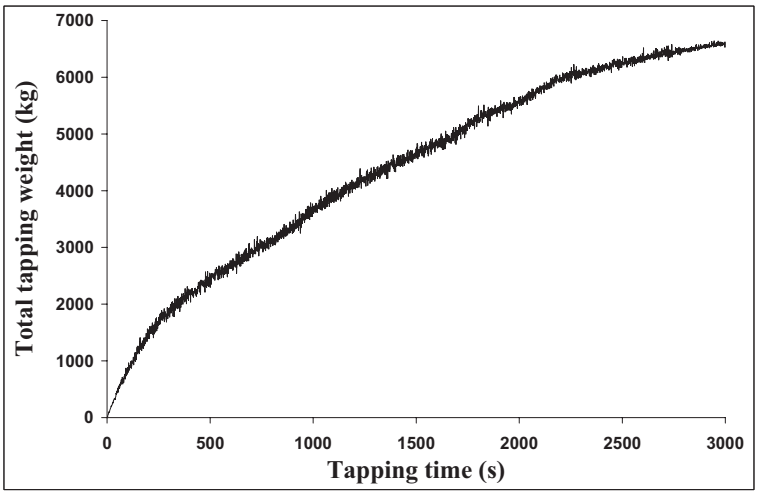

Figure 5.29: Results of the industrial measurements for total tapping weight from the silicon producing furnace (Grådahl [2010]).

It can be seen from this figure that the rate of tapping weight increase is high at the start of tapping and it decreases as the tapping process proceeds. It means that the tapping flow rate is high at the start and then it drops down into a lower amount.

Comparison of the results obtained from CFD model and the industrial tests

Comparison between the result provided the CFD model for tapping of silicon and the obtained result from industrial test at Elkem Salten plant has been presented in Figure 5.30. It should be mentioned that today the tapping process in most of the silicon furnaces is done in a continuous way. Since our focus in this research has been on the discontinuous tapping, the silicon furnace used for our industrial experiments was tapped discontinuously in the period of running the tests. The only reason for prediction of low initial metal height in the furnace

As it is seen from Figure 5.30 that the model result has been reported only until the middle of industrial tapping time. The reason, based on what we have experienced from modeling of ferrosilicon furnaces, is that the tapping flow rate remains almost constant after it drops and the tapping weight increases with a constant rate afterwards. Therefore there is no need to set the modeling time equal to the time needed for completion of industrial tapping.

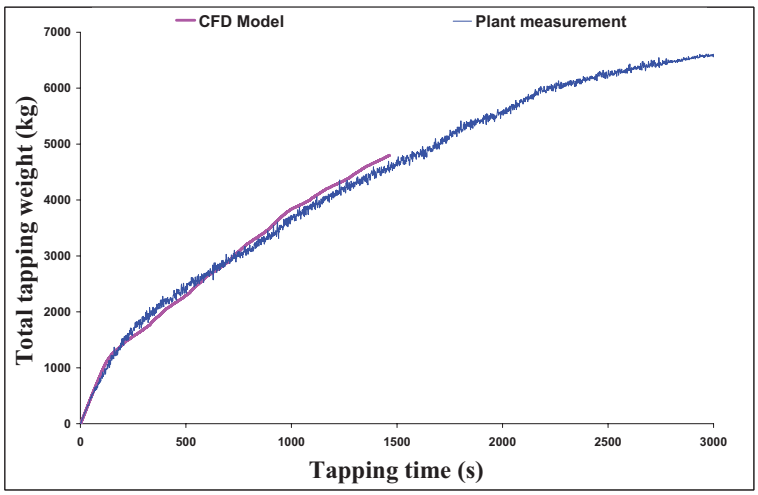

Figure 5.30: Comparison between industrial measurements and results of the model for total tapping weight from the silicon producing furnace, the initial metal height is 5.5 *cm* and the crater pressure is 70 *mbar*.

One example of the comparison between the results of CFD model and industrial tests for the ferrosilicon (FeSi 55) producing furnace is shown in Figure 5.31.

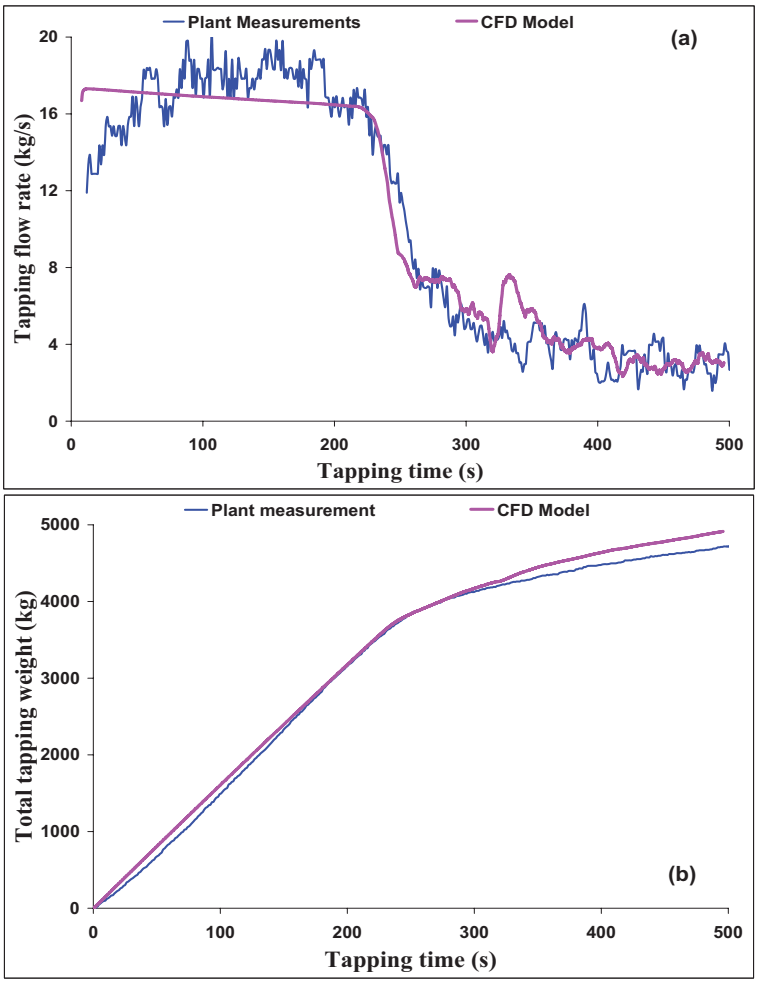

Figure 5.31: Comparison between industrial measurements and results of the model for tapping flow rate (a) and total tapping weight (b) from a ferrosilicon (FeSi 55) producing furnace, the initial metal height is 8 *cm* and the crater pressure is 80 *mbar*.

Figures 5.30 and 5.31 represent a very good agreement between the results of the model and the industrial measurements. In fact the CFD model has been able to simulate the behavior of the tapping for the main tapping parameters.

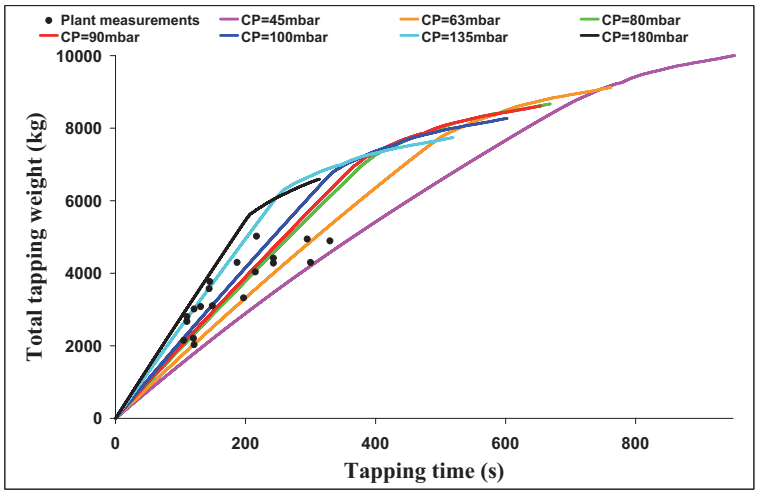

Figure 5.32: Comparison between the results of the model and industrial measurements for the total tapping weight in the ferrosilicon (FeSi 55) furnace, the initial metal height in the model is 10 *cm*.

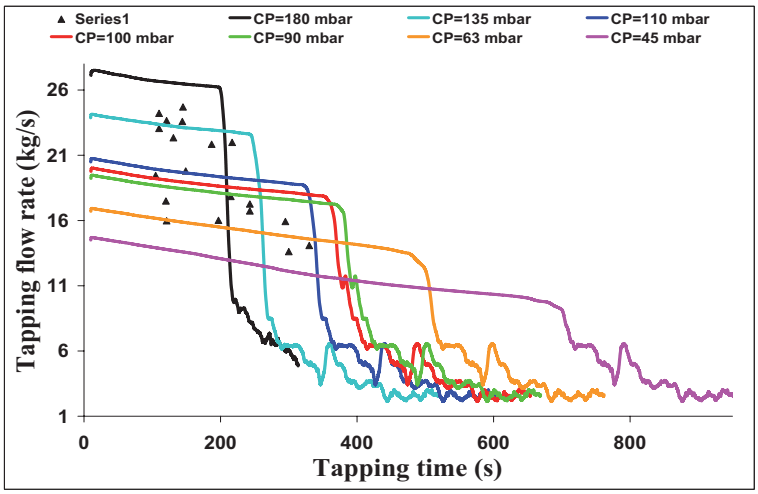

Figure 5.33: Comparison between the results of the model and industrial measurements for the tapping flow rate in the ferrosilicon (FeSi 55) furnace, the initial metal height in the model is 10 *cm*.

Figures 5.32 and 5.33 show comparison of the model results for tapping flow rate and total tapping weight with an initial metal height of 10 *cm* versus industrial measurements from the ferrosilicon (FeSi 55) furnace. The points in the graphs show the results of industrial measurements before the tapping flow rate drops. The industrial measurements have been done at different dates, even with few months difference, while the model has covered this range.

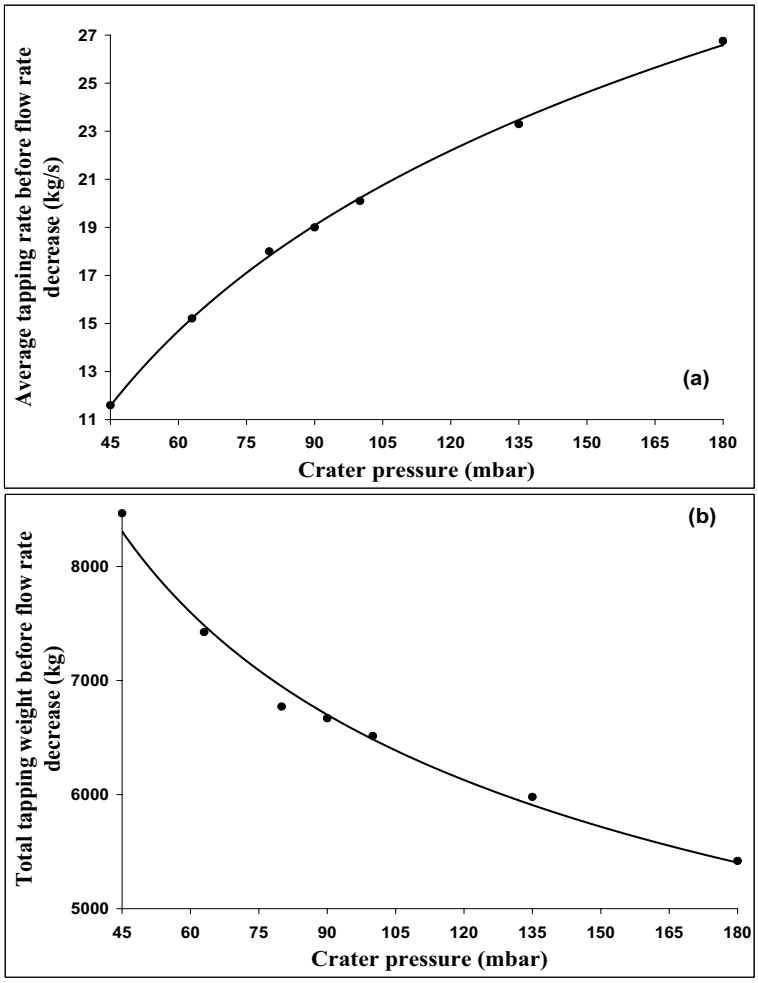

Figure 5.34: The effect of crater pressure on the average tapping flow rate (a) and the total tapping weight (b) when the metal height in the ferrosilicon (FeSi 55) furnace is 10 *cm*.

Figure 5.34 shows the effect of crater pressure on the average tapping rate and the total tapping weight from furnace before the flow rate decrease for the case when the metal heights in the furnace is 10 *cm*.

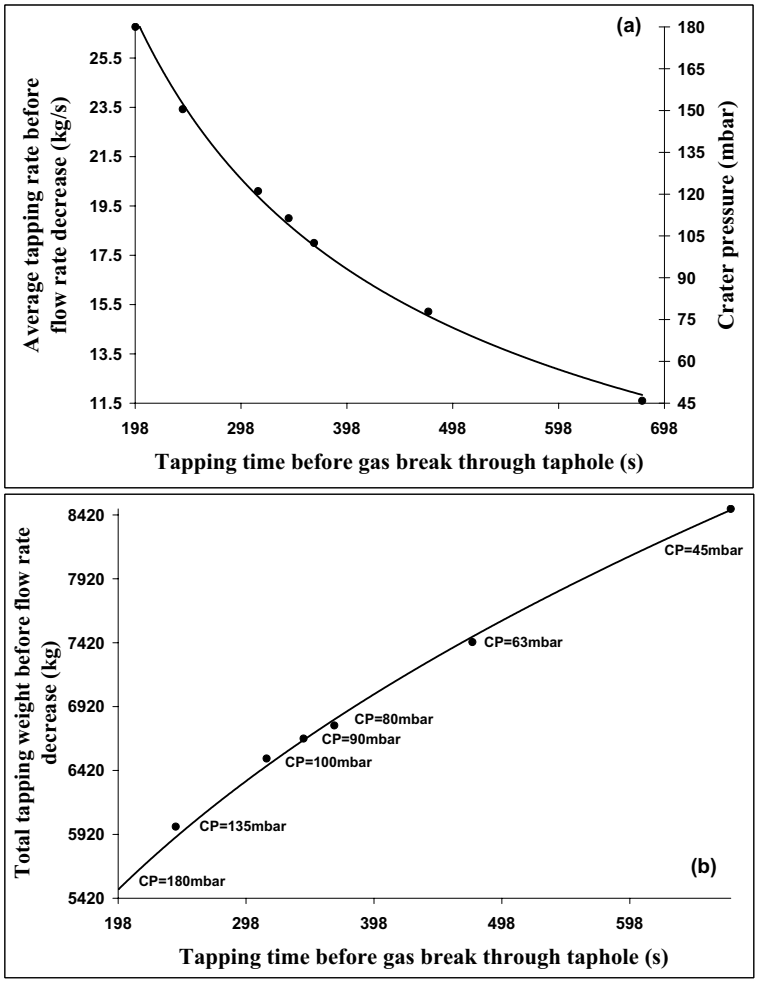

Figure 5.35: The effect of crater pressure on the average tapping rate (a) and the total tapping weight (b) as a function of time when the metal height in the ferrosilicon (FeSi 55) furnace is 10 *cm*.

The results presented in Figure 5.34(a) shows that the average tapping flow rate from the furnace increases when the crater pressure is higher. The total tapping

weight is also influenced by the crater pressure. Figure 5.34(b) shows how the crater pressure can affect the total weight of the melt tapped from the furnace. It is observed that when the crater pressure is higher the total amount of the melt before the flow rate drops is less than the situation where the furnace crater pressure is lower.

Figure 5.35(a) shows that the average flow rate increases with increase of crater pressure but the flow rate drops in the shorter time. The total tapping weight is also dependent on the tapping time. Figure 5.35(b) shows that by increase of the furnace crater pressure the total tapping weight before the flow rate drops, decreases. That is because the higher the crater pressures the faster the tapping flow rate drop.

5.4.4 Investigation of the effect of metal height

In order to investigate the effect of metal height on the tapping parameters, different metal heights have been studied. The range considered for the metal height starts from very low level around 4.5 *cm* up to 12 *cm*, the latter being higher than the taphole level. The effect of metal height on the tapping flow rate from the FeSi 55 furnace is for a crater pressure of 90 *mbar* presented in Figure 5.36.

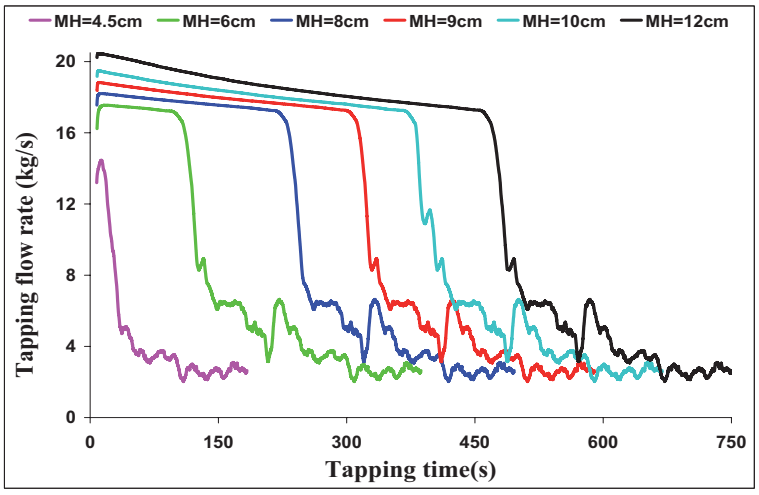

Figure 5.36: The effect of metal height on the tapping flow rate from the ferrosilicon (FeSi 55) furnace, Crater pressure is 90 *mbar*.

It is observed from Figure 5.36 that the increased metal height leads to increased

tapping flow rate. In addition we see an increase in the tapping time before the flow rate drops. It is obvious that the effect of metal height on the tapping flow rate is not as significant as the effect of furnace crater pressure is.

The most important result from the investigation of the metal height effect is that in all different range of metal heights, the tapping rates before the metal flow rate drops are virtually the same. It means that the metal height is not the factor which determines at which tapping rate the metal flow rate will drop. In other words, it is the furnace crater pressure which determines at which tapping rate the metal flow rate drops. The effect of metal height is to determine when the tapping flow rate drops. It is obvious that high metal height and corresponding large metal mass will lead to larger tapping time.

Figure 5.37 shows the same results as Figure 5.36, but now as the total tapped weight. It is seen how the total tapping weight from the furnace increases with increased metal height.

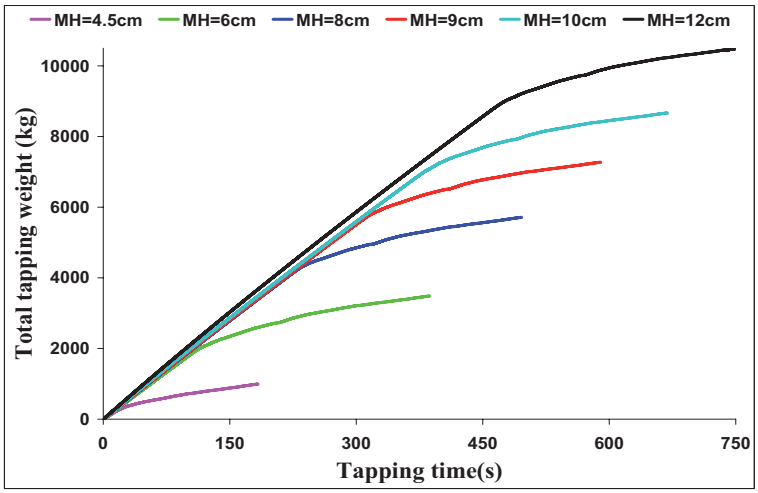

Figure 5.37: The effect of metal height on the total tapping weight from the ferrosilicon (FeSi 55) furnace, Crater pressure is 90 *mbar*.

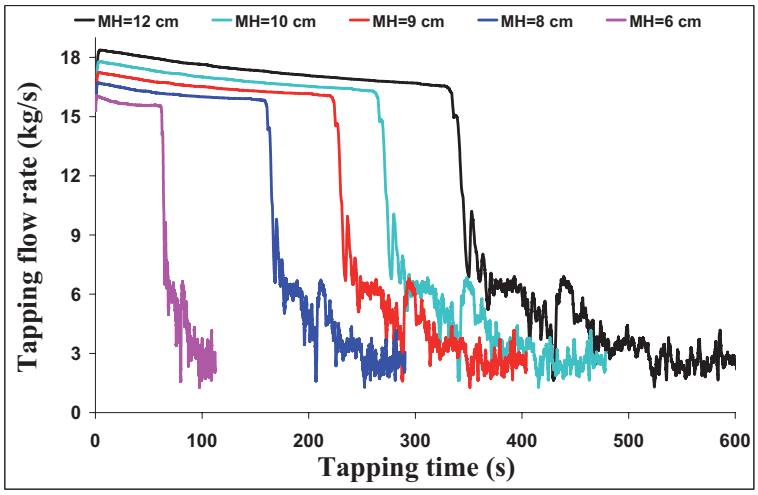

Figure 5.38: The effect of metal height on the tapping flow rate from the ferrosilicon (FeSi 75) furnace, Crater pressure is 110 *mbar*.

The effect of metal height on tapping flow rate and total tapping weight from the ferrosilicon furnace used in production of FeSi 75 is shown in Figures 5.38 and 5.39.

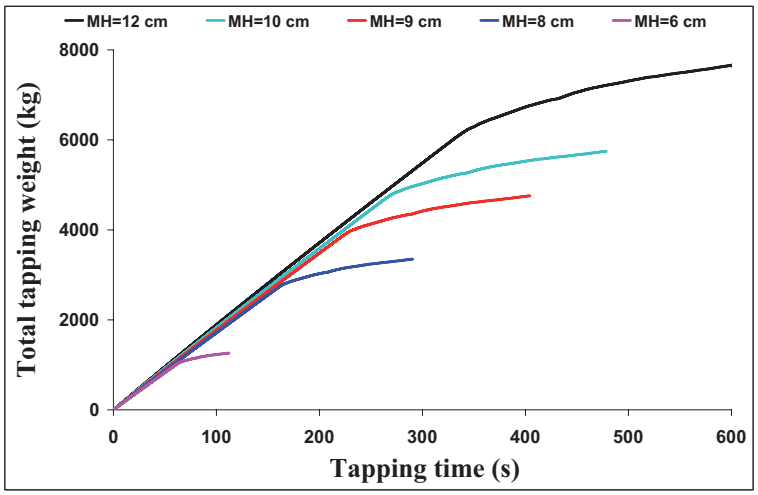

Figure 5.39: The effect of metal height on the total tapping weight from the ferrosilicon (FeSi 75) furnace, Crater pressure is 110 *mbar*.

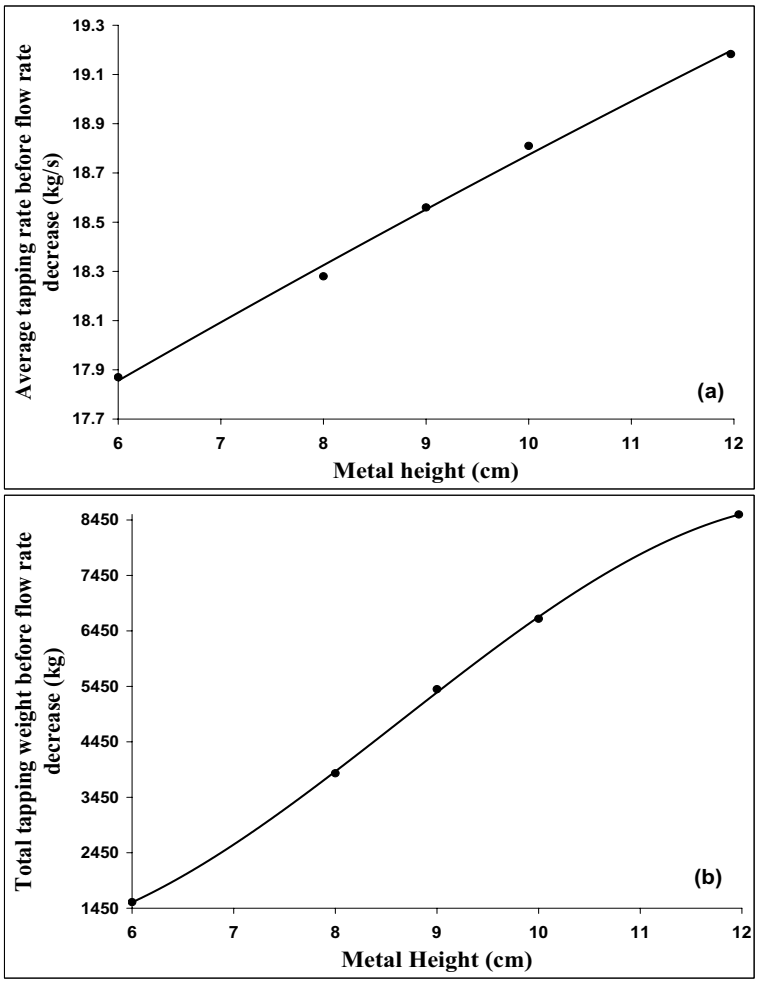

Figure 5.40: The effect of metal height on the average tapping rate (a) and the total tapping weight (b) from the ferrosilicon (FeSi 55) furnace in the case where the crater pressure is 90 *mbar*.

The effect of metal height on the average tapping flow rate and the total tapping weight for the case which the crater pressure is 90 *mbar* is shown Figure 5.40. It can be observed from Figure 5.40(a) that the metal height increase can slightly increase the tapping flow rate from the furnace. Figure 5.40(b) shows how the increased metal height affects the total tapping weight from the furnace before flow

rate decreases. As it can be seen the effect of metal height on the total tapping weight is positive and it leads to higher weight for the total melt tapped from the furnace.

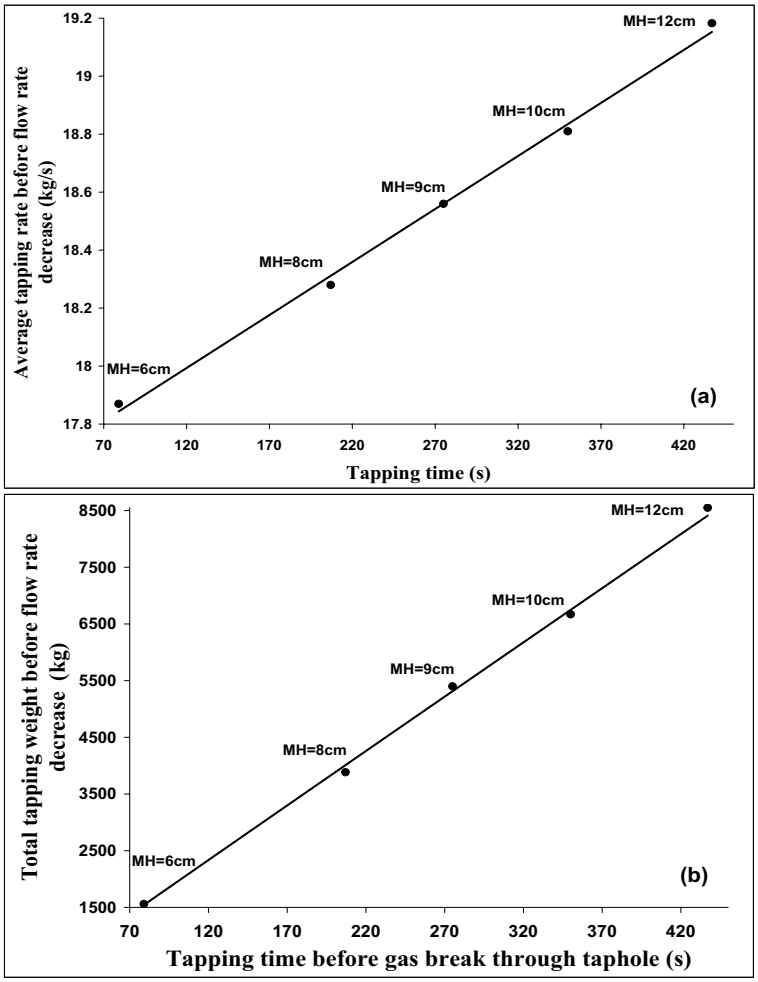

Figure 5.41: The effect of metal height on the average tapping rate (a) and the total tapping weight (b) from the ferrosilicon (FeSi 55) furnace as a function of time in the case where the crater pressure is 90 *mbar*.

The increase in the level of metal height causes higher tapping flow rate in one hand and of course longer tapping time in the other hand. This phenomenon is

shown in Figure 5.41(a). Figure 5.41(b) shows that increased metal height leads to higher weight for the melt which is tapped from the furnace. The higher total tapping weight comes together with longer tapping time.

5.4.5 Investigation of the combined effect of crater pressure and metal height

Industrial measurements prove that the furnace crater pressure has a dynamic behavior during the smelting process. In the industrial operation the metal production rate is not constant and different phenomena can change the production rate and hence the metal height in the furnace varies by time. Therefore investigation of the most important parameters over a larger span of values is necessary. In this research we have investigated the furnace crater pressure range from 45 *mbar* to 180 *mbar* and for the metal height range from 4.5 *cm* to 12 *cm*. The tapping time is also a key parameter in modeling the tapping process and therefore we explore how tapping time is affected by crater pressure and metal height.

Figure 5.42 shows the effect of furnace crater pressure on the average tapping flow rate and the total tapping weight for different metal heights inside the furnace. It is observed that furnace crater pressure has a positive effect on the tapping flow rate for different metal heights but the total tapping weight from the furnace is lower in the cases with higher crater pressure. Note that the tapping time has been defined as the time until the tapping flow rate suddenly drops. The reason for this definitions is that after gas break through in the taphole the tapping rate drops down to very low level which is almost the same in all cases, and has a low metal flow rate that is in good agreement with the industrial measurements.

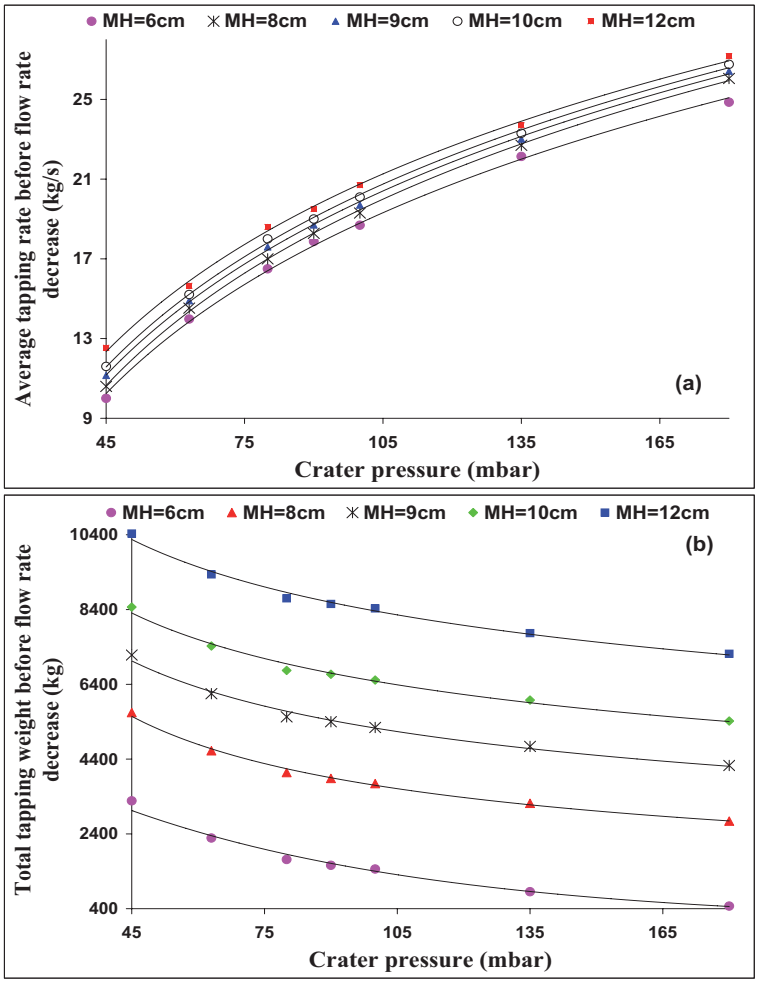

Figure 5.42: The effect of crater pressure on the average tapping rate (a) and the total tapping weight (b) for different metal heights inside the ferrosilicon (FeSi 55) furnace.

The simulation results can alternatively be presented as the average tapping flow rate or the total tapping weight, both versus metal height (see Figure 5.43).

As it is seen from Figure 5.43 (a) increase in the metal height leads to increased tapping flow rate for all crater pressures. Furthermore, and as expected, the total mass of tapped metal increases as the metal height and hence metal volume in the furnace is increased, as observed from Figure 5.43 (b).

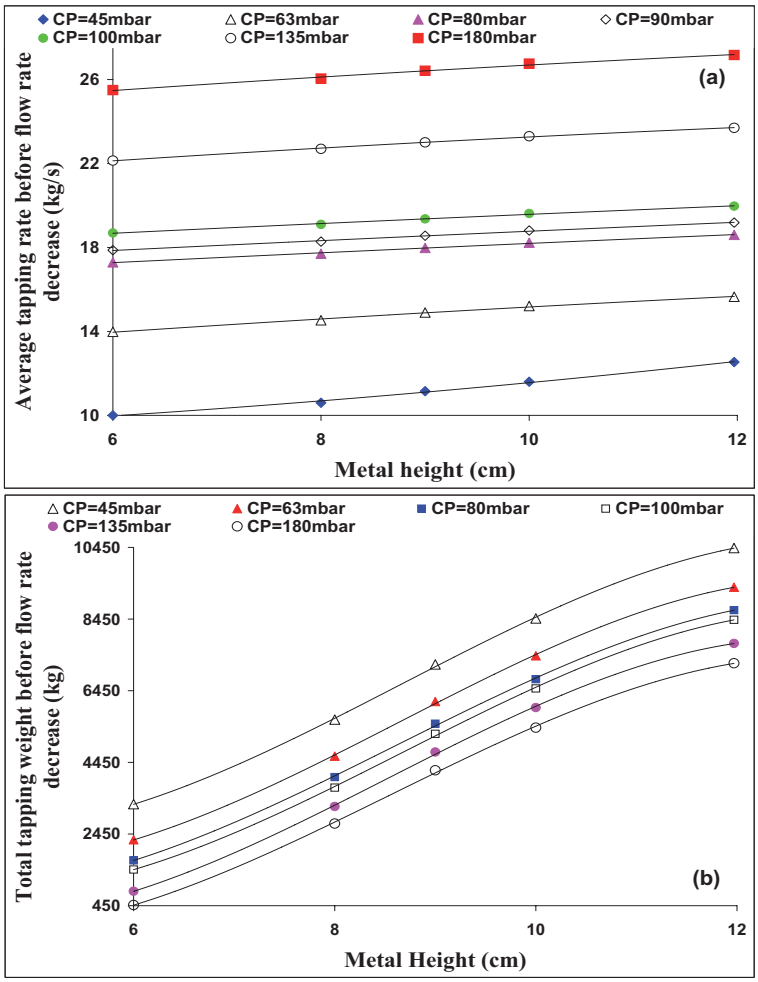

Figure 5.43: The effect of metal height on the average tapping rate (a) and the total tapping weight (b) for different crater pressures in the ferrosilicon (FeSi 55) furnace.

As tapping time expresses the time we can tap before gassing from the taphole starts, tapping time is the most important operational parameter. The effects of metal height and furnace crater pressure on the tapping flow rate and the total tapping weight as a function of time is presented in Figure 5.44.

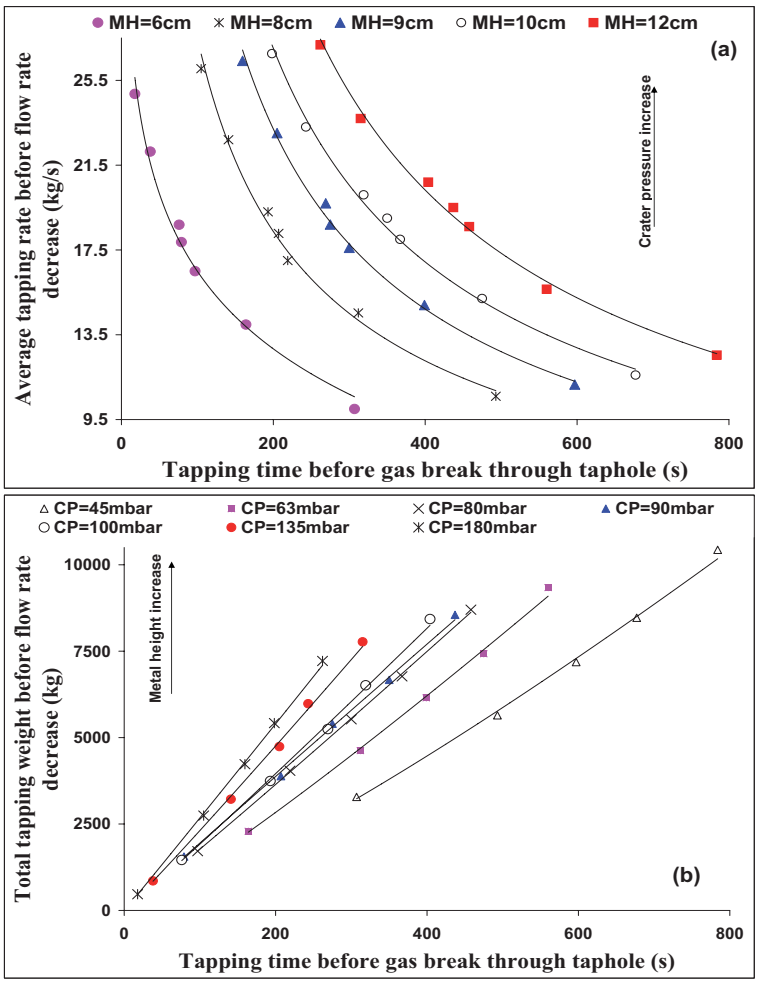

Figure 5.44: The relation between the crater pressure, the metal height and the average tapping flow rate (a) and the relation between the crater pressure, the metal height and the tapped metal mass (b) in the ferrosilicon (FeSi 55) furnace.

Figure 5.45 represents the percentage of the melt which is tapped from the furnace inside as a function of tapping time for different crater pressures and metal heights. As it can be seen when the crater pressure is lower the amount of the metal tapped from the furnace is higher and the tapping time is longer. The general picture is that short tapping times correspond to low metal height and high crater pressures.

However, in these cases with the shortest tapping times the results are telling that more than 90 % of the metal remains inside the furnace when gassing from the taphole is initiated.

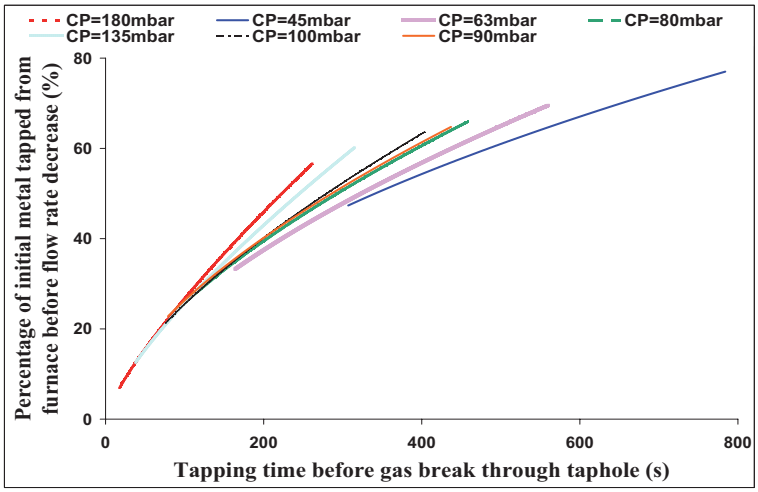

Figure 5.45: Percentage of the melt which is tapped from the ferrosilicon (FeSi 55) furnace as a function of tapping time for different crater pressures and metal heights.

5.4.6 Prediction of the crater pressure and the metal height in the furnace using the results of CFD model

Comparison of the results of the model with the industrial measurements for the total tapping weight before the flow rate decrease leads to a very interesting and valuable result about prediction of the metal height inside the furnace. Figure 5.46 shows both the results of the CFD model and industrial measurements. It is observed that the range of industrial data falls between the metal height of 6 *cm* and 9 *cm* predicted by the model. A point that should be noticed is that the metal height considered in the modeling and the metal volume are not linearly related as the furnace bottom contains a packed bed of solid particles which displaces the melt and has a given porosity distribution.

The same method can be applied for the furnace crater pressure. Figure 5.47 shows the comparison between the model results and the industrial measurements.

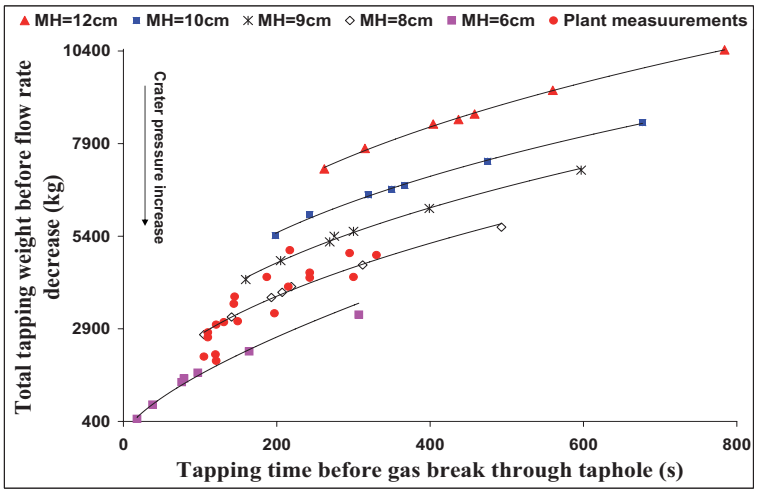

Figure 5.46: Comparison between the model results and industrial measurements in the ferrosilicon (FeSi 55) furnace for the total tapping weight versus tapping time, for different metal heights.

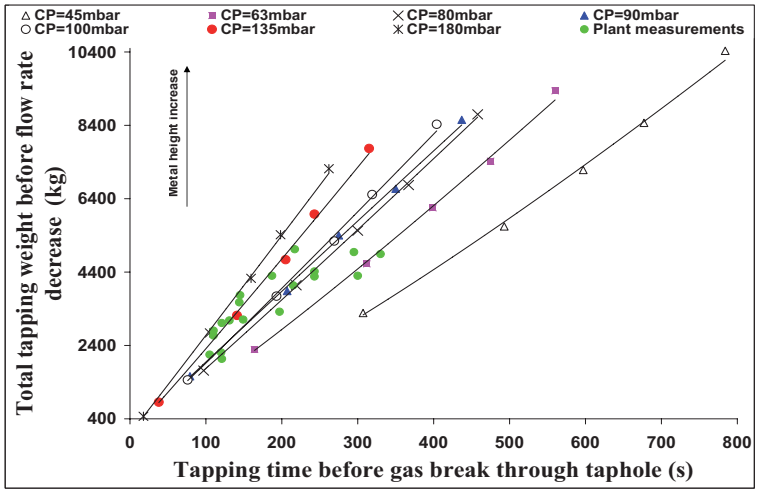

Figure 5.47: Comparison between the model results and industrial measurements in the ferrosilicon (FeSi 55) furnace for the total tapping weight versus tapping time, for different crater pressures.

Comparison of the industrial measurements with the model results support that variations in tapping rate observed industrially may be caused by the dynamic behavior of the furnace crater pressure. From Figure 5.46 we see that the industrially observed variations in tapping rate can be explained by large with industrially observed variations in crater pressures while the initial metal level before tapping starts is around 8 *cm*. From Figure 5.47 we can conclude that metal height variations cannot explain the industrially observer variations in tapping rate and tapping times. Based on these results it is likely that the model will be able to give indications of the furnace crater pressure by having just the information about the total tapping weight.

5.4.7 Investigation of the effect of bottom bed permeability

The packed bed at the furnace bottom has two important effects. Firstly it influences the metal height for a given metal volume. Secondly the packed bed creates a resistance against the flow of melt towards the taphole and leads to reduced tapping flow rate from the furnace. In fact the melt should drain through this packed bed during tapping.

In order to investigate the effect of the backed bed properties on the tapping, two different beds with different permeability (and hence resistance) were considered at the furnace bottom. The permeability difference was considered to be only due to different particles size inside the beds and not due to porosity change. The first bed is the main bed of the model and in the second bed the permeability has been reduced down to 40% of the base case.

The comparison of the tapping parameters between the low and the high permeable beds for the crater pressures ranging between 90 *mbar* up to 180 mbar is presented in Figures 5.48 and 5.49. The initial metal height in all these cases is constant and fixed at 12 *cm*.

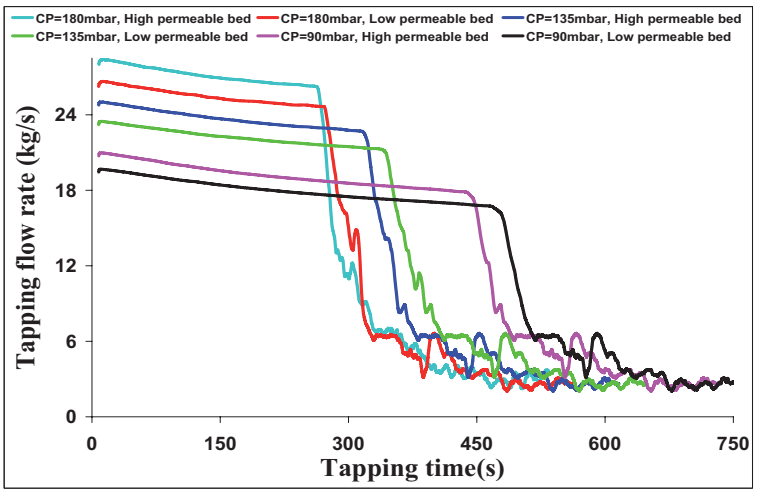

Figure 5.48: The effect of bottom bed permeability on the tapping flow rate from a ferrosilicon (FeSi 55) furnace, the initial metal height is 12 *cm*.

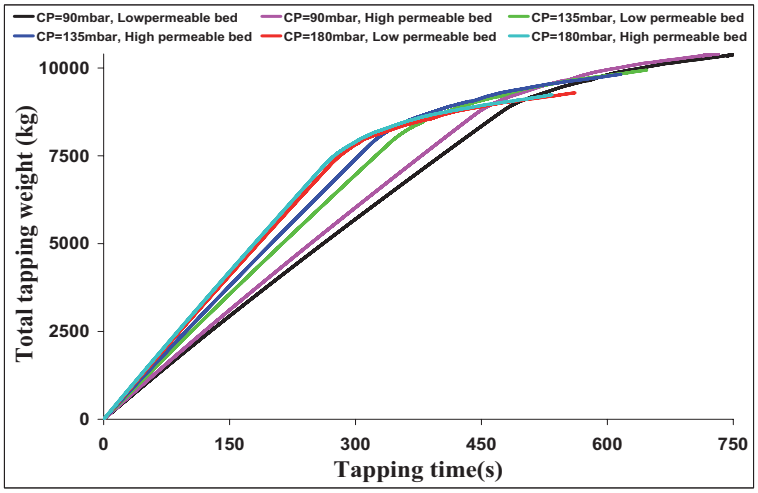

Figure 5.49: The effect of bottom bed permeability on the total tapping weight from a ferrosilicon (FeSi 55) furnace, the initial metal height is 12 *cm*.

As it can be seen from Figure 5.48 the tapping flow rate decreases by decreasing the bed permeability. This is a direct effect of increased resistance against melt

flows in the lower part of the furnace where the melt should be drained through the existing packed bed. It is clear from Figure 5.49 that the effect of bed permeability on the total tapping weight is insignificant as the crater pressure increases, which again highlights the role of furnace crater pressure in the tapping.

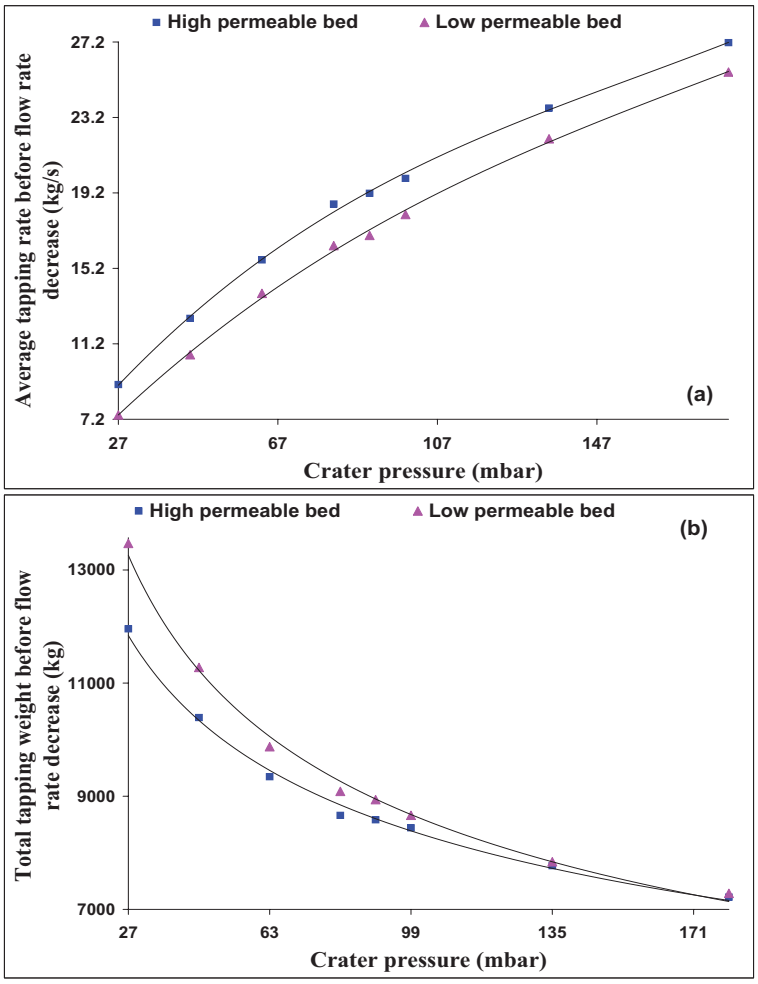

Figure 5.50: The effect of bottom bed permeability on the average tapping flow rate (a) and the total tapping weight (b) for different crater pressures in the ferrosilicon (FeSi 55) furnace, initial metal height is 12 *cm*.

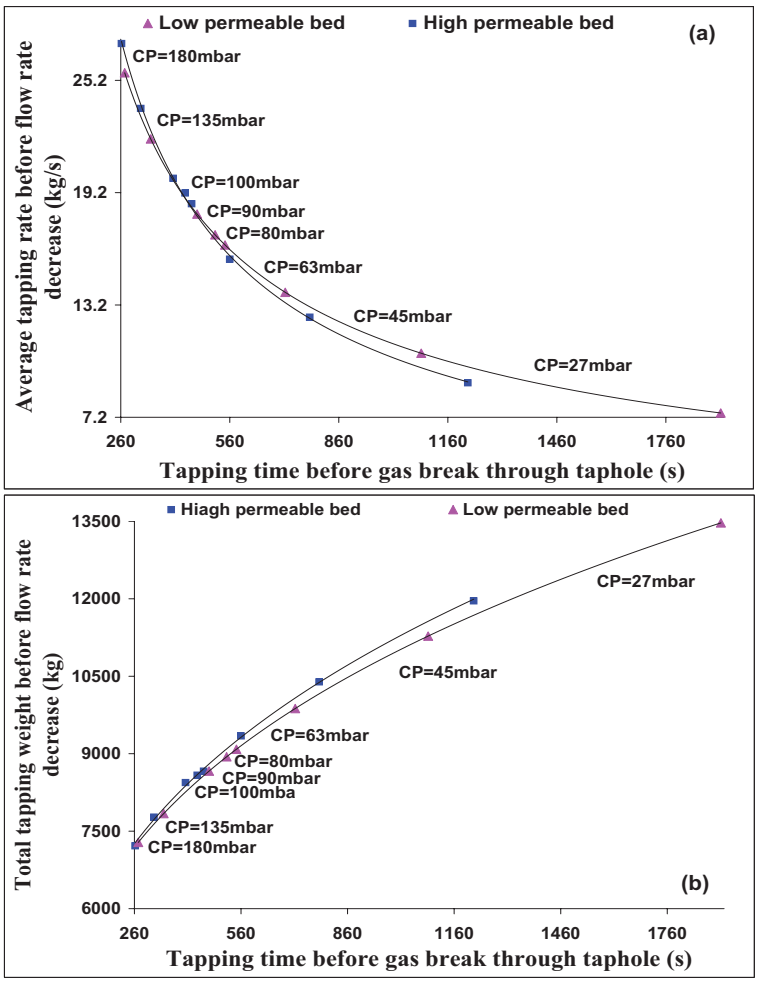

Figure 5.51: The effect of bed permeability on the average tapping flow rate (a) and the total tapping weight (b) versus tapping time for different crater pressures in the ferrosilicon (FeSi 55) furnace, the initial metal height is 12 *cm*.

Figure 5.50 shows that how the bed permeability affects the average tapping rate from the furnace and the total tapping weight before the flow rate drops in different range of crater pressures. It is obvious that the higher the bed permeability the higher the average tapping flow rate. The increased tapping flow rate in the high permeable bed is accompanied with decreased amount of total tapping weight, of

course in shorter period for tapping time, at lower furnace crater pressures.

Investigation of the effect of bed permeability on the average tapping flow rate and the total tapping weight versus tapping time for different range of furnace crater pressures has been presented in Figure 5.51.

As it can be seen from this figure as the crater pressure decreases both the tapping time difference and the proportional difference of the average tapping flow rate increases. The results show that the tapping flow rate is higher in the cases when the bed permeability is higher. It is also observed that both the tapping time difference and the proportional difference of the total weight of the melt tapped from the furnace increases as the furnace crater pressure decreases. The total tapping weight is higher in the case with more permeable bed.

5.4.8 Investigation of the gas flows in the charge materials

The process gases, generated in the furnace crater zone, flow towards the furnace top through the bulk of charge materials. Due to existence of several packed beds with different physical properties inside the charge materials, the gas flow is influenced. Therefore the velocity and the flow rate of process gases in each zone are determined based on the spatial position of the zone. Evaluation of the process gases flows is important because of the reactive nature of these gases. In fact the flow rate of process gases together with the temperature distribution in the furnace, are important parameters to determine the rate of chemical reactions and hence formation of different zones inside the charge materials.

Figure 5.52 shows a 2D view of the model results for the gas velocity in the central plane inside the furnace. As it is seen the gas velocity in the crater zone is higher than the other zones. It is because of generation of process gases in this zone and therefore creation of a high pressure region in the lower part of the furnace.

Tapping flow rate drop is accompanied with gas release from the taphole. This phenomenon changes the gas velocity in the lower part of charge materials and close to the taphole. The gas velocity pattern in the central plane of charge materials inside the furnace when flow rate drops, is shown in Figure 5.53. Comparing this figure with Figure 5.52 shows how the flow rate drop causes creation of a new gas flow pattern inside the furnace.

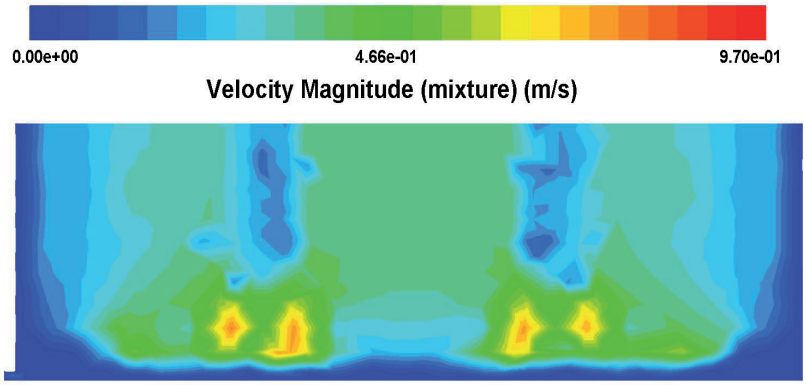

Figure 5.52: The gas velocity pattern in the central vertical plane inside the silicon furnace during normal tapping operation.

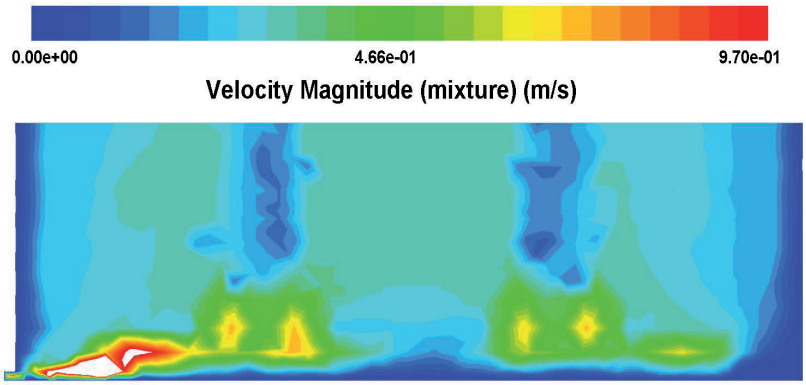

Figure 5.53: The gas velocity pattern in the central vertical plane inside the silicon furnace when tapping flow rate drops and gas is released from the furnace taphole. The white color shows gas velocities higher than the maximum shown in the legend.

In order to investigate more closely the flows of process gases inside the furnace, both during the normal tapping of the melt when only the silicon melt is tapped from the furnace taphole, and when the tapping flow rate drop happens, the gas velocity on the charge materials surface has been presented in Figure 5.54.

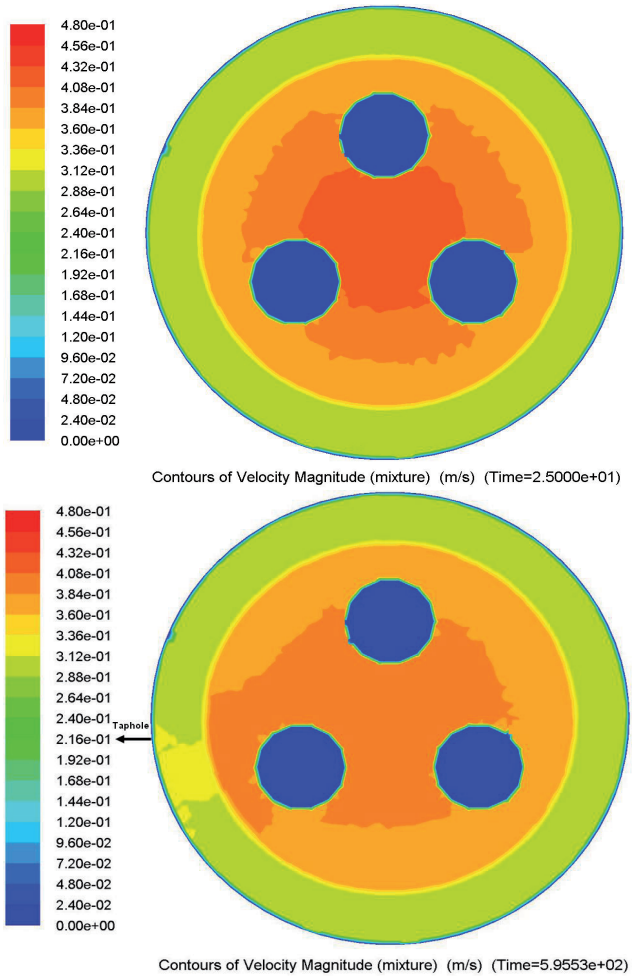

Figure 5.54: Gas flow pattern on the charge surface in the silicon furnace during normal tapping (a) and in the situation where the flow rate drops and gas is released from the furnace taphole (b).

During normal furnace operation, Figure 5.54 (a), it is seen that the gas velocity at the furnace top is high in the furnace center close to the electrodes and it is decreased close to the furnace wall in the inactive part of charge materials. This result is in a very good agreement with the limited observations of the furnace top in the plant. When tapping flow rate drops the gas velocity in the charge materials

decreases due to release of gas from the furnace taphole. From the Figure 5.54 (b) it is also observed that the gas flow pattern through the furnace top depends on the tapping situation. In fact when tapping flow rate drops more gas exits the charge surface close to the taphole area. This result is very important because of the reactive nature of the process gases. Any change in the flow rate of the process gases in the charge materials can lead to increased or decreased chemical reactions rate and modified heat distribution.

Model prediction of formation of gas channels outside the crater zone

Flow of process gases from crater zone towards the furnace top causes formation of gas channels in the charge materials inside the furnace. Results from excavation of a ferrosilicon furnace (Tranell et al. [2010]) prove formation of several gas channels on the outside of the crater walls, starting at the bottom of the crater. These channels were wider at the bottom of the crater (typically 200 *mm*) and narrower at the top.

The existence of such gas channels illustrate the strong gas flows also outside the crater, resulting from vigorous reactions under the electrode. Outside the gas channels and towards the furnace mantle, brown and white condensates were found in a layered structure, suggesting the presence of radial temperature zones in the furnace. Figure 5.55 shows the excavation result of a ferrosilicon furnace (Tranell et al. [2010]).

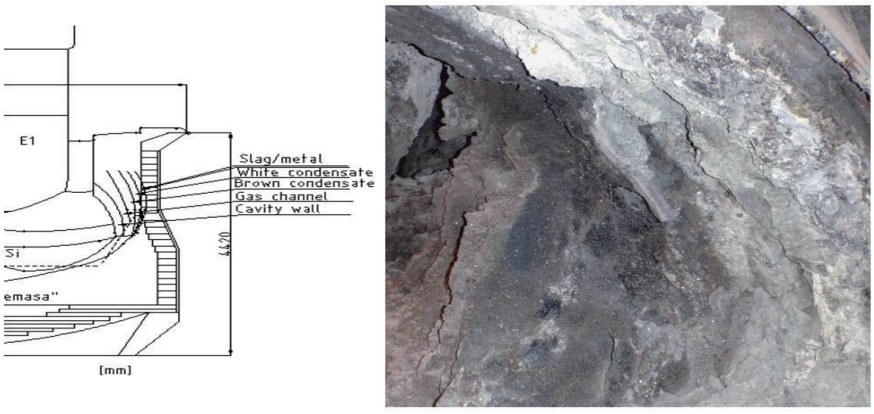

Figure 5.55: Formation of gas channels in the charge materials on the outside of crater wall, results from excavation of an industrial ferrosilicon furnace (Tranell et al. [2010]).

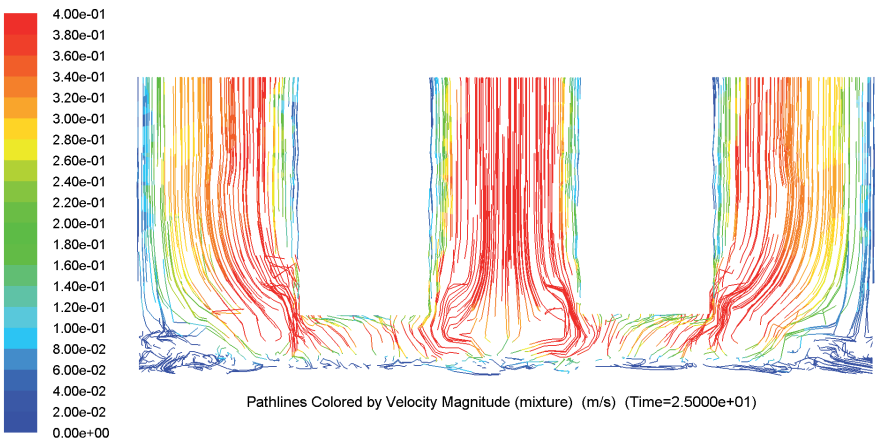

Figure 5.56: Gas flows pathlines in a vertical plane of furnace including electrodes, the gas pathlines show how the gas channels are formed in the charge.

Formation of these gas channels in the charge materials has been predicted by the present CFD model of furnace. The gas flow pattern in the charge materials has been presented in Figure 5.56. It is seen from this figure that the process gases do not move just in the vertical direction. The tilted path of gas flows in the lower part of charge materials close to furnace crater zone can explain why the channels found in excavations are formed.

5.5 Conclusions

A comprehensive model for the tapping process in the submerged arc furnaces used for production of high silicon alloys has been developed. Different important issues which can affect the tapping have been investigated. The most important parameters affecting the tapping are furnace crater pressure, metal height inside the furnace and permeability of different packed beds inside the furnace.

The model results show that the furnace crater pressure affects the tapping process through influencing the tapping flow rate and the fraction of the metal that can be tapped before gassing from the taphole is initiated. The crater pressure is the factor which determines the tapping flow rate by the start of tapping as well as the tapping rate just before flow rate drops. Higher furnace crater pressure leads to higher tapping flow rate from the furnace at the start of tapping and at the same time it causes the faster tapping flow rate drop.

The metal height affects the tapping flow rate and the total tapping weight before flow rate drops. The effect of metal height on the tapping flow rate is not as significant as the effect of furnace crater pressure. A trivial result is that the metal height, directly related to the total metal volume, is the key factor which determines when tapping flow rate drops.

The change of permeability in different zones inside the furnace influences the process gas flow resistance and pressure drop as the gas flows from the crater to the top of the charge. A low permeability in the charge results in a high pressure inside the crater zone. The permeability of the packed bed formed over the furnace bottom, particularly near the taphole zone, affects the tapping flow rate. Reduced permeability of the bottom packed bed causes reduced tapping flow rate and hence longer tapping time. In addition low permeability result in reduces yield of the tapped metal.

The results of the model are in very good agreements with the industrial measurements and the model is able to explain the variations in industrial tapping rates as a result of variations in crater pressure.

Chapter 6

Tapping Gas Collection from Silicon and Ferrosilicon Furnaces

TAPHOLE gassing phenomenon in the submerged arc furnaces used for silicon production poses a significant problem in the view of environment, operation and economy of production. The reason for the gassing is the relatively high pressure of the process gasses in the furnace crater which may escape through the taphole. The combustion of the off gasses creates a high temperature gas containing very fine particles of SiO2 and the result may be internal pollution in the tapping area. In this chapter development of a model for combustion and capturing of the off gasses from the furnace taphole as the feasibility study step for design of a new industrial hood system, is described. Performance of the hood system for different geometries and different operational conditions and industrial challenges for installing the hood are extensively investigated. The results of preliminary industrial tests after installing the system are then presented.

6.1 Pollution sources in the tapping area

Pollution generation in the tapping area is an undesirable effect of furnace tapping. The tapping process is usually the main internal source of pollution in ferroalloys plant. These pollution are composed of gaseous products such as CO_2, NOx, metallic vapor and fine SiO_2 particles. Taphole gassing phenomenon and fumes released from the ladle are the main reason for pollution generation in the tapping area. Figure 6.1 shows the fumes released from melt surface in the ladle during tapping.

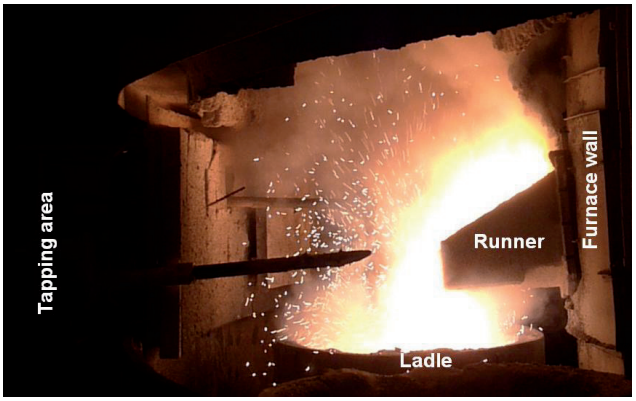

Figure 6.1: The fumes released from ladle during tapping in a submerged arc furnace used for silicon production.

Taphole gassing phenomenon occurs with gas blowing out of taphole in the form of high temperature and high length flame. The release of sparks into tapping area during taphole gassing is shown in Figure 6.2.

Figure 6.2: Sparks released into the tapping area from the furnace taphole due to gassing phenomenon in a silicon production furnace.

As the result of this phenomenon in addition to gaseous pollution a large amount of fine SiO_2 particles are generated. Taphole gassing phenomenon occurs frequently during tapping of silicon and ferrosilicon furnaces. Efficient capturing of the tapping off-gases due to this phenomenon is one of the industrial challenges and it is

still a problem in many plants. Although high suction may improve the conventional off-gas system, it fails to capture the strong gas blows.

Today in most of the silicon and ferrosilicon producing plants there is a hood system consisting of few suction channels in the upper front of furnace taphole. The existing system is to some extent successful in capturing of ladle fumes but it has no or very limited efficiency in capturing of taphole gases during gassing phenomenon. The main difficulty is the high velocity (i.e 50 *m/s*) and high temperature nature of the gases blown out of the taphole. Performance of the existing suction system during normal tapping operation in a silicon furnace is shown in Figure 6.3. Accumulation of dust particles in the form of a thick solid layer of white color on the front walls due to inefficient performance of the ventilation system is clearly seen from this figure.

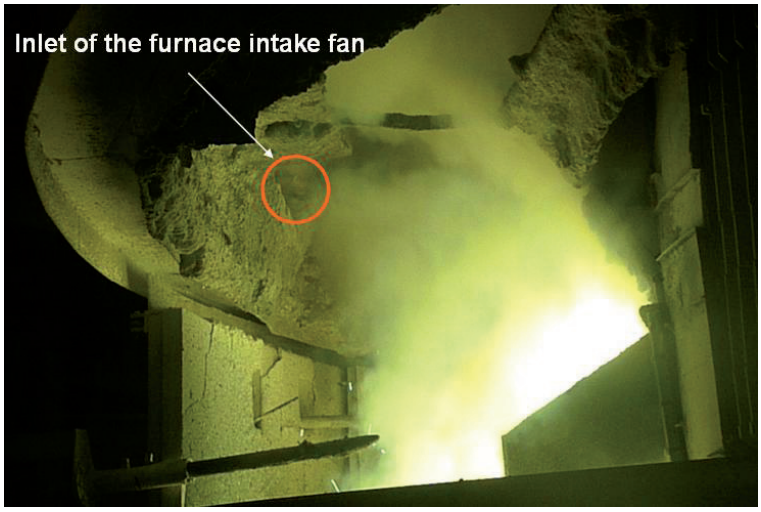

Figure 6.3: Performance of the existing ventilation system in capturing of tapping off-gases and ladle fumes in a silicon furnace.

6.2 New hood system for tapping gas collection

In order to capture the taphole gases from silicon and ferrosilicon furnaces in an efficient way, an initial designing idea from Elkem Company was proposed. The feasibility study regarding successful performance of the proposed design has been done within the present research work. The new hood system, called "*Doghouse*",

is installed over the furnace runner. The hood inlet is in front of the taphole and its outlet is connected to the furnace intake fan. The furnace intake fan is a part of the main off-gas system. Therefore the main duty of Doghouse is to capture the tapping off-gases and directing them towards the main off-gas system. Figure 6.4 shows sketch of the new hood system and the position where it is going to be installed on the furnace. The main idea is that the blowing gas will only need to be directionally tilted towards the hood and the buoyancy of the hot gas will help to achieve this.

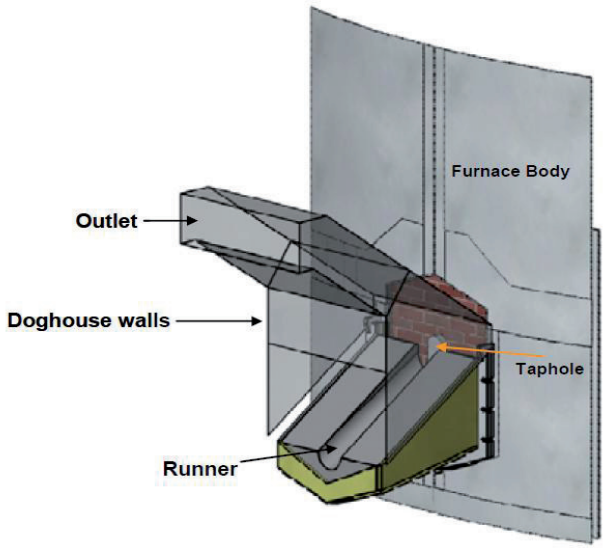

Figure 6.4: Structure of the new hood system designed for capturing of tapping off-gases from silicon and ferrosilicon furnaces.

Two main issues which have been considered while designing the new hood system, are as follows:

- The gas velocity in the hood is a function of the suction capacity of the fan and the hood entrance surface area, $V = f(S, A)$. In the new design the hood entrance area has been reduced therefore the gas velocity in the channel has increased. Increased gas velocity in the hood has led to more efficient capturing of released dust.

- Since the taphole off-gases have very high velocities, a strong change in the

flow direction needs to be created by the fan in order to capture them. In the conventional hood designs the necessary change in the flow direction is very high and hence the required suction capacity is high. While in the new hood design, because of changed channel geometry, change of the flow direction is done using much less fan's suction capacity. This phenomenon has been simply shown in Figure 6.5.

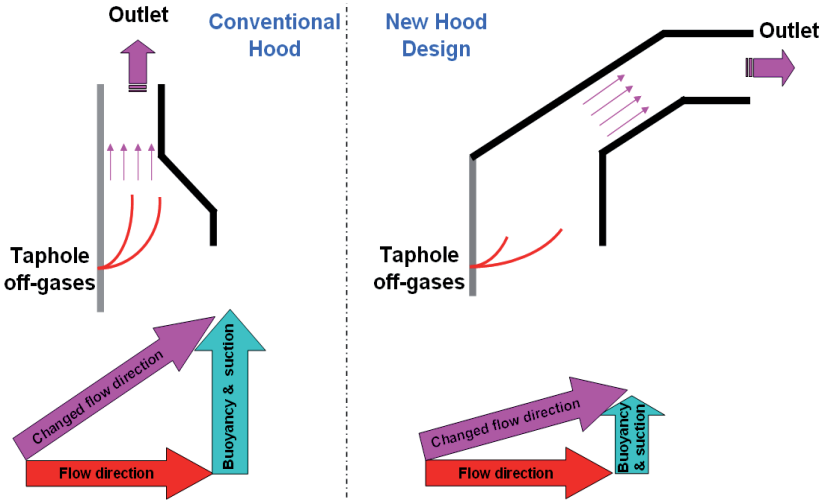

Figure 6.5: Comparing the principle issues between conventional and new hood designs showing much less suction is needed while to change the gas flow direction using the new hood system.

The challenge has been to design the hood in a way which does not make any problem for the operators while furnace tapping. There were several questions about the performance of the system in real operation before it gets ready for industrial tests. The questions were mostly about the taphole off-gas velocity, temperature distribution both in the off-gases and the Doghouse walls, required suction rate for capturing the off-gases and pressure drop in the hood channel. In order to find answer for these questions, development of a model for simulation of taphole gassing phenomenon and investigation of the hood performance in different operational situations was necessary.

6.3 CFD modeling

Since the modeling results are going to be used as an important step in feasibility studies of the hood design, it should include essential aspects. The model should address the industrial problem, performance of the designed system in different operational situations and the effect of different parameters on the efficiency of the system. A comprehensive CFD model for investigation of the above mentioned issues has been developed. The model is 3D and contains almost all aspects of the problem such as gas blowing out from furnace taphole, pollution generation due to combustion of off-gasses, concentration and flows of the off-gases in the tapping area and heat distribution with considering different mechanisms for heat transfer. The model also evaluates performance of the new hood in different situations within several case studies.

6.3.1 Model governing equations

The model includes one phase which is gas but there are different species in the gas phase. The governing equations for mass, momentum and energy conservation and also species equation have been explained in previous chapters and therefore are not repeated here again. In addition to them there are other equations describing turbulence, radiation and combustion models which are explained as follows:

Turbulence model

Due to existence of gases with high velocity and also combustion phenomenon in the system under consideration, using turbulent flows equations in the model are necessary. Using Large Eddy Simulation (LES) turbulence equations in modeling of the systems which include combustion phenomenon is recommended by different authors due to its accuracy. LES model can be used only in 3D transient CFD models and because the present work focuses only on modeling of the system in the steady state situation, it is not possible to apply LES turbulence model here. In this work the standard $k-\omega$ turbulence model is used. The standard $k-\omega$ is an empirical model based on model transport equations for the turbulence kinetic energy (k) and the specific dissipation rate (ω), which can also be thought of as the ratio of ε to k (Wilcox [1998] [1998]). The turbulence kinetic energy, k, and the specific dissipation rate, ω, are obtained from the following transport equations:

$$\frac{\partial}{\partial t}(\rho k)+\frac{\partial}{\partial x_i}(\rho k u_i)=\frac{\partial}{\partial x_j}\left[(\mu+\frac{\mu_t}{\sigma_k})\frac{\partial k}{\partial x_j}\right]+G_k-Y_k+S_k \qquad (6.1)$$

$$\frac{\partial}{\partial t}(\rho\omega) + \frac{\partial}{\partial x_i}(\rho\omega u_i) = \frac{\partial}{\partial x_j}\left[(\mu + \frac{\mu_t}{\sigma_\omega})\frac{\partial \epsilon}{\partial x_j}\right] + G_\omega - Y_\omega + S_\omega \tag{6.2}$$

In these equations, G_k represents the generation of turbulence kinetic energy due to mean velocity gradients. G_ω represents the generation of ω. Y_k and Y_ω represent the dissipation of k and ω due to turbulence. σ_k and σ_ω are the turbulent Prandtl numbers for k and ω, respectively. S_k and S_ω are user-defined source terms. The turbulent viscosity, μ_t, is computed by combining k and ω as follows:

$$\mu_t = \alpha^* \frac{\rho k}{\omega} \tag{6.3}$$

The coefficient α^* damps the turbulent viscosity causing a low-Reynolds-number correction. It is given by:

$$\alpha^* = \alpha^*_\infty \left(\frac{\alpha^*_0 + Re_t/R_k}{1 + Re_t/R_k}\right) \tag{6.4}$$

Note that, in the high-Reynolds-number form of the $k-\omega$ model, α^*= α^*_∞ = 1.

Table 6.1: Empirical constants used in standard $k-\omega$ model.

α^*_0	R_k	σ_k	σ_ω
0.024	6.0	2.0	2.0

Radiation model

The gas radiation in this study is modeled by using the standard P1 model. The P1 radiation model is based on the expansion of the radiation intensity into orthogonal series of spherical harmonics. The radiative flux is given by equation 6.5 where G is the incident radiation and C is the linear-anisotropic phase function coefficient (Cheng [1964] and Siegel and Howell [1992]).

$$q_r = -\Gamma \nabla G \tag{6.5}$$

$$\Gamma = \frac{1}{\left(3(a + \sigma_s) - C\sigma_s\right)} \tag{6.6}$$

The transport equation for G is defined in equation 6.7 where σ is the Stefan-Boltzmann constant and S_G is a user-defined radiation source.

$$\nabla \cdot (\Gamma \nabla G) - aG + 4a\sigma T^4 = S_G \tag{6.7}$$

Equation 6.7 is solved in order to determine the local radiation intensity. Combining equations 6.5 and 6.7 gives lead to Equation 6.8 which can then be directly substituted into the energy equation to account for heat sources (or sinks) due to radiation.

$$\triangle q_r = aG + 4a\sigma T^4 \tag{6.8}$$

Combustion model

The combustion of off-gasses from taphole according to equations 3.5 and 3.6, affects the energy distribution and the velocity pattern of the gas flows in the system and must be taken into consideration in the modeling process. In the calculations related to combustion, both the Eddy-Dissipation and Eddy-Dissipation Concept models were tested. Since combustion of tapping off-gases like SiO gas occurs very fast, the Eddy-Dissipation model was preferred to be implemented in this study. In this model the net rate of production of species i due to reaction r, $R_{i,r}$, is given by the smaller (i.e., limiting value) of the two expressions below (Magnussen and Hjertager [1976]):

$$R_{i,r} = \nu_{i,r}^{'} M_{\omega,i} A \rho \frac{\epsilon}{k} \mathbf{min}_R \left[\frac{Y_R}{\nu_{R,r}^{'} M_{\omega,R}} \right] \tag{6.9}$$

$$R_{i,r} = \nu_{i,r}^{'} M_{\omega,i} A B \rho \frac{\epsilon}{k} \frac{\sum_p Y_p}{\sum_j^N \nu_{j,r}^{''} M_{\omega,j}} \tag{6.10}$$

Where Y_p is the mass fraction of any product species, p, Y_R is the mass fraction of a particular reactant R, A is an empirical constant equal to 4.0 and B is an empirical constant equal to 0.5. In these equations, the chemical reaction rate is governed by the large eddy mixing time scale, k/ϵ, as in the eddy-breakup model of Spalding [1970]. Combustion proceeds whenever turbulence is present ($k/\epsilon > 0$).

Adiabatic temperature of combustion for both SiO and CO gas with oxygen in the air was calculated separately and the results were used in the model. In the calculations two assumptions were considered. First of all the combustion considered to be adiabatic and at constant volume and second of all perfect mixing of reactants with a mixing rate equal to 1 was applied. Table 6.2 shows the results of calculation of adiabatic temperature of combustion for some species.

Table 6.2: Thermodynamic data for adiabatic temperature of combustion of some species.

Species	**Enthalpy of formation (*kJ/mol*)**	**Specific heat (*J/kg.K*)**
N_2	0	$939.8 + 0.2802 \times T - 5.308 \times 10^{-5} \times T^2$
O_2	0	$854.1 + 0.2765 \times T - 5.404 \times 10^{-5} \times T^2$
SiO	-98.4	$1.34 + 1.76 \times 10^{-4} \times T$
SiO_2	-910	$2.8 + 5.35 \times 10^{-4} \times T$
CO	-110	$940 + 0.3017 \times T - 6.091 \times 10^{-5} \times T^2$
CO_2	-393.5	$581.4 + 1.089 \times T - 5.215 \times 10^{-4} \times T^2 + 8.682 \times 10^{-8} \times T^3$

It was assumed that the taphole off-gas is composed of 50% SiO and 50% CO. Therefore properties of the gas mixture were determined based on this assumption.

6.3.2 Hood geometry

Figure 6.6 shows the conventional ventilation system including the furnace intake fan. The original geometry of the hood installed on a furnace is presented in Figure 6.7. The taphole diameter was selected to be 7.5 *cm*. The real diameter in the silicon furnaces is more but during the gassing phenomena the off-gas does not blow-out from the total surface of the taphole. Because even in the taphole gassing mode there is some flow of metal from the taphole. Therefore the considered taphole diameter seems to be reasonable.

Performance of the hood system in capturing of the ladle fumes is evaluated through adding the ladle into the described geometry of the system. Figure 6.8 shows the system including the ladle. Moreover further investigation of the system efficiency is studied in the situation where a lid is put on the ladle in order to direct the ladle fumes towards the hood. The system geometry in this case is shown in Figure 6.9.

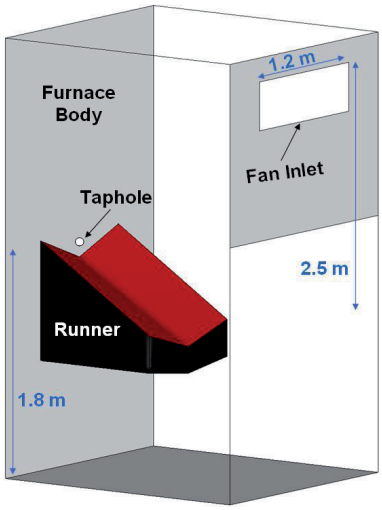

Figure 6.6: Geometry of the conventional ventilation system used for CFD modeling showing the fan inlet located in upper front of the furnace taphole.

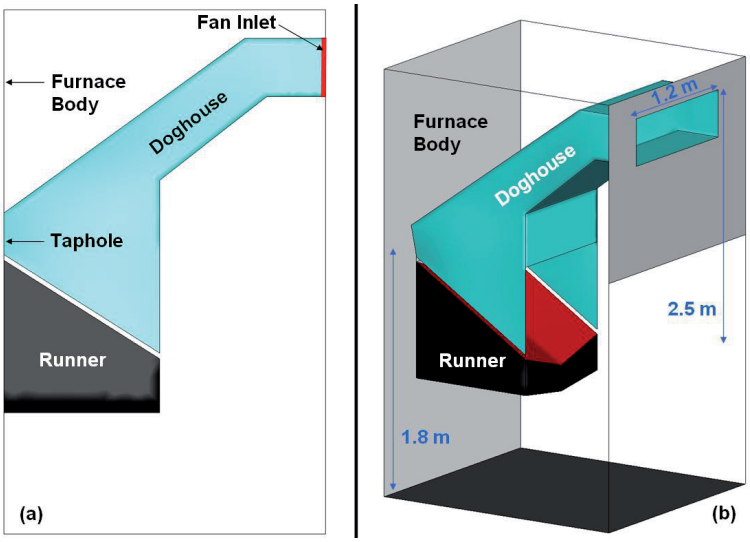

Figure 6.7: Original geometry of the hood used for CFD modeling, 2D side view (a) and 3D view including the main dimensions (b).

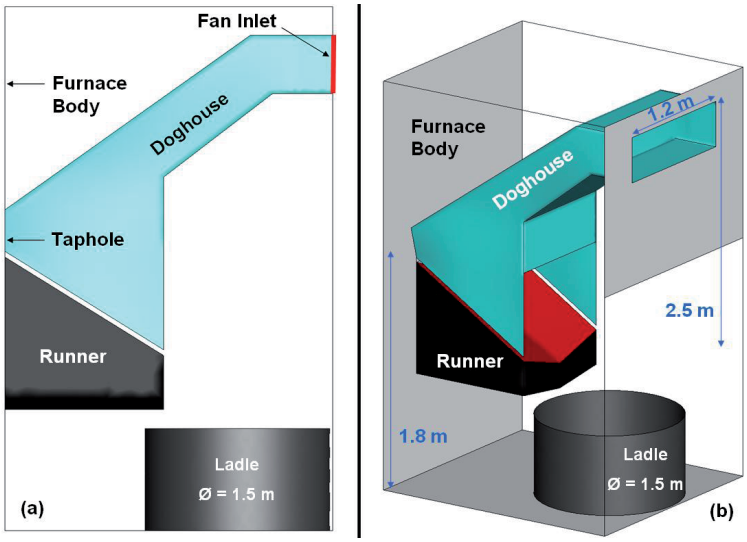

Figure 6.8: Geometry of the hood including the ladle used for CFD modeling, 2D side view (a) and 3D view showing the main dimensions (b).

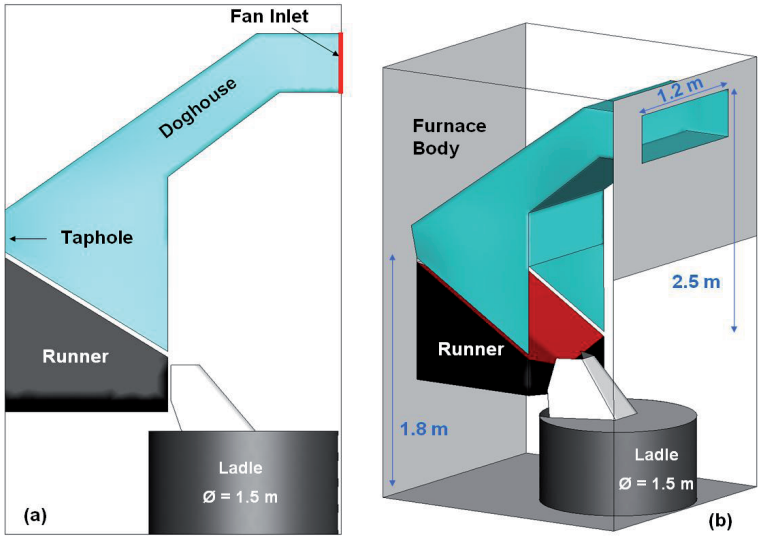

Figure 6.9: Geometry of the hood including the ladle and its lid used for CFD modeling, 2D side view (a) and 3D view showing the main dimensions (b).

6.3.3 Numerical method and boundary conditions

The numerical approach used in this study is based on finite volume method (FVM). In order to perform the simulations the commercial CFD software Fluent version 6.3.26 is applied. The transport equations for mass, momentum and energy together with described equations of heat transfer, combustion and turbulent flows are solved simultaneously. The geometry contains of 360000 meshes and very fine meshes have been considered for the zones where combustion happens. A graphical presentation of the computational grid used for modeling is shown in Figure 6.10.

In order to perform calculations of CFD model different boundary conditions are defined. Definition of the boundary condition is done based on the structure of the ventilation system. According to them and because the mixture of off-gasses is blown-out of the taphole during gassing phenomenon, the taphole is modeled as mass flow inlet. Temperature of the gas mixture released from the furnace taphole is considered 1400$^{\circ}C$. The hood channel outlet is modeled as outflow. The suction rate by the intake fan determines the amount of the off-gasses which flows through the outlet. The environment around the new hood is modeled as atmospheric pressure inlet. Therefore the model is able to consider the effect of "Hall-Wind". A part of the runner walls which molten silicon flows through that into the ladle, is modeled as high temperature wall. The wall temperature considered to be around 1500$^{\circ}C$. The reason to define high temperature boundary condition for this wall was to take into account the effect of metal flow on radiative heat transfer. In the cases including the ladle a source term for the fumes released from the melt surface during tapping, has been defined.

The velocity of tapping off-gases in the normal operation is around 10 *m/s*. When taphole gassing phenomenon occurs, the off-gas velocity increases up to 50 *m/s* but in severe cases it may goes even higher. In this research several case studies considering wide range for gas velocities blown-out of the taphole, from 10-100 *m/s*, and different suction rates provided by the furnace intake fan, from 5000-30000 Nm^3/hr, have been performed. Therefore different modes of the gassing phenomenon from less intensive to most sever cases which may happen in real operation of the furnace are covered in the present simulations.

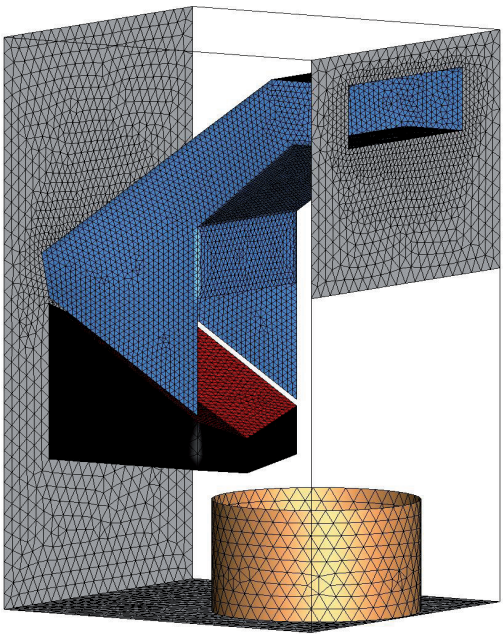

Figure 6.10: Computational grid including the hood system, surrounding area and ladle, only meshes on the surfaces have been shown.

6.3.4 Results and discussions

Depending on the described case studies he results are presented in different categories. First of all the taphole gassing phenomenon in the situation where the hood system has not been installed is investigated. Then performance of the hood in different conditions is evaluated through defining several scenarios. The CFD model is fully 3D but in order to have better graphical view the central plane perpendicular to the furnace wall, and hence taphole, and parallel to the side walls of the hood has been selected for presentation of the most results.

Case 1: Taphole gassing phenomenon - Conventional ventilation system

As the first case study the normal operational situation and the performance of the system, is investigated. Figure 6.11 shows the results of the model for performance of the conventional ventilation system in capturing of tapping off-gases and ladle fumes during normal tapping where the off-gas velocity from the taphole is 10 *m/s*.

The suction rate crated by the furnace intake fan in this case is 15000 Nm^3/hr.

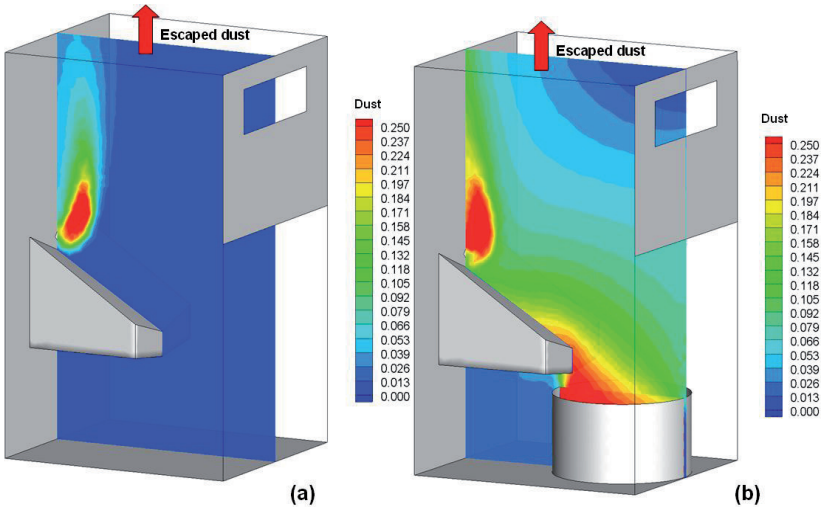

Figure 6.11: Mass fraction of dust due to combustion of taphole off-gases and ladle fumes when the gas velocity is 10 *m/s*, without ladle (a) and considering the ladle fumes (b).

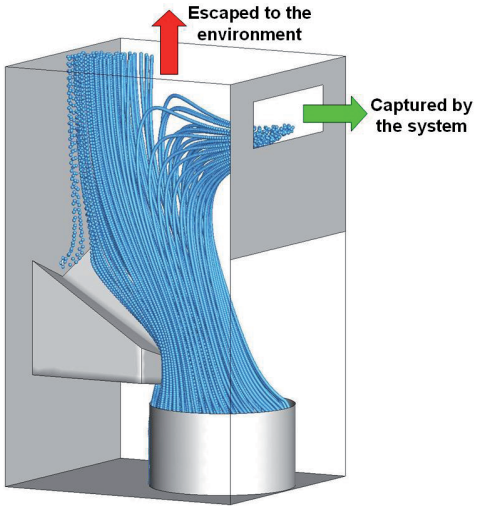

Figure 6.12: Pathlines of the dust particles released in the tapping area, a large portion of the dust is not captured by the existing ventilation system.

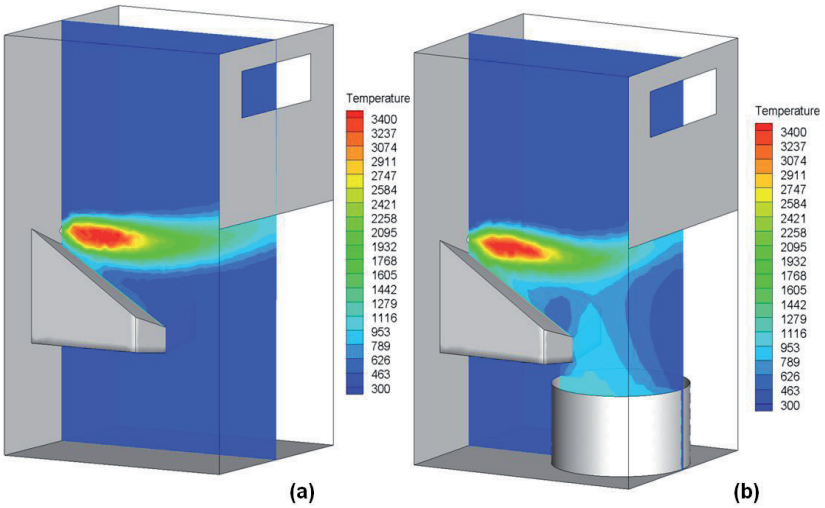

Figure 6.13: The flame temperature due to combustion of taphole off-gases where the gas velocity is 50 *m/s* and the fan suction rate is 15000 Nm^3/hr.

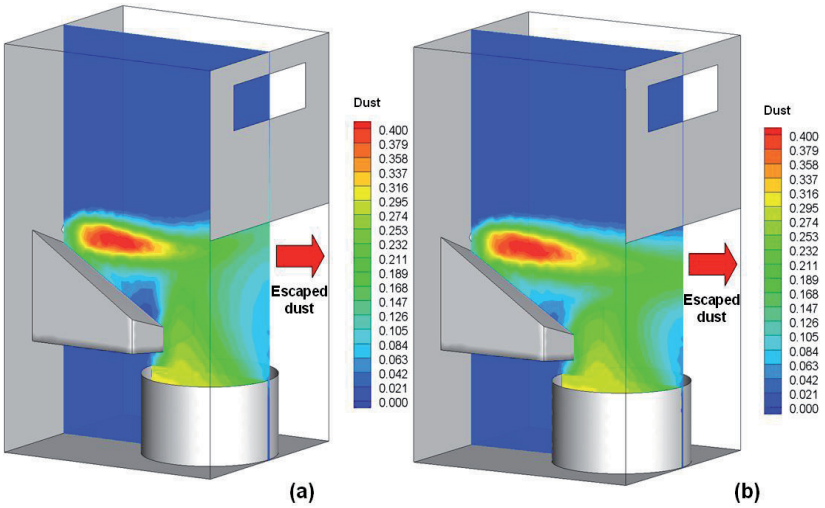

Figure 6.14: Mass fraction of dust in the tapping area from combustion of taphole off-gases and ladle fumes where the taphole gas velocity is 50 *m/s* (a) and 100 *m/s* (b).

Figure 6.12 represents the pathlines of the dust particles which are released in

the tapping area for the case study (b) in Figure 6.11.

The flame temperature due to combustion of tapping off-gases in the case where the gas velocity is 50 *m/s* has been presented in Figure 6.13. As it is seen from this figure the flame has a length of 2-3 *m* which is in good agreement with industrial observations when taphole gassing phenomenon occurs.

As it can be seen from the results of the CFD model the old ventilation system does not work efficiently. Therefore large amount of dust is released in the tapping hall. Performance of the system in the case of taphole gassing where the off-gas velocities are 50 *m/s* and 100 *m/s*, are shown in Figure 6.14. It is clear that the hood system is not able to capture the dust which is released in the tapping area. Results of the model for the average temperature, velocity and mass fraction of dust at the fan inlet are briefly presented in Table 6.3. In the table Efficiency represents the ratio between dust captured by the suction system compared to total amount of dust.

Table 6.3: Results of the model for average temperature, velocity and dust concentration at the fan inlet for different taphole off-gas velocities using the conventional system.

Case Study	Temp. (*K*)	Dust conc. (mg/Nm^3)	Velocity (*m/s*)	Efficiency (%)
V=10 *m/s* - Without ladle	301	20	13.9	13.8
V=10 *m/s* - With ladle	306	831	14.0	36.8
V=50 *m/s* - Without ladle	325	362	15.0	23.4
V=50 *m/s* - With ladle	320	376	14.9	26.5
V=100 *m/s* - Without ladle	304	81	14.1	8.4
V=100 *m/s* - With ladle	301	15	14.0	1.0

Case 2: Performance of the new hood system - without considering the ladle fumes

As the second case study performance of the new hood system in the situation where the only pollution source is tapping off-gases, is evaluated. The model is tuned for different tapping gas velocities and suction rates provided by the furnace intake fan.

Figure 6.15 shows mass fraction of the dust in the hood channel in a central plane perpendicular to the furnace wall. It is clearly seen that the off-gases are completely captured by the hood system in these cases.

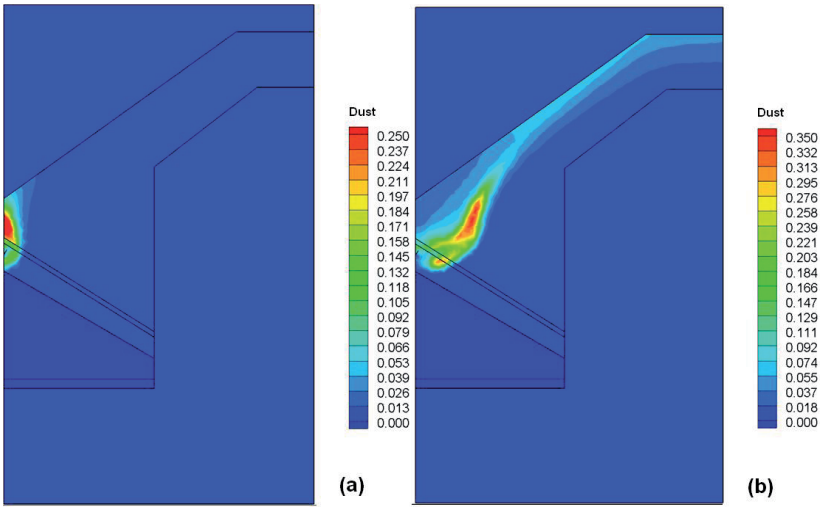

Figure 6.15: Mass fraction of dust in the hood when the tapping gas velocity is 10 *m/s* (a) and 50 *m/s* (b) and the suction rate provided by the furnace intake fan is 15000 Nm^3/hr.

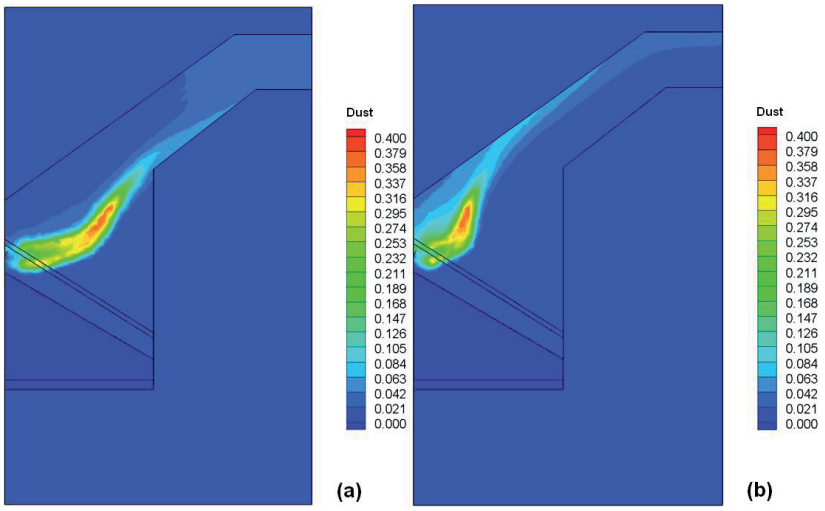

Figure 6.16: Mass fraction of dust in the hood when the tapping gas velocity is 100 *m/s* and the suction rate provided by the furnace intake fan is 15000 Nm^3/hr (a) and 30000 Nm^3/hr (b).

The hood performance in the severe situation when the taphole gas velocity is 100 *m/s* and the capacity of the furnace intake fan is 15000 Nm^3/hr and 30000 Nm^3/hr, has been presented in Figure 6.16. Such high velocity for taphole off-gases is very unlikely to happen during furnace operation, however as it can be seen from this figure, the hood shows a successful performance in both cases although increased suction rate leads to a better result. Temperature distribution in the hood channel for these cases is shown in Figure 6.17.

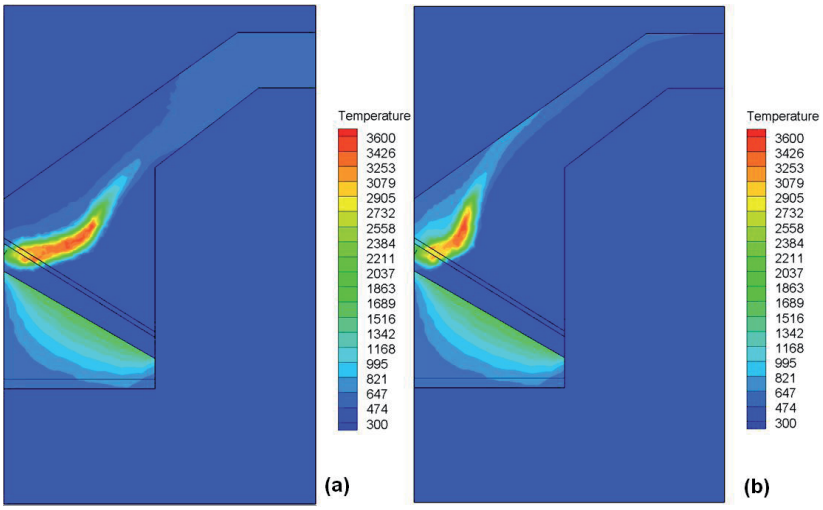

Figure 6.17: Temperature distribution in the hood when the tapping gas velocity is 100 *m/s* and the suction rate provided by the furnace intake fan is 15000 Nm^3/hr (a) and 30000 Nm^3/hr (b).

Table 6.4: Results of the model for average temperature, velocity and dust concentration at the fan inlet during hood operation. A wide range for tapping gas velocities, V, and intake fan capacities, S, have been reported.

Case Study	Temp. (K)	Dust conc. (mg/Nm^3)	Velocity (m/s)	Efficiency (%)
V=10 *m/s* - S=15000 Nm^3/hr	327	196	13.7	>99
V=50 *m/s* - S=15000 Nm^3/hr	386	856	16.1	>99
V=100 *m/s* - S=15000 Nm^3/hr	460	1440	18.9	>99
V=50 *m/s* - S=30000 Nm^3/hr	348	924	29.0	>99
V=100 *m/s* - S=30000 Nm^3/hr	384	1701	31.9	>99

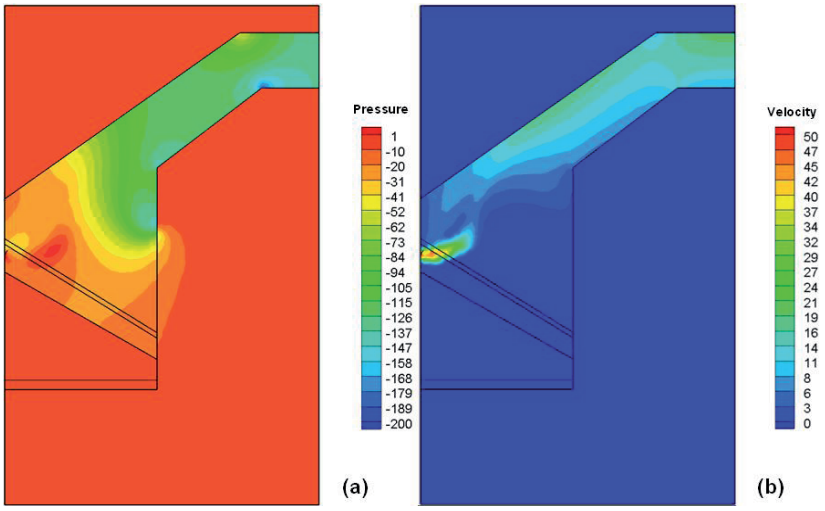

Figure 6.18: Pressure drop (a) and gas velocity pattern (b) in the hood when the tapping gas velocity is 50 *m/s* and the fan suction rate is 15000 Nm^3/hr.

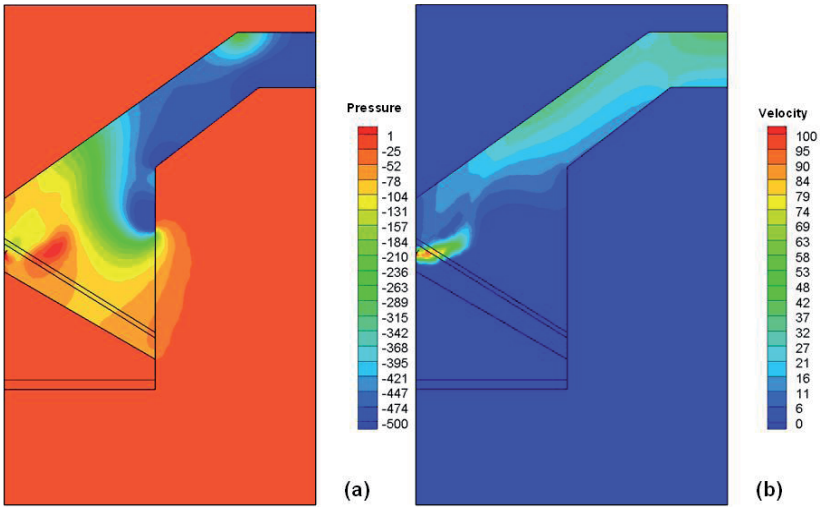

Figure 6.19: Pressure drop (a) and gas velocity pattern (b) in the hood when the tapping gas velocity is 100 *m/s* and the fan suction rate is 30000 Nm^3/hr.

Comparison between some of the operational data resulted from model for the above case studies are given in Table 6.4.

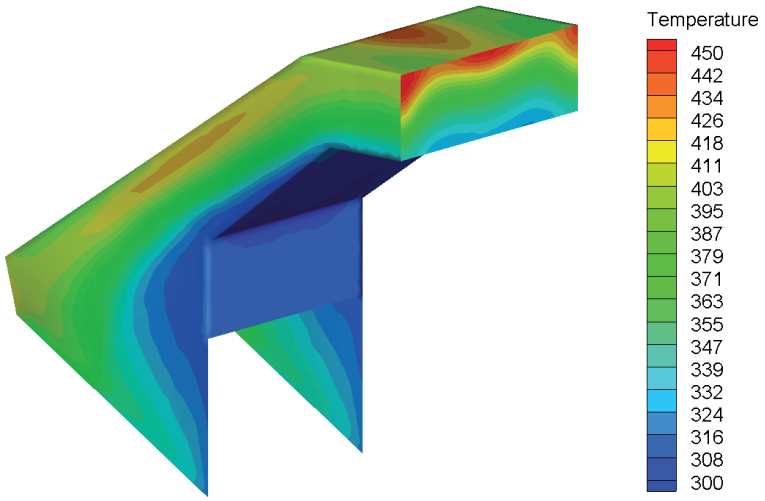

Figure 6.20: Temperature distribution in the channel body in the situation where the taphole gas velocity is 100 *m/s* and the fan suction rate is 30000 Nm^3/hr.

The reason for big difference between the outlet velocities is due to different pressure drop in the hood channel in these cases. In fact higher pressure drop in the hood causes higher gas velocities at the channel outlet. Examples of the pressure drop in the hood channel and the related gas velocity patterns are shown in Figures 6.18 and 6.19.

Increased fan speed sucks more cold air from the environment into the hood and therefore the gas temperature at the outlet decreases. Decreased fan capacity has an inverse effect and causes increased temperature in the exiting gas flow.

Case 3: Performance of the new hood system - considering the ladle fumes

The new hood system was mainly designed for capturing of taphole off-gases in order to avoid release of them in the tapping area. However in the real operation the ladle fumes as another source of pollution in the tapping area do exist. In order to answer what is the effect of hood performance on the flows of the ladle fumes in the tapping hall, a new CFD model by considering the ladle was developed. In this new model a source term for the dust released from the melt surface in the ladle is defined. The upwards velocity of the ladle fumes is considered to be 1 *m/s* which is an approximation made by the movies taken from the real operation. The dust concentration in the released fume is assumed to be 30%.

Results of the model show that the new hood system affects the flows of the fumes released from the ladle. In fact a large portion of the ladle fumes can be captured by the hood system. Since due to operation of the hood a large volume of the air from the environment around the ladle is sucked into the channel, therefore the ladle fumes which follow the air flows are directed towards the hood inlet. Efficiency of the hood depends on the capacity of intake fan and velocity of the taphole off-gases.

Mass fraction of dust in the tapping area and temperature distribution in the hood channel for two case studies have been shown in Figures 6.21 and 6.22. It is clearly seen from these figures that when the hood operates, in addition to tapping off-gases a portion of the ladle fumes can be captured by the hood system.

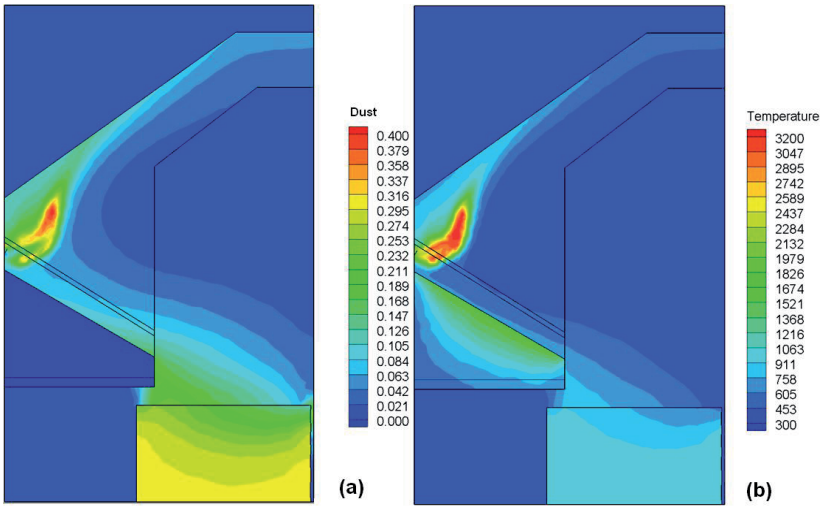

Figure 6.21: Mass fraction of dust (a) and temperature distribution in the hood channel (b) when the tapping gas velocity is 50 *m/s* and the suction rate provided by the furnace intake fan is 15000 Nm^3/hr.

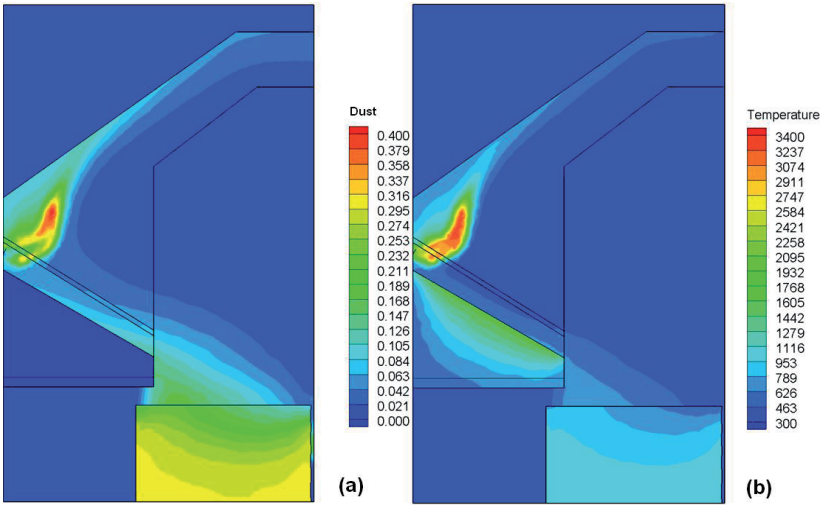

Figure 6.22: Mass fraction of dust (a) and temperature distribution in the hood channel (b) when the tapping gas velocity is 100 *m/s* and the suction rate provided by the furnace intake fan is 30000 Nm^3/hr.

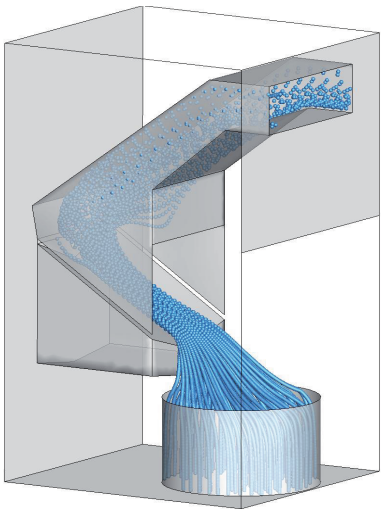

Figure 6.23: Pathlines of ladle fumes towards the hood in the situation when the tapping gas velocity is 50 *m/s* and the fan suction rate is 15000 Nm^3/hr.

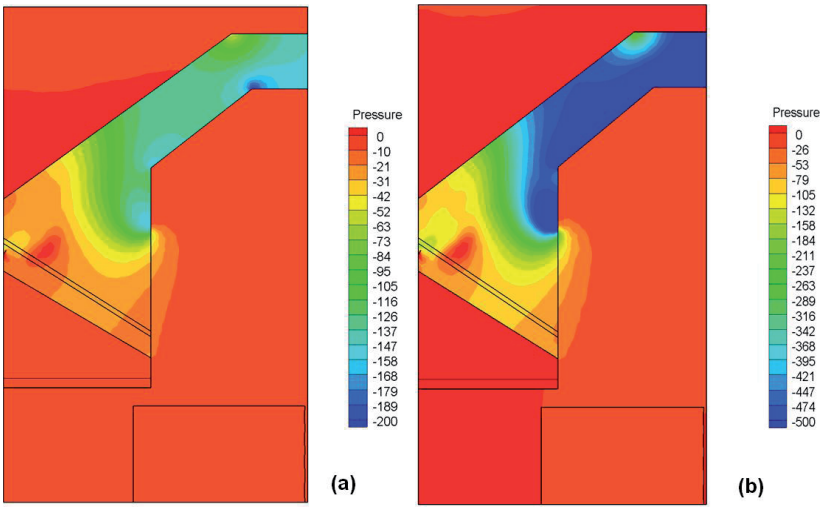

Figure 6.24: Pressure drop in the hood channel in the situation where the taphole gas velocity is 50 *m/s* and the fan suction rate is 15000 Nm^3/hr (a) and 30000 Nm^3/hr (b).

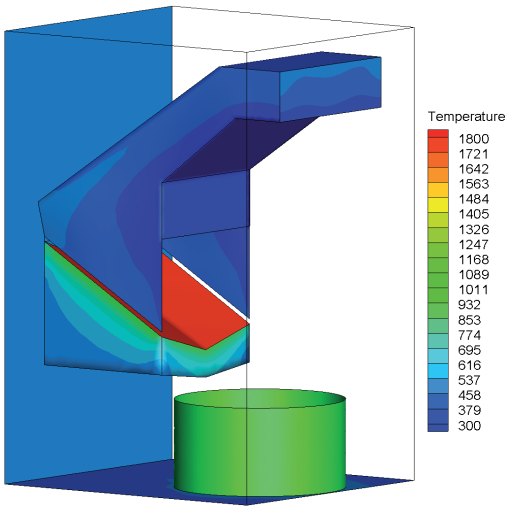

Figure 6.25: Contours of temperature distribution on the walls of the system in the situation where the taphole gas velocity is 50 *m/s* and the fan suction rate is 15000 Nm^3/hr.

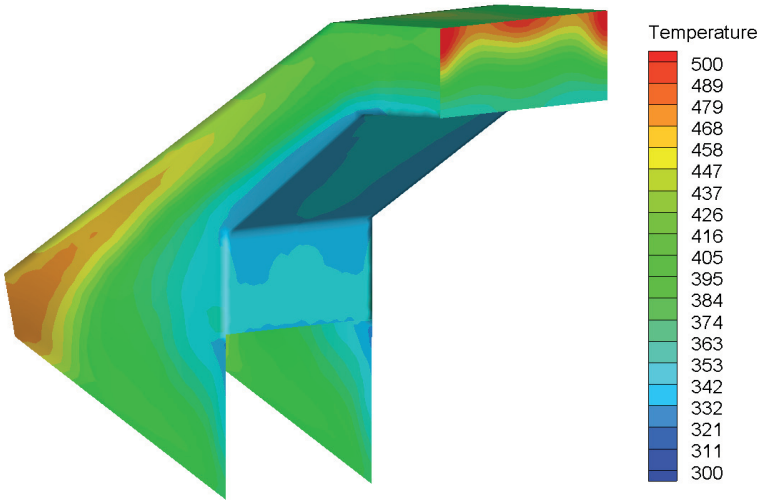

Figure 6.26: Temperature distribution in the channel body in the situation where the taphole gas velocity is 50 *m/s* and the fan suction rate is 15000 Nm^3/hr.

Pathlines of the ladle fumes towards the hood channel are shown in Figures 6.23.

The modeling results show that the hood system also shows a good performance even when severe taphole gassing occurs (see Figures 6.22. The results also show more efficient performance of the hood system by increasing the capacity of the furnace fan.

Some practical information about the hood operation while considering the ladle fumes have been briefly reported in Table 6.5.

Table 6.5: Results of the model for average temperature, velocity and dust concentration at the fan inlet during operation of the hood. A wide range for tapping gas velocities, V, and intake fan capacities, S, have been reported.

Case Study	Temp. (K)	Dust conc. (mg/Nm^3)	Velocity (m/s)	Efficiency ($\%$)
V=50 *m/s* - S=15000 Nm^3/hr	425	1925	17.5	83.8
V=50 *m/s* - S=30000 Nm^3/hr	371	2179	30.7	94.9
V=100 *m/s* - S=30000 Nm^3/hr	407	2834	33.7	92.1

Case 4: Performance of the new hood system - considering a lid for ladle

The hood system shows a very good performance in capturing of both tapping off-gases and ladle fumes. However in order to have a more efficient performance of the hood an industrial suggestion is to put a lid over the ladle during tapping. The lid has an opening which allows the tapped melt flows from the runner into the ladle and the fumes can flow out of the ladle from the same opening. The specific property of the proposed design for the lid is to reduce the ladle free surface, where the fumes come in contact with air, as well as directing the ladle fumes towards the hood inlet. The geometry of the system in this situation and the lid structure has been shown in Figure 6.9.

Improved performance of the hood system using the described lid installed over the ladle for different working situations have been shown in Figures 6.27-6.31. As the results show directing the ladle fumes towards the hood inlet leads to a more efficient performance for the hood system. Adding the lid has no effect on the capability of the hood in capturing of tapping off-gases and it only affects the flows of ladle fumes in the tapping area.

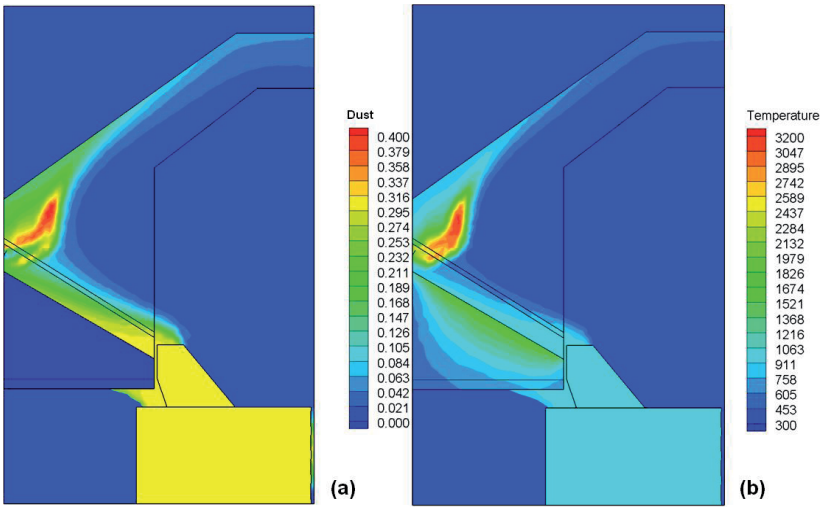

Figure 6.27: Mass fraction of dust (a) and temperature distribution in the hood channel (b) when the tapping gas velocity is 50 *m/s* and the suction rate provided by the furnace intake fan is 15000 Nm^3/hr.

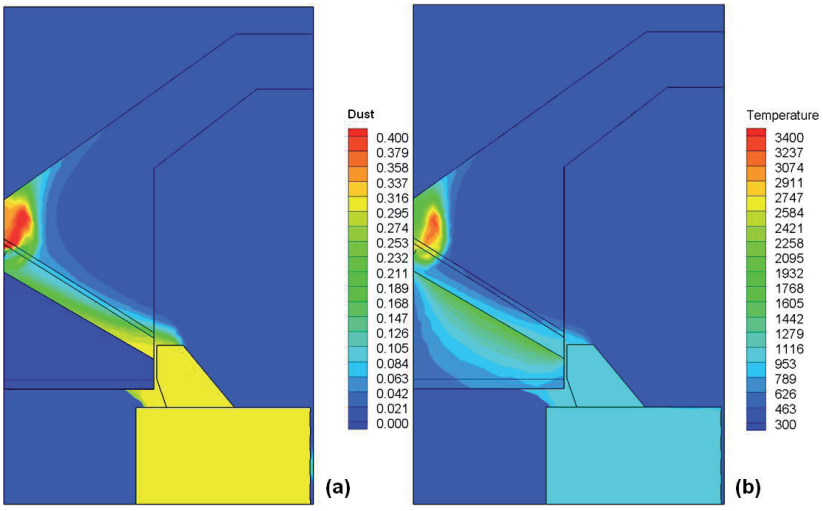

Figure 6.28: Mass fraction of dust (a) and temperature distribution in the hood channel (b) when the tapping gas velocity is 50 *m/s* and the suction rate provided by the furnace intake fan is 30000 Nm^3/hr.

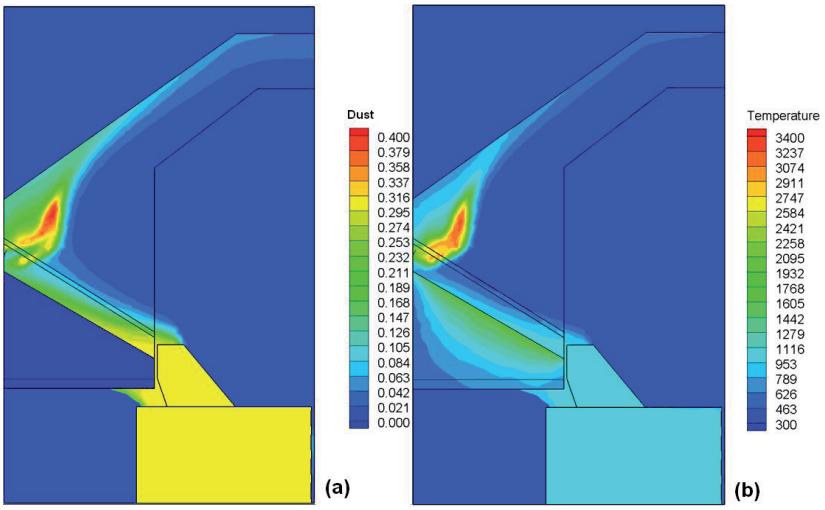

Figure 6.29: Mass fraction of dust (a) and temperature distribution in the hood channel (b) when the tapping gas velocity is 50 *m/s* and the suction rate provided by the furnace intake fan is 30000 Nm^3/hr.

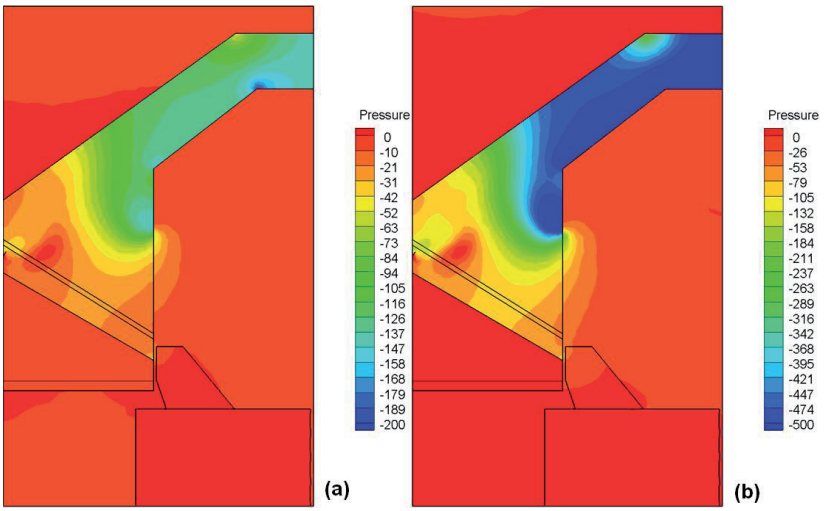

Figure 6.30: Pressure drop in the hood channel in the situation where the taphole gas velocity is 50 *m/s* and the fan suction rate is 15000 Nm^3/hr (a) and 30000 Nm^3/hr (b).

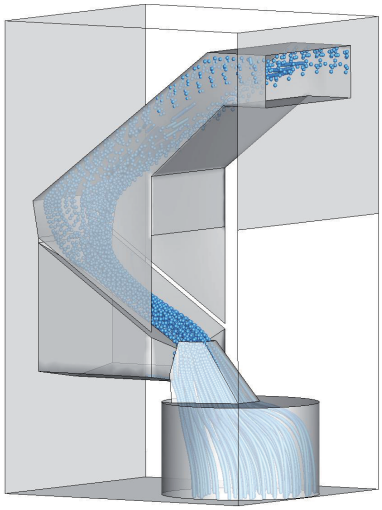

Figure 6.31: Pathlines of ladle fumes towards the hood in the situation when the tapping gas velocity is 50 *m/s* and the fan suction rate is 30000 Nm^3/hr.

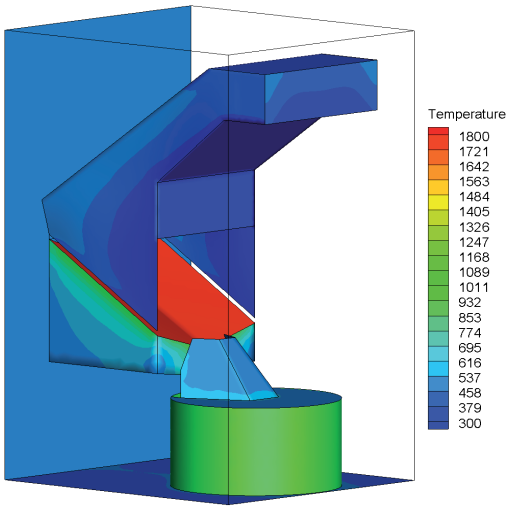

Figure 6.32: Contours of temperature distribution on the walls of the system in the situation where the taphole gas velocity is 100 *m/s* and the fan suction rate is 30000 Nm^3/hr.

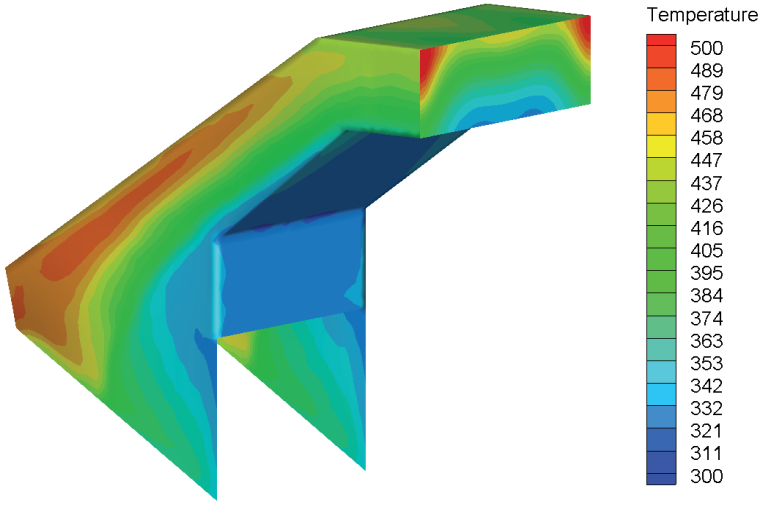

Figure 6.33: Temperature distribution in the channel body in the situation where the taphole gas velocity is 100 *m/s* and the fan suction rate is 30000 Nm^3/hr.

The results show that the hood system shows the best performance in the current situation where both ladle fumes and tapping off-gases are efficiently captured.

Practical results of the CFD model for the operation of the system in this situation are given in Table 6.6. The provided information by the modeling work is very useful in construction and operation of the system in the industrial scale.

Table 6.6: Results of the model for average temperature, velocity and dust concentration at the fan inlet during operation of the hood.

Case Study	Temp. (*K*)	Dust conc. (mg/Nm^3)	Velocity (*m/s*)	Efficiency (%)
V=50 *m/s* - S=15000 Nm^3/hr	412	1994	17.0	94.2
V=50 *m/s* - S=30000 Nm^3/hr	366	2258	30.3	97.5
V=100 *m/s* - S=30000 Nm^3/hr	403	2978	33.3	96.0

The general performance of the new hood system for different working conditions has been briefly presented in Table 6.7.

Table 6.7: General performance of the new hood system in different working conditions, $\surd$: Successful performance and X: Failed operation.

Parameter	$S = 5000Nm^3/hr$	$S = 10000Nm^3/hr$	$S = 15000Nm^3/hr$	$S = 30000Nm^3/hr$
$V = 10m/s$	$\surd$	$\surd$	$\surd$	$\surd$
$V = 50m/s$	X	X	$\surd$	$\surd$
$V = 100m/s$	X	X	$\surd$	$\surd$

6.4 Industrial tests

In order to validate the results of the model some industrial tests were done at Elkem Thamshavn and Elkem Salten plants where the hood system was installed on the silicon producing furnaces.

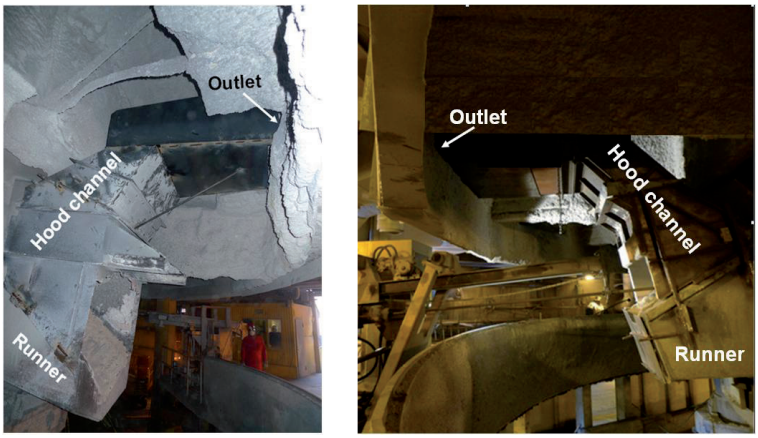

Figure 6.34: The hood system installed on the silicon furnaces at Elkem Salten plant (right) and Elkem Thamshavn plant (left).

Figure 6.34 shows how the hood structure has been installed on the silicon furnaces. The results of the experimental works are satisfactory and the new hood design shows very good performance in real operation.

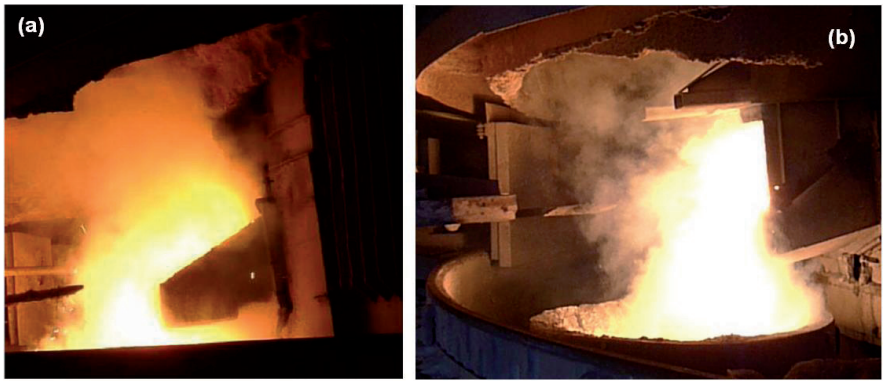

Figure 6.35: Release of dust in the tapping area before installing the hood system (a) and after installing the hood system (with some opening around the channel outlet) (b) on a silicon furnace.

Figure 6.36: Successful performance of the hood system using the lid over the ladle during tapping in a silicon furnace at Elkem Thamshavn plant.

The dust flows in the tapping area before installing the hood and after installing the hood system, of course with some opening around the channel outlet, have been shown in Figure 6.35. As it can be seen from this figure when the hood channel is not closed a portion of ladle fumes is released in the tapping area. It should be mentioned that the Figure 6.35 has been taken from the first industrial test of the

hood while the air gaps between the channel outlet and the fan inlet were quite larger than what has been considered in the modeling. That is why the hood efficiency in this figure seems to be somehow low.

The hood shows a perfect performance when the designed lid iused. Figure 6.36 represents how the ladle fumes and tapping gases are efficiently captured by the hood system in this situation.

Measuring the amount of dust in the off-channel proves that the hood system is able to capture the released pollution in the tapping area. The measurements are done using optical instrument NEO LaserDust MP which is able to measure both the gas velocity and gas temperature in the off-gas channel as well. LaserDust Monitors use a transmitter / receiver configuration to probe the dust concentration along the optical line-of-sight. The true non-contact approach (no probes) is superior to point type dust meters. The transmitter is similar for all three versions (MP, LP, XLP), whereas the receivers are of different size. With innovative laser technology the LaserDust combines two measurement principles in one instrument. At low dust levels it operates with forward scattered light technology: The incident laser light is scattered by dust particles and collected onto a solid-state sensor for dust quantification. This highly sensible mode enables detection limits of less than 0.5 mg/Nm^3 and is unaffected by dust depositing on the windows. At high dust levels the LaserDust will measure transmittance or opacity: Light absorption by dust particles is captured by a second sensor. The LaserDust equipment is shown in Figure 6.37.

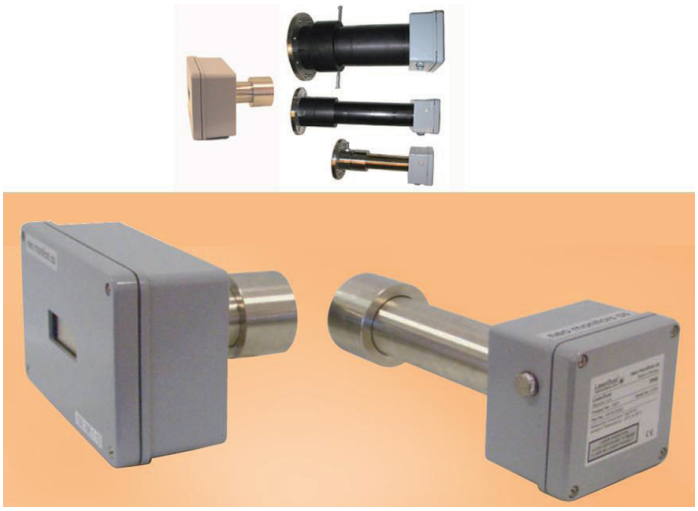

Figure 6.37: The NEO LaserDust MP used in measurements of dust in the furnace off-gas channel.

Figure 6.38 shows how the LaserDust system has been installed on the furnace off-gas channel during the measurements in the Elkem Salten plant.

Figure 6.38: The NEO LaserDust MP system installed on the off-gas channel of a silicon producing furnace at Elkem Salten plant. The industrial tests have been performed in April 2010 (Grådahl [2010]).

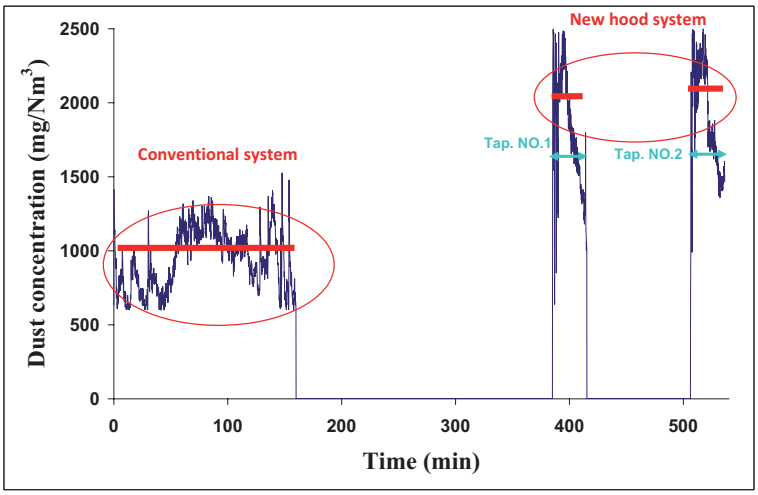

Figure 6.39: Comparison between the amount of dust in the off-gas channel during tapping in a silicon furnace at Elkem Salten plant before and after installing the hood system in April 2010 (Grådahl [2010]).

Comparison between the amount dust before and after installing the hood system is shown in Figure 6.39. It should be mentioned that this results comes from the hood performance while there were some opening around the channel outlet, without putting the lid over the ladle and in the normal tapping condition where there is no gassing from the taphole. The first part of the graph shows the measurements when the furnace is getting tapped continuously and of course without installing the new hood system. As it is seen the conventional ventilation system can capture a portion of the released dust from taphole off-gases and ladle fumes. After measuring the dust amount for a period of time, the tapping was stopped for installation of the hood. The measurements were then continued again to see the effect of the new hood design in capturing the dust. The furnace was tapped discontinuously after installing the hood and the measurements were performed for two different tapping operations. In the second part of the graph there are two peaks showing the measured dust amount during discontinuous furnace tapping. The amount of dust which has been captured by the hood is almost two times of the dust captured by the conventional ventilation system. This result clearly shows the improved performance of the ventilation system using the new hood design.

6.5 Conclusions

A physical design and theoretical model for capturing fumes from gassing taphole and ladle has been presented. The model is 3D and has been developed based on computational fluid dynamics. The model represents different aspects of the gassing phenomena such as combustion of off-gasses, temperature distribution, different heat transfer modes, and turbulent flows of off-gasses for different geometries and working situations. At same time it is also able to evaluate the capabilities of the new hood design in capturing the released pollution in the tapping area. The model results for different gassing modes shows that selection of the suitable suction rate for the furnace intake fan is important in order to capture the pollution from the taphole. The total suction rate needed for the successful operation of the hood system is smaller than the traditional designs. Normally the efficiency of the furnace off-gas system is affected by internal air flow around the furnace, driven by external wind which enter through open doors(Hall wind). Due to high suction rates created by this new hood design, the efficiency of this system is less affected by "Hall-Wind". In order to test the new hood system it has been installed on some silicon furnaces in the Elkem Company and it showed very good performance in the preliminary tests. The experimental tests in the plant are in good agreements with results generated by the model and hence it can prove the validity of the model.

Chapter 7

Modeling of Tapping Process in Ferromanganese (FeMn) Production Furnaces

FOR the stable operation of a submerged arc furnace, precise controlled tapping of the molten products is an important factor. In this chapter tapping of slag and metal from submerged arc furnaces used for ferromanganese production is investigated. An in-depth understanding of the melt flows and heat transfer in the furnace is essential in order to identify the governing conditions on the tapping process. Therefore a comprehensive Computational Fluid Dynamics (CFD) model of an industrial size furnace is described which is able to predict the melt flows in the furnace hearth, temperature distribution in the melt and the wall refractories and flow rates of slag and metal during tapping of the furnace. The model addresses multiphase fluid flow; conjugate heat transfer, natural convection, turbulent flow through porous beds inside the furnace and high resolution grid. Using the modified $k - \epsilon$ turbulence model for porous beds, the effect of fluid flows around coke particles is taken into account.

7.1 Tapping of slag and metal from packed bed reservoirs

As the result of furnace operation slag and metal are produced and they are accumulated over the furnace bottom. The molten products are then tapped from the

furnace in predefined time intervals. Stable operation of submerged arc furnace is required to reduce energy consumption in the furnace. Stability of furnace operation is highly dependent on the quality of tapping process. Tapping of melt from the furnace is directly connected to the conditions inside the furnace. To maintain the inside of the furnace in good condition, in addition to different operational issues, it is necessary to clarify the drainage behavior of molten metal and slag in the hearth. Therefore the melt flow behavior should be understood precisely.

In the furnace hearth, the molten metal and slag layers segregate into two separate layers due to density difference. The viscosities of the two layers are also largely different; the molten slag is usually several orders of magnitude more viscous. In submerged arc furnaces the hearth is often packed with coke particles, so that the liquids inside the hearth can only flow throughout the void space between the particles.

Flow of molten slag and metal in a FeMn furnace is very similar to melt flows in a blast furnace (BF) hearth (Ashrafian and Johansen [2006]). There are several studies available in the literature about flow of molten slag and metal in the blast furnace hearth. Throughout the pioneering experiments about tapping process in the blast furnaces (Fukutake and Okabe [1976]), it was shown that during the tapping period, the slag surface tilts towards the taphole resulting in an early discharge of the furnace gases and remaining of relatively large amounts of slag in the furnace. These observations were furthermore completed in other studies (Tanzil et al. [1984]) where it was observed that the slag-metal interface may also tilt towards the taphole. Simultaneous to the tapping of the overlaying slag layer, the metal layer is also entrained into the taphole from levels well below the taphole level. Different flow regimes in tapping of the slag and metal from the blast furnace hearth are schematically shown in Figure 7.1.

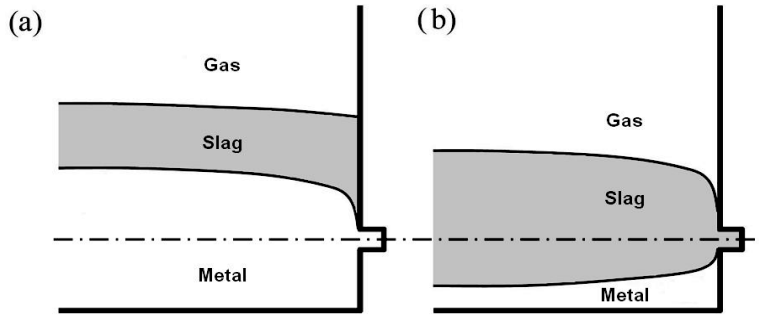

Figure 7.1: Different flow regimes in tapping of stratified fluids from a packed bed reservoir while the metal height is above (a) or bellow (b) the taphole level.

In fluid mechanics, the entrainment of immiscible liquids during the tapping of one or the other is a well-known phenomenon. In many applications, it is necessary to predict the maximum rate of withdrawal of a fluid with desired properties which can be attained before fluid from a different level also begins to flow (Turner [1973]). The behavior of fluid flow in the channels due to existence of point and line sinks in the end wall of channel at different levels from the interface between the two layers have been investigated in previous works (Craya [1949] and Huber [1960]). Further improvements of the theory of the withdrawal from a two-layer fluid through a line sink were carried out through works done by Hocking and Forbes [2001], Tyvand [1992] and Stokes et al. [2003].

In the case of tapping from a ferromanganese furnace, existence of metal, slag and gas as three separate phases in the system, interaction of different phases with a packed bed of solid particles in the slag and coke bed zones and unknown shape for the coke bed, are just examples which show how complex the system is. Drainage rates as well as the viscosity of the working liquids are often quite high. The complex flow behavior through the furnace hearth is, therefore a result of the simultaneous action of inertial, buoyancy and viscous forces, including the geometrical effects represented by the packed bed.

Tapping of slag and metal from the FeMn furnaces could be idealized as the drainage of immiscible liquids from a packed bed reservoir. This problem was revisited by Ashrafian and Johansen [2006] through developing a simple two-dimensional CFD model. Their model includes a non-porous metal zone and porous slag and gas zones, where the porosity and particles size are evenly distributed in these zones. The aim of their work was to study the behavior of metal and slag flows while tapping from a packed bed reservoir as the furnace hearth. The influence of density

and viscosity ratios of slag and metals as well as the packed bed characteristics on the onset of entrainment of slag into the taphole was studied in their work. They found that buoyancy effects are the underlying parameter in determining the onset of the simultaneous tapping. Also they concluded that in the absence of packed bed, the viscosity ratio was found out to have no influence on the tapping behavior while with the presence of the packed-bed the tapping behavior is drastically changed. Their results show that onset of entrainment of slag as well as the gas-slag interface into the taphole is advanced, leading to the considerable amounts of the lighter liquid to be remained in the reservoir. The initial situation and tilted gas-slag and slag-metal towards the furnace taphole as the result of their 2D model is presented in Figure 7.2.

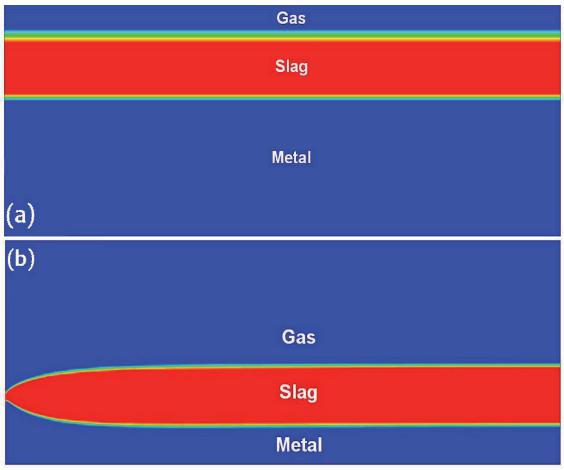

Figure 7.2: Initial flat interfaces (a) and tilted interfaces between gas, slag and metal towards the taphole, due to tapping, (b) in a packed of solid particles as the result of a 2D CFD model for tapping of stratified liquids from a packed bed reservoir as a furnace (Ashrafian and Johansen [2006]).

7.2 Modeling the tapping in FeMn furnaces

In spite of the investigations described above, a general description of the flow behavior during the tapping of slag and metal from the submerged arc furnaces is difficult to obtain, due to the complexity of the real system and simplifications and assumptions made in the numerical models. The current study aims to develop a

new three-dimensional numerical model to resolve the complex flow structures and heat transfer within the hearth of a FeMn furnace. Therefore our model is restricted to the lower part of the furnace. The current model is built based on an industrial size furnace and uses multiphase Computational Fluid Dynamics (CFD) techniques together with refined computational grid and applies a set of mathematical equations for turbulent flow-heat transfer in porous media. Moreover, the flow pattern and heat transfer are described and analyzed in more details to extend the knowledge on the liquid slag and metal flows. Physical properties of coke bed zone such as porosity, permeability and particles size as well as the most probable coke bed structure have been selected based on both the available literature and industrial information about the conditions inside the furnace.

7.2.1 Geometry of the Model

Since the current research aims to investigate the tapping of slag and metal from a FeMn furnace, the model is restricted to the lower part of the furnace including metal layer and the coke bed. Therefore only 1 m from the furnace bottom is considered in the geometry of the model. It addition the geometry includes the furnace refractory walls, both side wall and bottom wall, in order to study the heat distribution in the lower part of the furnace. The furnace geometry has been selected based on an industrial size FeMn furnace with following specifications. 2D side view of the furnace geometry is shown in Figure 7.3.

Table 7.1: Detailed geometry of the FeMn production furnace used in CFD modeling

Furnace diameter (m)	Considered height (m)	Electrode diameter (m)	Taphole diameter (m)	Taphole length (m)	Taphole height (m)
11	1	2	0.10	0.6	0.4

The high temperature zone of the furnace is treated as symmetric about the plane defined by the hearth centerline and the taphole, so only one half of the furnace needs to be modeled. The furnace geometry including different zones is shown in Figure 7.4.

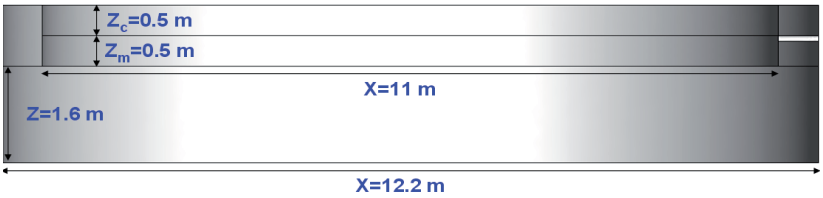

Figure 7.3: 2D side view of the geometry of the FeMn furnace considered for CFD modeling in this research (thickness of metal and coke bed layers in this case are 0.5 m).

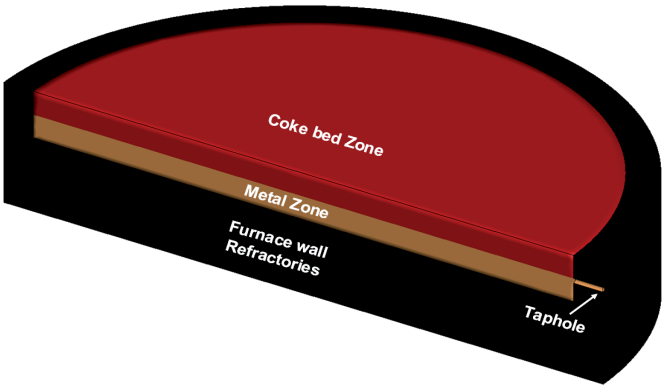

Figure 7.4: Geometry of the FeMn production furnace including the slag and metal zones as well as wall refractories.

Table 7.2: Physical properties of different zones used in CFD modeling of the FeMn production furnace (Olsen et al. [2007], Shin et al. [2010] and Eramet [2010])

Zone	Fluid density (kg/m^3)	Dynamic viscosity $(Pa.s)$	Thermal conductivity $(W.m^{-1}.K^{-1})$	Packed porosity	Specific heat $(J.kg^{-1}.K^{-1})$	Particles diameter (m)
Metal	6100	0.005	40	1	791	-
Coarse coke bed	3000	0.1	3	0.3	1800	0.05
Fine coke bed	3000	0.1	3	0.5	1800	0.015

The coke bed zone is divided into two different zones called fine coke bed, the zones located under the electrodes, and coarse coke bed which includes the rest of

coke bed zone (see Figure 7.5). Physical properties of the described zones, slag and metal are given in Table 7.2. Surface tension for the metal is equal to 1.17 N/m Shin et al., for the slag is 0.5 N/m and metal - slag interfacial tension is equal to 0.6 N/m Ashrafian and Johansen [2006].

The furnace wall refractory thickness is considered 1.6 *m* at the bottom and 0.6 *m* at the furnace side wall. It was assumed that the wall refractory is made of normal carbon bricks used in constructing submerged arc furnaces (Scheepers [2008]) and therefore the material properties of the bricks were chosen upon to the available information.

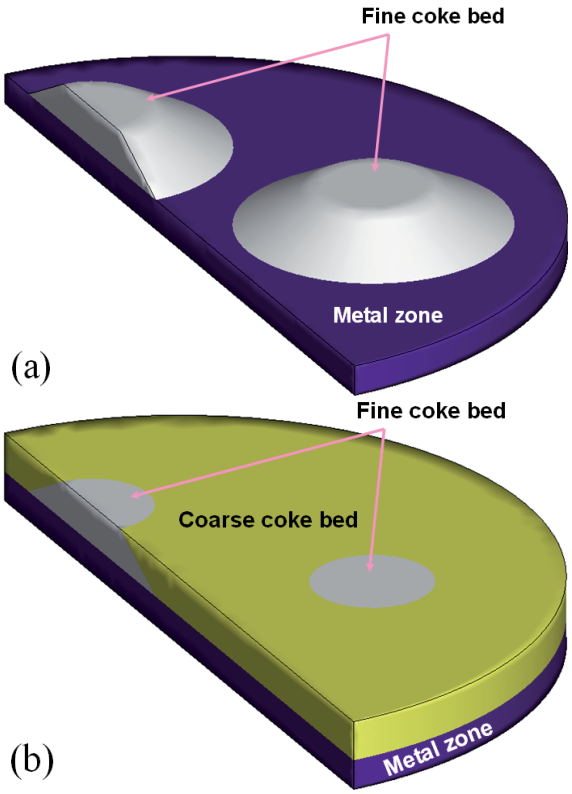

Figure 7.5: Coke bed zone laid over the metal layer in the furnace hearth, the fine coke bed(a) and the coarse coke bed (b).

7.2.2 Model governing equations

Metal, slag and gas are the immiscible phases available in the model of the FeMn producing furnace. The interfaces between these phases are tracked by VOF method. The conservation equations for mass and momentum in isotropic porous medium, resistance against fluid flows and turbulence model's equations used in this model have been described earlier through Equations (5.1) - (5.10).

Using the proper turbulence model for porous media (Kuwahara and Nakayama [1999]), the effect of microscopic flows around coke particles in the coke bed zone is considered into account and it allows unified treatment of coke bed and metal zone. Assuming thermal equilibrium between the fluid and solid matrix of packed bed, for saturated rigid porous media, the energy equations for the fluid and solid phases have been extracted by Guo et al. [2008]. The same equations have been applied in the current research.

7.2.3 Numerical method and boundary conditions

The numerical computations were performed with the commercial CFD package FLUENT 6.3.26 which is a finite volume based software. To construct liquid-liquid and gas-liquid interfaces in the system, Volume Of Fluid (VOF) method together with the CICSAM scheme, suitable for fluids with big viscosity difference, was chosen. The software provides a solver for a standard set of Navier-Stokes equations for fluid flow and heat transfer. The additional source terms for the modified turbulence and heat transfer model are introduced using user defined functions (UDF's) to the software. The mesh generated for the model is arranged in such a way that the resolution is high in regions where velocities or temperature tends to vary greatly, e.g., near taphole and in the radial direction. The total number of grid points is about 600 000.

For boundary conditions it is assumed that both the slag and metal production happen in the fine coke bed zone. Based on industrial data an average production rate of 200 *ton/day* for slag and 330 *ton/day* for metal, have been considered as the mass source terms in the model. Pressure on the taphole surface is set as the atmospheric pressure condition. On the slag surface, a constant pressure, 150 *mbar*, and temperature of 1450°C were specified. The pressure term is considered to account the effect of charge weight on the slag and hence metal zones. At the wall, a no-slip condition exists on the hot face of the refractory walls. The standard log law wall function is applied for the velocity. The thermal boundary layer is modeled using the thermal law-of-the-wall function. Temperatures at the cold face of the refractory

and the furnace bottom are explicitly specified. The upper surface of the refractory wall is adiabatic. The computational grid developed for CFD modeling is presented in Figure 7.6.

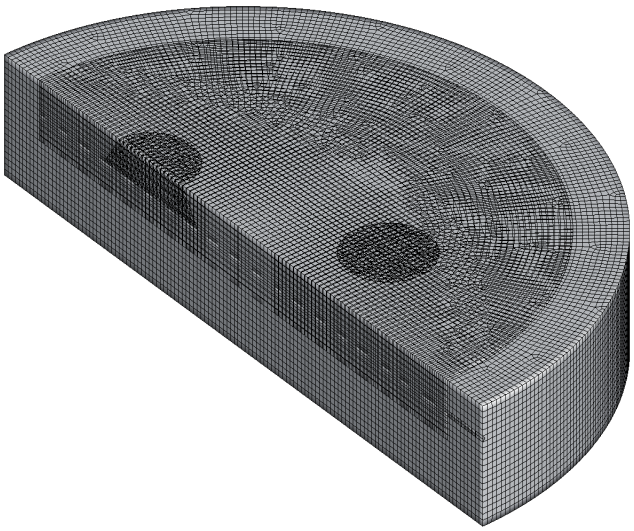

Figure 7.6: Computational grid of the FeMn furnace geometry including the high temperature zone of the furnace and the wall refractory.

7.2.4 Results and discussions

The results of the model are divided into two different parts. In the first part, general features of the slag and metal flows and heat transfer in the furnace hearth are discussed. The effect of the slag and metal height on the tapping flow rate from the furnace is then investigated in the second part. Finally comparison between the model results and operational data from an industrial furnace with the same size as the model, is presented. It should be mentioned that in all case studies, the initial fluids in the system are slag and metal. As the tapping process proceeds the zones which are emptied of slag are filled with process gas with a density of 0.23 kg/m^3 in the furnace working temperature, and hence the third phase appears in the model.

Melt flows in the furnace hearth

The predicted results show there are two different flow zones in the furnace, which can be separated by the interfacial boundary between the slag and metal layers. the

fluid velocity in the metal layer is always more than that in the slag layer. Resistance created by the low permeable coke bed zone against the high viscosity slag flow is the main reason for low fluid velocity in the coke bed zone.

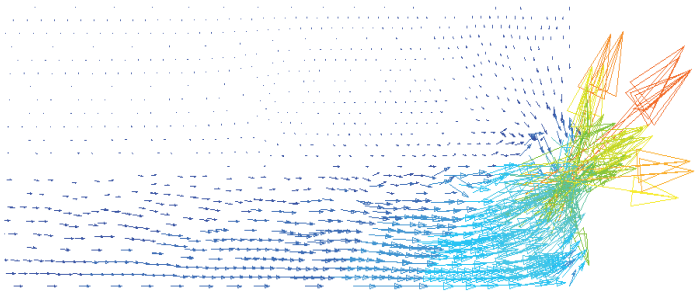

Figure 7.7: Velocity vectors in the central vertical plane of the furnace, y=0, showing higher velocity magnitude in the metal layer comparing with flow of highly viscous slag in the coke bed zone.

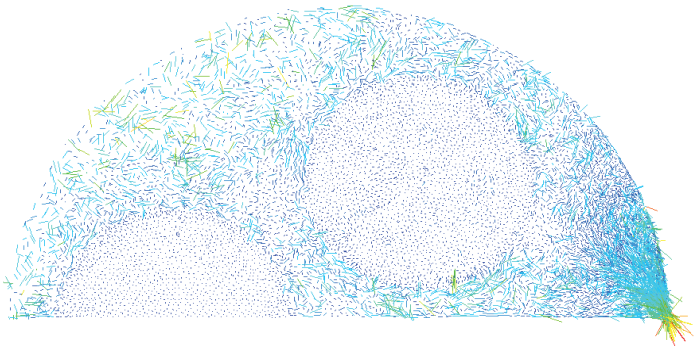

Figure 7.8: Velocity vectors in the central horizontal plane of the furnace, z=0.5 *m*, showing higher velocity magnitude for the slag in the coarse coke bed zone comparing to the slag flow in the fine coke bed zone.

Figure 7.7 shows the velocity vectors in the slag and metal layers for the vertical central plane of the furnace.

The slag velocity magnitude also varies between the fine coke bed and coarse coke bed zones. Reduced size of coke particles in the fine coke bed zone leads to formation of a less permeable region and hence higher resistance against fluid flow in this zone. This phenomenon is shown in Figure 7.8.

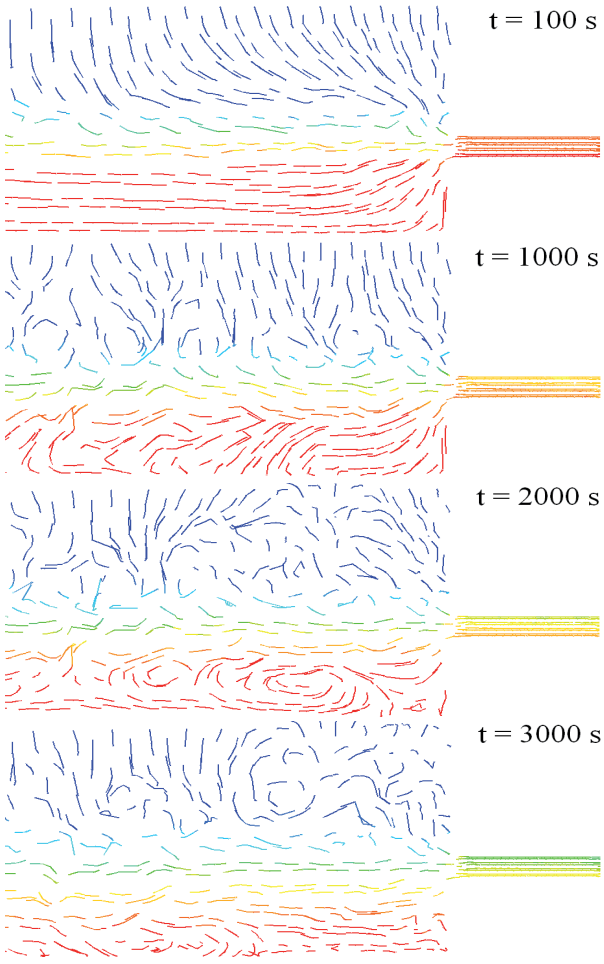

Figure 7.9: Evolution of the pathlines of the slag and metal flows in the high temperature zone of the furnace in vicinity of the taphole colored by volume fraction of metal.

The metal flows towards the furnace taphole even when the metal height is bellow the taphole level. Evolution of the slag and metal flows towards the taphole is shown in Figure 7.9.

As it can be seen from this figure, by start of tapping the direction in the metal zone is towards the furnace taphole, even in the zone close to the furnace bottom, and metal is the only phase which goes through taphole. As the tapping proceeds

the metal flow towards the taphole is disturbed due to flow of slag phase in the same direction and also decreased metal height. By time passing the metal flow is restructured through formation of recirculation loops in the zone close to the furnace bottom. In this situation the metal flow rate from the taphole decreases and slag is the main phase which occupies the taphole. At the final stage the gas phase also entrains towards the taphole while the slag height in the furnace is still above the taphole level. In this situation the tapping rate of both the slag and metal from the furnace taphole drops. Figure 7.10 shows the situation where the slag and metal are getting tapped from the furnace and the gas phase has entrained the melt flows.

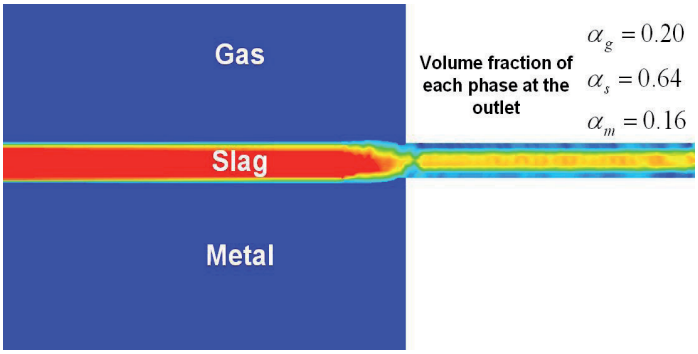

Figure 7.10: Volume fraction of different phases, in vicinity of furnace taphole, in the FeMn furnace during tapping showing simultaneous flow of metal and slag through the taphole while the gas phase has entrained the melt flows.

Temperature distribution in the furnace hearth

The melt flow pattern determines the temperature distribution in the liquid phases. High efficiency heat transfer is made by the bulk flow advection, turbulent diffusion and thermal dispersion, which strongly depend upon the fluid velocity. Temperature distribution in the slag and metal as well as furnace wall refractory is shown in Figures 7.11 and 7.12. Results of the model considering the melt flows in the furnace hearth, Figure 7.11, show that the temperature is basically uniform over a large portion of the melt pool, while the change in temperature is mostly restricted to the near-wall regions or those corner regions of the refractoryhot metal interface. As it can be seen from this figure the metal temperature in the furnace and close to the taphole zone is higher than the opposite side in vicinity of the furnace wall. This is in one hand due to high thermal conductivity of molten metal which leads to

higher heat transfer from hot metal to the cold wall refractory. In the other hand it is caused because of low melt velocity in this zone and hence decreased heat transfer efficiency due to bulk flow advection and turbulent diffusion. This phenomenon is not seen in the coke bed zone due to very low thermal conductivity of molten slag which flows in this zone.

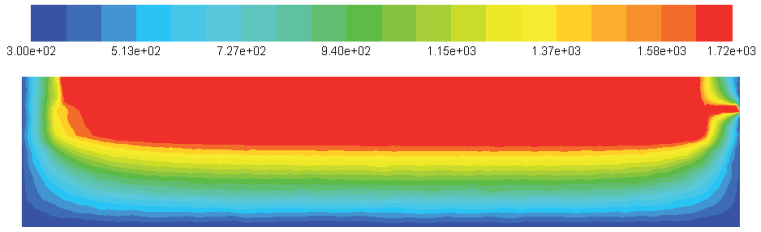

Figure 7.11: Temperature distribution in the high temperature melt zone of the furnace as well as wall refractory in the central vertical plane of the furnace.

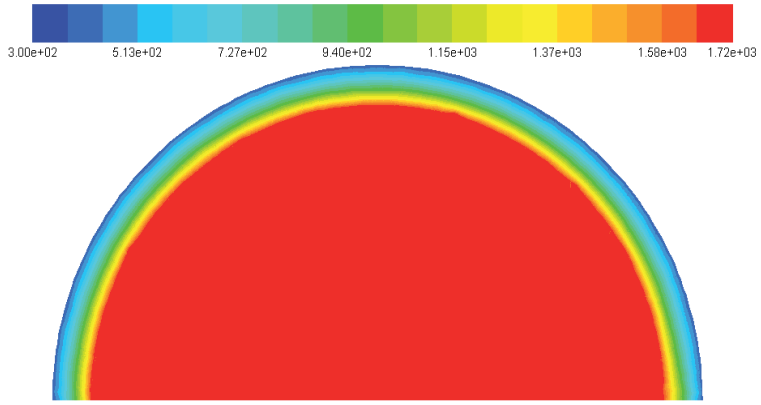

Figure 7.12: Temperature distribution in the high temperature melt zone of the furnace as well as wall refractory in the horizontal plane located over the slag surface.

The temperature profile along the vertical centreline of the furnace is shown in Figure 7.13. In the solid refractory region, between $z = 0$ and $z = 1.6m$, the temperature gradient is inversely proportional to the thermal conductivity of the construction material. Overall, the thermal conduction across the solid refractory dominates the entire heat transfer from hot melts to the surrounding.

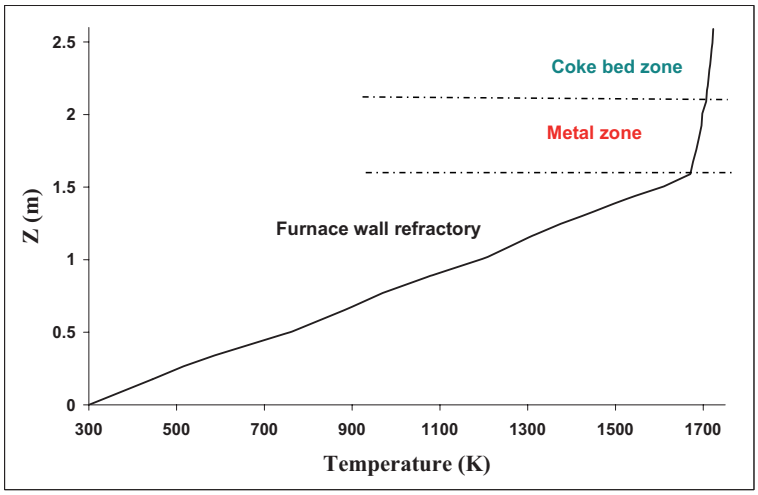

Figure 7.13: Temperature profile along the vertical centerline of the furnace, $x = 5.5m$, showing the temperature gradients in both wall refractory and molten phases.

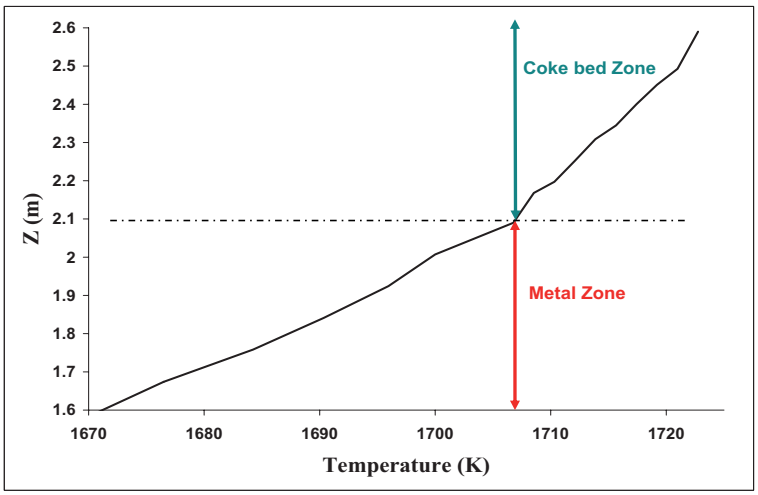

Figure 7.14: Temperature profile along the vertical centerline of the furnace, $x = 5.5m$, showing the temperature gradients only inside the molten phases.

Figure 7.14 represents the same temperature profile when it is only restricted to the metal and coke bed zones. As it is seen from this figure there is a linear

temperature gradient in the metal zone while a change in the slope of this linear gradient at the slag - metal interface, approximately at $z = 2.1m$, is clear. It is also seen that there is a linear temperature gradient in the coke bed zone.

This result show that there is a distinct temperature difference between slag and metal phases which can be used to make distinguish between these phases in the situation where slag and metal are simultaneously tapped from FeMn furnaces.

The temperature profile in the slag and metal phases along the horizontal centerline of the furnace is presented in Figures 7.15 and 7.16.

The temperature profile in the metal zone shows that there is a temperature gradient while moving in the vertical direction in this zone. In fact due to higher temperature in the slag, the metal temperature increases as the vertical distance to the slag-metal interface decreases. There is also a temperature gradient in the horizontal direction showing that the metal temperature close to the taphole region is higher than the opposite side in the furnace.

In the coke bed zone where slag exists, the melt temperature is mostly constants along the horizontal centerline and there is rapid changes in the temperature close to the wall refractory. It is also clear that close to the wall refractory, the melt temperature in the taphole region is higher than the opposite side in the furnace.

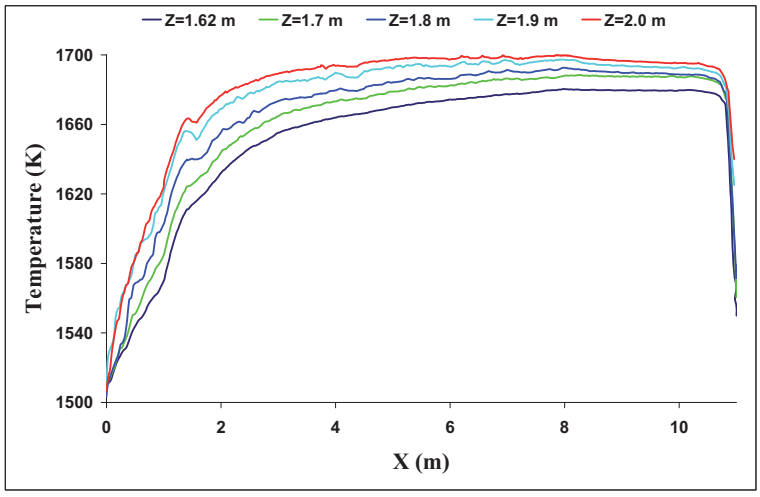

Figure 7.15: Temperature profile along the horizontal centerline of the furnace, parallel to the furnace bottom, showing the temperature gradients in the metal zone.

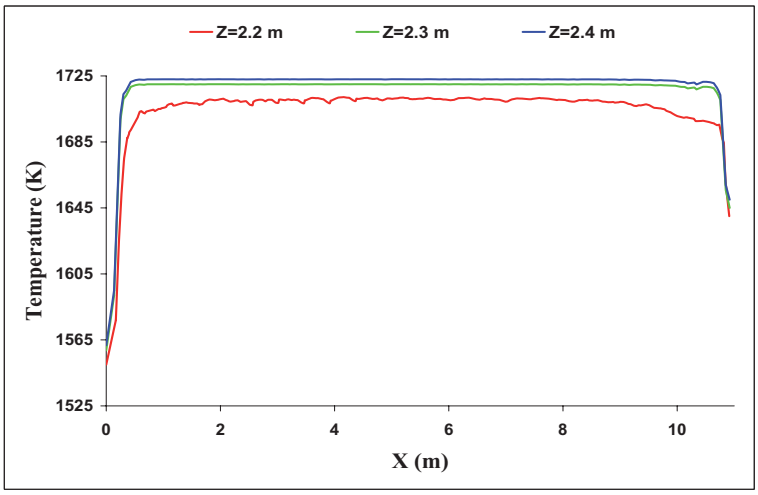

Figure 7.16: Temperature profile along the horizontal centerline of the furnace, parallel to the furnace bottom, showing the temperature gradients in the slag.

Effect of buoyancy on the melt temperature profile

In the presented results the fluid density change due to thermal expansion, buoyancy effect, has been ignored in the model. Considering the buoyancy effect in the melt leads to a changed temperature profile in the furnace. Figure 7.17 shows comparison between temperature profile along the vertical centreline of the furnace with and without considering the buoyancy effect. The effect of buoyancy on the temperature profile is more clear when it is restricted to the zone including the melts (see Figure 7.18).

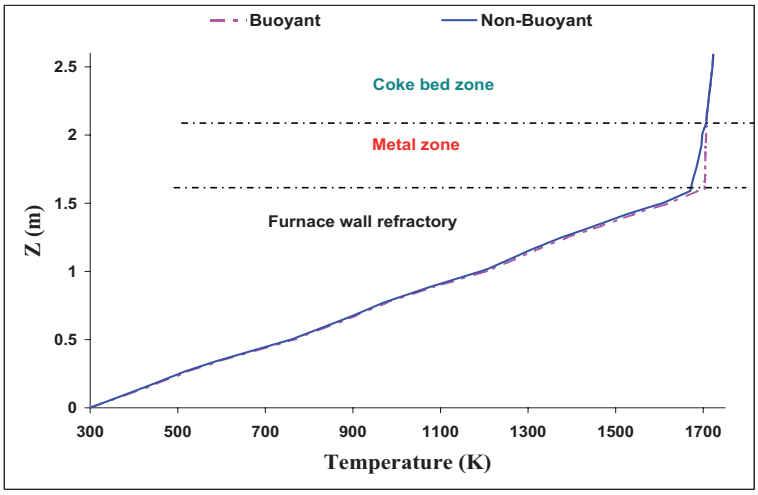

Figure 7.17: Comparison between the temperature profile along the vertical centerline of the furnace, $x = 5.5m$, in two situations with and without considering the buoyancy effect in the melt.

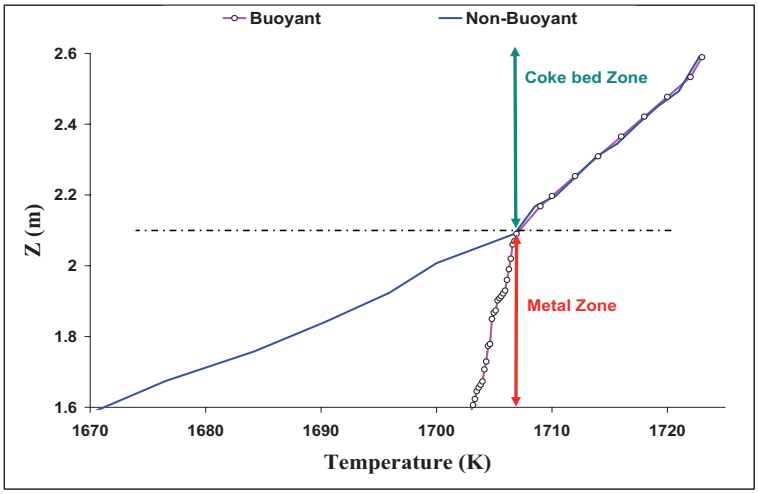

Figure 7.18: Comparison between the buoyant and non-buoyant temperature profiles along the vertical centerline of the furnace, $x = 5.5m$, in the zone where molten phases do exist.

From these figures it is seen that in the case where no buoyancy is considered,

temperature changes significantly in the metal layer, whereas it is not the case when the buoyancy is included. It is also seen that the buoyancy force is negligible for the case of a liquid with a low thermal expansion coefficient, such as slag. In this case, the turbulence/dispersion makes very little difference to the calculated result. However, the contribution of turbulence/dispersion has been found to be much stronger when a stagnant zone due to natural convection exists. Presence of coke particles would generate additional turbulence and thermal dispersion compared with the metal layer where there is no particle in it.

Investigation of the effect of slag and metal height on the tapping parameters

One of the main parameters which can influence tapping of slag and metal from FeMn furnaces, is the volume of the melts inside the furnace hearth. The initial levels of molten products in the furnace hearth in one hand determines the hydrostatic pressure in the furnace as a driving force for tapping of the melts. In the other hand it influences the composition of slag and metal in the tapped melts. In the current research the effect of slag and metal height on the tapping flow rate from the described size FeMn furnace is investigated. The case studies which have been considered in this research are listed in Table 7.3.

Table 7.3: List of the case studies which have been investigated in the current research

H \ Case No.	Case No.1	Case No.2	Case No.3	Case No.4
Metal Height (m)	0.4	0.5	0.6	0.7
Slag Height (m)	0.6	0.5	0.4	0.3

During tapping, the metal height in the furnace gradually decreases and therefore the coke bed zone which is floating on the metal layer, will descend as well. In order to consider the vertical movement of porous coke bed, several zones in form of layers located on top of each other have been considered in the model. The physical properties of each layer changes from non-porous to a porous zone as it is filled with slag. Since modeling of a moving porous bed in Fluent is difficult and because this method is applied only to a very narrow region at the slag-metal interface, it seems that this simplification does not affect the accuracy of the model significantly.

Tapping flow rate from the FeMn furnace in the case where the slag and metal heights are equal to $0.5m$ is shown in Figure 7.19. It is seen from this figure that

metal flow rate is quite high by the start of tapping and it decreases to a constant level as tapping proceeds. The slag has a much less tapping rate, comparing to metal, at the beginning but it slowly increases to a higher and constant amount and finally it decreases to a lower rate again. The resultant total flow rate from the furnace shows a decreasing behavior.

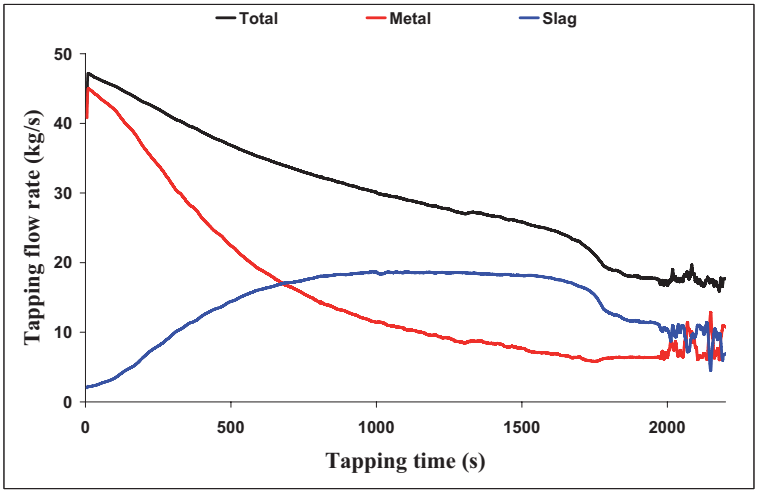

Figure 7.19: Tapping flow rate from the FeMn furnace in the situation where the slag and metal heights are both equal to $0.5m$.

The tapping weight for this case is shown in Figure 7.20. The result show that the metal weight increases with a faster rate at the beginning and it reaches to a more flat level as the metal tapping rate decreases. The slag tapping weight shows an increasing behavior up to the time when its tapping rate drops to a much lower level and after that it has a much slower increase rate. The total tapping weight follows a pattern very similar to the metal weight.

The tapping rate of metal for different case studies is presented in Figure 7.21. The results show that the flow rate of metal which is tapped from the furnace is directly related to the initial metal height. As tapping continues, the tapping flow rate decreases to a level which is almost constant in all case studies. Evolution in the total weight of the metal which is tapped from the furnace is shown in Figure 7.22.

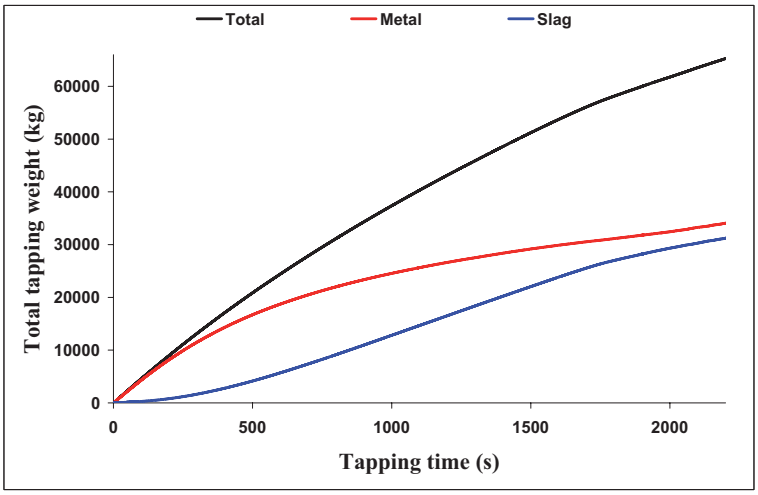

Figure 7.20: Tapping weight from the FeMn furnace in the situation where the slag and metal heights are both equal to $0.5m$.

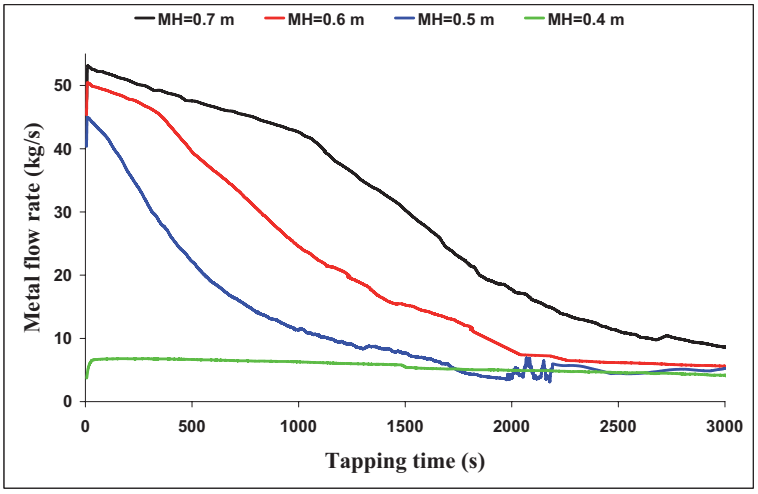

Figure 7.21: Metal flow rate during tapping of the FeMn furnace in the situation where the metal heights ranges from $0.4m$ - $0.7m$.

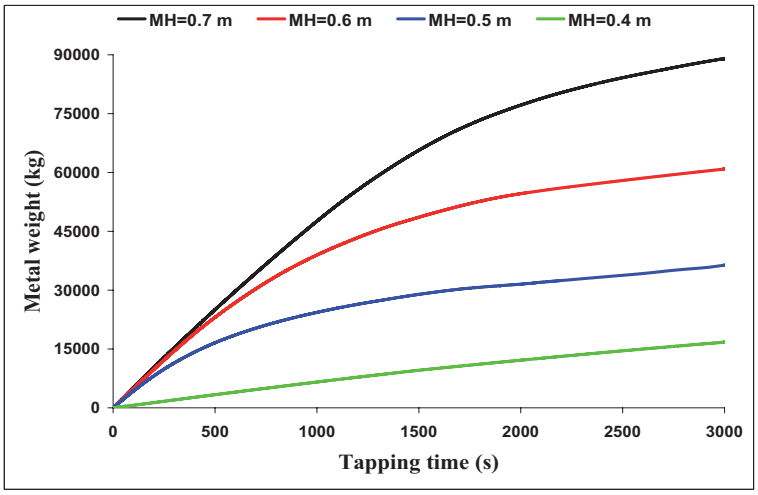

Figure 7.22: Metal weight increase during tapping of the FeMn furnace in the situation where the metal heights ranges from $0.4m$ - $0.7m$.

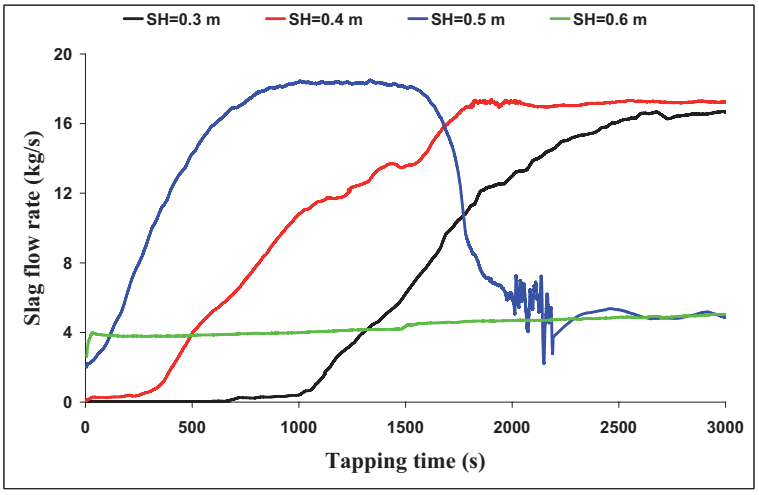

Figure 7.23: Slag flow rate during tapping of the FeMn furnace in the situation where the slag heights ranges from $0.3m$ - $0.6m$.

The slag flow rate as a function of tapping time is presented in Figure 7.23. The most interesting result is that the slag height is detrimental parameter for tapping

flow rate of slag only if the metal height is above the taphole level. In this situation the higher the slag height the higher the tapping flow rate of slag, although the flow rate difference is not significant. In the situation where the metal height is lower than the taphole level, $MH = 0.4m$, the slag height is highest among the case studies but the slag flow rate is the lowest.

The main reason for this phenomenon is that the metal flow through the furnace taphole acts as a driving force to evacuate the overlaying high viscosity slag when the slag reaches to the taphole.

Comparing the results of model with industrial measurements

In order to check validity of the predicted results by the model, using of industrial measurements is an essential step. Continuous measurement of tapping weight from a FeMn furnace, due to some technical problems, was not possible to be performed. However the industrial data from operation of a FeMn furnace with the same size as the model was provided by one of the industrial partner of the project (Eramet Norway).

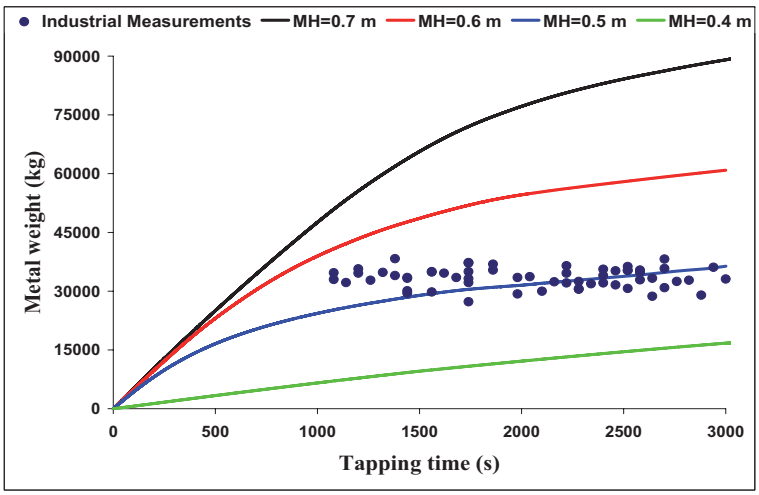

Figure 7.24: Comparison between the results provided by the model and industrial data from one week operation of the same furnace size as the model.

These data have been taken from one week of normal furnace operation. The results are the weight of tapped metal and not slag because the weight of produced

metal is the data which is normally registered in the plant during furnace operation. The points represent the industrial measurement of the metal weight after tapping. Comparison between the model results and industrial measurements is shown in Figure 7.24.

This comparison shows that the model covers the industrial data in its range. The main result is that the model predicts a metal height of $0.5m \mp 0.05m$ inside the furnace. Considering the fact that taphole level is at $z = 0.45m$, the model prediction shows that the metal height in the furnace just before the start of tapping is always above the taphole level.

7.3 Conclusions

The tapping process in ferromanganese (FeMn) production furnaces was investigated. A 3D multiphase model for the high temperature zone of the furnace was developed. The furnace geometry was taken from an industrial size FeMn furnace. The developed model is based on Computational Fluid Dynamics (CFD) techniques and it considers slag and metal flows and heat transfer in the furnace hearth. The model shows that there is a distinct temperature difference between molten slag and metal inside the furnace. Also the metal temperatures in the different regions over the furnace bottom are different. The temperature in the slag zone is evenly distributed except for a narrow region at the slag-metal interface where the slag temperature is influenced by metal. The tapping flow rate for different phases including slag and metal was predicted by the model for a number of different cases. The results indicate that since the permeability of the coke bed is low, the metal below the taphole level is able to drain during the tapping process. Decreased coke bed permeability can make this phenomenon more significant. Comparison between the model predictions and industrial tests can be used to estimate the true metal height inside a furnace.

Chapter 8

Conclusions and Recommendations for Future Work

In this work the tapping process in silicon and ferrosilicon production furnaces, designing a new hood system for capturing of tapping off-gases and ladle fumes and the tapping process in ferromanganese furnaces have been extensively studied. Investigations of each one of the mentioned topics has been performed using both modeling techniques and industrial tests. The results of the work as well as recommendation for the future work are briefly summarized as follows:

8.1 Tapping process in silicon and ferrosilicon furnaces

- A 3D multiphase CFD model of the furnaces based on industrial geometry and the most probable conditions of the inside of the furnaces has been developed. Using the model the effect of different parameters on the tapping speed has been studied.
- Different industrial tests have been performed within this work. Results of the industrial tests have been used both as input for developing the model and as scale for checking the validity of the theoretical work. There is a very good agreement between the model's predictions and the results of industrial tests which shows the validity of the model.
- The results show that tapping speed is highly depended on the magnitude of furnace crater pressure. Metal height also influences the tapping speed to

some extent but it is mostly important in determining the duration of tapping. Permeability of the furnace bottom bed affects the tapping speed, however it does not play an important role when the furnace crater pressure is high.

- The model predicts a narrow range for the average initial metal height in the furnace. It can also can predict variation in the furnace crater pressure which has been observed and reported as dynamic behavior of crater pressure during industrial measurements.

- The flow pattern of the silicon and ferrosilicon melts inside the furnace due to high gas pressure in the furnace crater zone, is one of the interesting results of the model. The melt flow pattern explains that why during tapping process the tapping flow rate drops suddenly from a high level down to a very low level. Although there is an evidence proving the obtained flow pattern in the furnace, however performing more industrial tests to check it more accurately is recommended.

- Flows of process gases in the charge materials have been predicted by the model which shows why the gas channels are created around the crater wall. However considering the gas solid reactions, mainly in the upper charge, is recommended in order to determine the positions where the condensation reaction happens. It will then be helpful in better understanding of crust formation in the charge and it's effect on the gas flows from crater zone towards the furnace top.

8.2 Designing a new hood system for collecting taphole off-gases and ladle fumes

- Taphole gassing phenomenon as an industrial challenge during tapping process in the silicon and ferrosilicon furnaces has been addressed. Design and construction of a new hood system for capturing of taphole off-gases from the furnaces has been done as a part of this research. CFD modeling has been used for feasibility study of the new design. Using the model performance of the hood system in different situations, considering a wide range for the tapping gas velocities and suction capacity, has been investigated.

- The new hood design has been industrially tested in different plants and it has shown a successful performance. The good agreement between the model

predictions and the results of industrial tests shows validity of the theoretical model.

- The main feature of the new design is that the hood shows a much better performance compared to conventional ventilation systems even with lower suction capacities. This is mainly because of the innovation in designing the hood channel. Due to suction of high amount of air into the channel, temperature distribution in the channel walls remains in a reasonable range and can not be a challenge during operation of the hood.

- Although the new hood system has originally been designed for capturing of taphole off-gasses, however both theoretical modeling and industrial tests show that it can also capture ladle fumes. Since the ladle fumes are a source of pollution in the tapping area, the hood performance can improve the working environment significantly.

8.3 Tapping process in ferromanganese furnaces

- In order to study the tapping process in ferromanganese furnaces, a 3D multi-phase model of high temperature zone of a ferromanganese furnace has been developed. Geometry of the model has been chosen based on an industrial size furnace and the conditions of inside the furnace have been modeled based on the most probable situation found from literature or industrial data. The model focuses on the melt flows in the furnace during the tapping process as well as temperature distribution in the melts and the furnace refractory walls.

- Comparison between the model's prediction and industrial data on the tapping weight of metal results in finding a range for the metal height in the furnace although there is no industrial measurement of the metal height in the furnace for further comparison.

- The results of model show that there is a distinct temperature difference between slag and metal in the furnace. It means that it may be possible to estimate volume flow rate of slag and metal during tapping through temperature control in the melts stream.

- Continuous measurement of tapping weight and the height of melts in a ladle during tapping of a ferromanganese furnace is helpful in determining the slag

and metal flow rates. Since it was not possible to do it in the current research, it is recommended to be done in the future works.

Bibliography

B. Andresen. *Process model for carbothermic production of silicon metal*. Dr.-ing thesis, MI-Report 1995:34, NTH, Norway.

A. Ashrafian and S. T. Johansen. Tapping of stratified liquids from a packed bed. In *5^{th} International Conference on CFD in the Process Industries*, pages 1–6, December 2006.

N. A. Barcza, A. Koursaris, J. B. See, and W. A. Gericke. The dig-out of a 75 mva high carbon ferromanganese electric smelting furnace. In *Proceedings of the 37^{th} Electric Furnace Conference, INFACON IX*, pages 19–33, December 1979.

P. Cheng. Two-dimensional radiating gas flow by a moment method. *AIAA Journal*, 2:1662–1664, 1964.

A. Craya. Theoretical research on the flow of non-homogeneous fluids. *La Houille Blanche*, 4:44–55, 1949.

A. W. Date. *Introduction to computational fluid dynamics*. Cambridge university press (2005).

Eramet. *Core drilling of FeMn furnaces*. Eramet Norway internal report (2010).

S. Ergun. Fluid flow through packed columns. *Chemical Engineering Progress*, 48: 89–94, 1952.

T. Fukutake and K. Okabe. Experimental studies of slag flow in the blast furnace hearth during tapping operation. *Transactions ISIJ*, 16:309–316, 1976.

GIA2010. *Silicon and Ferro Silicon: A Global Strategic Business Report*. Global Industry Analysts, Inc.

S. Grådahl. *Measurement campaign at Elkem Salten plant with focous on the tapping area*. SINTEF, Report No. 16525, Trondheim, Norway.

B. Y. Guo, D. Maldonado, P. Zulli, and A. B. YU. Cfd modelling of liquid metal flow and heat transfer in blast furnace hearth. *ISIJ International*, 48:1676–1685, 2008.

G. C. Hocking and L. K. Forbes. Supercritical withdrawal from a two-layer fluid through a line sink if the lower layer is of finite depth. *Journal of Fluid Mechanics*, 428:333–348, 2001.

D. G. Huber. Irrotational motion of two fluid strata towards a line sink. *Journal of Engineering Mechanics Division of American Society of Civil Engineering*, 86: 71–86, 1960.

H. P. Ingason. *Hollow electrodes in the production process for ferrosilicon*. Dr.-ing thesis, MI-Report 1994:27, NTH, Norway.

S. T. Johansen, S. Grådahl, R. Gammelsaeter, M. Raanes, A. E. Arntsberg, T. Lindstad, G. Enstad, and H. Tveit. Clogging of ferro-silicon furnace off-gas channels at high temperatures in smelter process gas handling and treatment. In *The Minerals, Metals and Materials Society*, pages 7–18, June 1991.

S. T. Johansen, H. Tveit, S. Grådahl, A. Valderhaug, and J. Byberg. Environmental aspects of ferro-silicon operations - an investigation of waste gas dynamics. In *Proceedings of the 8^{th} International Ferroalloys Congress, INFACON VIII*.

O. S. Klevan. *Removal of C and SiC from si and FeSi during ladle refining and solidification*. Dr.-ing thesis, MI-Report 1997:40, NTH, Norway.

F. Kuwahara and A. Nakayama. Numerical determination of thermal dispersion coefficients using a periodic porous structure. *Journal of Heat Transfer*, 121: 160–163, 1999.

H. L. Larsen. *AC electric arc models for laboratory set - up and a silicon metal furnace*. Dr.-ing thesis, MI-Report 1996:39, NTH, Norway.

B. F. Magnussen and B. H. Hjertager. On mathematical models of turbulent combustion with special emphasis on soot formation and combustion. *16^{th} international Symposium on Combustion*, 1976.

E. H. Myrhaug. *Non-fossil reduction materials in the silicon process-properties and behaviour*. Dr.-ing thesis, IMT-Report 2003:47, NTNU, Norway.

A. Nakayama and F. Kuwahara. A macroscopic turbulence model for flow in a porous medium. *Journal of Fluids Engineering*, 121:427–433, 1999.

K. Nishioka, T. Maeda, and M. Shimuzu. A three-dimensional mathematical modelling of drainage behavior in blast furnace hearth. *ISIJ International*, 45:669–676, 2005.

S. E. Olsen and M. Tangstad. Silicomanganese production - process understanding. In *Proceedings of the 10^{th} International Ferroalloys Congress, INFACON X*, pages 231–238, February 2004.

S. E. Olsen, M. Tangstad, and T. Lindstad. *Production of manganese ferroalloys*. Tapir Academic Press (2007).

Y. Otani, M. Saito, K. Usui, and N. Chino. The inner structure in submerged arc furnaces. In *6^{th} International Congress of Electroheat*, page 112, June 1968.

W. K. Rhim and K. Ohsaka. Thermophysical properties of molten silicon measured by high temperature electrostatic levitation. *Journal of Crystal Growth*, 208: 313–321, 2000.

E. Ringdalen and J. Eilertsen. Excavation of a 54 mva hc-ferrochromium furnace. In *Proceedings of the 9^{th} International Ferroalloys Congress, INFACON IX*, pages 166–173, June 2001.

J. Safarian-Dastjerdi. *Kinetics and mechanisms of reduction of MnO-containing silicate slags by selected forms of carbonaceous materials*. Doctoral thesis 2007:235, NTNU, Norway.

E. Scheepers. *Fingerprint of submerged - arc furnace, Optimising energy consumption through data mining, dynamic modelling and computational fluid dynamics*. Dr.-ing thesis, Printpartners Ipskamp, Enschede, The Netherlands.

A. Schei. On the chemistry of ferrosilicon production. *Tidsskrift Kjemi Bergvesen, Metallurgi 27*, 8-9:152–158, 1967.

A. Schei, J. Kr. Tuset, and H. Tveit. *Production of high silicon alloys*. Tapir Academic Press (1998).

M. Shin, L. T. Hoai, and J. Lee. Surface tension and density of fe-mn alloys. In *Presentation of TOFA 2010, Discussion Meeting on Thermodynamics of Alloys*.

R. Siegel and J. R. Howell. *Thermal radiation heat transfer*. Hemisphere Publishing Corporation (1992).

D. B. Spalding. Mixing and chemical reaction in steady confined turbulent flames. *13^{th} international Symposium on Combustion*, 1970.

T. E. Stokes, G. C. Hocking, and L. K. Forbes. Unsteady free-surface flow induced by a line sink. *Journal of Engineering Mathematics*, 47:137–160, 2003.

M. Tangstad. *Excavation of FeMn furnaces in 1994 and 1995*. Elkem internal report (1999), a.

M. Tangstad. *The high carbon ferromanganese process - coke bed relations*. Dr.-ing thesis, MI-Report 1996:49, NTH, Norway, b.

M. Tangstad. Presentation of roma-project (resource otimization in the material industry) a typical cooperation project in norway. In *Pyro 2011*, pages 209–217, March 2011.

M. Tangstad, B. Heiland, S. E. Olsen, and R. Tronstad. Simn production in a 150 kva pilot scale furnace. In *Proceedings of the 9^{th} International Ferroalloys Congress, INFACON IX*, pages 401–406, June 2001.

W. B. U. Tanzil, P. Zulli, J. M. Burgess, and W. V. Pinczewski. Experimental model study of the physical mechanisms governing blast furnace hearth drainage. *Transactions ISIJ*, 24:197–205, 1984.

G. Tranell, M. Andersson, E. Ringdalen, O. Ostrovski, and J. J. Steinmo. Reaction zones in a fesi75 furnace results from an industrial excavation. In *Proceedings of the 12^{th} International Ferroalloys Congress, INFACON XII*, pages 709–715, June 2010.

J. S. Turner. *Buoyancy effects in fluids*. Cambridge University Press (1973).

H. Tveit, T. Halland, K. I. Landrø, S. T. Johansen, and B. Ravary. The tapping process in silicon production. In *Proceedings of Silicon for the Chemical Industry VI*, pages 39–46, June 2002.

P. A. Tyvand. Unsteady free-surface flow due to a line source. *Journal of Physics of Fluids A*, 4:671–676, 1992.

A. M. Valderhaug. *Modeling and control of submerged - arc ferrosilicon furnaces*. Dr.-ing thesis, Report 92-81-W, NTH, Norway.

J. Westly. Dimensions of reduction furnaces for fesi and other alloys. *Journal of Furelectric*, 1:14–19, 1979.

D. C. Wilcox. *Turbulence Modeling for CFD*. DCW Industries, Inc., La Canada (1998), California, 1998.

Y. Yang, Y. Xiao, and M.A. Reuter. Analysis of transport phenomena in submerged arc furnace for ferrochrome production. In *Proceedings of the 10^{th} International Ferroalloys Congress, INFACON X*, pages 15–25, February 2004.

I. T. Zherdev, V. N. Davats, and I. I. Polyakov. Investigation of the structure of the working space in ferrosilicon furnaces. *Izv, Chern. Met*, 9:173–181, 1960.

I. T. Zherdev, I. I. Polyakov, D. P. Moskovtsev, and E. S. Yaskov. Methods and results from investigations of the operation of ferrosilicon furnaces. In *6^{th} International Congress of Electroheat*, page 113, June 1968.

C. Q. Zhou, D. Huang, Y. Zhao, and P. Chaubal. Computational fluid dynamics analysis of 3d hot metal flow characteristics in a blast furnace hearth. *Journal of Thermal Science and Engineering Applications*, 2:1–10, 2010.